NAVAL POSTGRADUATE SCHOOL

MONTEREY, CALIFORNIA

THESIS

EFFECTS OF LOCAL OSCILLATOR ERRORS ON DIGITAL BEAMFORMING

by

Marcos Chi Lim Siu

March 2016

Thesis Advisor: David C. Jenn
Second Reader: Ric Romero

Approved for public release; distribution is unlimited

THIS PAGE INTENTIONALLY LEFT BLANK

REPORT DOCUMENTATION PAGE			Form Approved OMB No. 0704-0188
Public reporting burden for this collection of information is estimated to average 1 hour per response, including the time for reviewing instruction, searching existing data sources, gathering and maintaining the data needed, and completing and reviewing the collection of information. Send comments regarding this burden estimate or any other aspect of this collection of information, including suggestions for reducing this burden, to Washington headquarters Services, Directorate for Information Operations and Reports, 1215 Jefferson Davis Highway, Suite 1204, Arlington, VA 22202-4302, and to the Office of Management and Budget, Paperwork Reduction Project (0704-0188) Washington, DC 20503.			
1. AGENCY USE ONLY *(Leave blank)*	**2. REPORT DATE** March 2016	**3. REPORT TYPE AND DATES COVERED** Master's thesis	
4. TITLE AND SUBTITLE EFFECTS OF LOCAL OSCILLATOR ERRORS ON DIGITAL BEAMFORMING			**5. FUNDING NUMBERS**
6. AUTHOR(S) Marcos Chi Lim Siu			
7. PERFORMING ORGANIZATION NAME(S) AND ADDRESS(ES) Naval Postgraduate School Monterey, CA 93943-5000			**8. PERFORMING ORGANIZATION REPORT NUMBER**
9. SPONSORING /MONITORING AGENCY NAME(S) AND ADDRESS(ES) N/A			**10. SPONSORING / MONITORING AGENCY REPORT NUMBER**
11. SUPPLEMENTARY NOTES The views expressed in this thesis are those of the author and do not reflect the official policy or position of the Department of Defense or the U.S. Government. IRB Protocol number ____N/A____.			
12a. DISTRIBUTION / AVAILABILITY STATEMENT Approved for public release; distribution is unlimited			**12b. DISTRIBUTION CODE**

13. ABSTRACT (maximum 200 words)

Digital phased array antennas are sensitive to phase error among elements because it affects the coherence necessary to create the array factor. There are many sources for phase errors: local oscillators and clocks, quadrature modulators and demodulators, non-linear components, and so forth. Additionally, phased arrays are sensitive to element mislocation, which introduces another source of phase error.

In this research, three types of phase errors were studied: phase noise, gain unbalance in quadrature modulators and demodulators, and element mislocation. Modifications to the traditional array pattern expression were proposed to account for these errors, and equations were programmed in MATLAB to perform parametric simulations to generate information regarding gain loss, beam pointing error, pattern distortions, and degradation in sidelobe levels. The objective is to aid array designers in setting acceptable tolerance limits for these types of errors.

14. SUBJECT TERMS radar, distributed array, phased array, phase synchronization, digital array, digital beamforming (dbf), wireless sensor network, transmit/ receive (t/r) module, local oscillator, phase noise			**15. NUMBER OF PAGES** 135
			16. PRICE CODE
17. SECURITY CLASSIFICATION OF REPORT Unclassified	**18. SECURITY CLASSIFICATION OF THIS PAGE** Unclassified	**19. SECURITY CLASSIFICATION OF ABSTRACT** Unclassified	**20. LIMITATION OF ABSTRACT** UU

NSN 7540-01-280-5500 Standard Form 298 (Rev. 2-89)
Prescribed by ANSI Std. 239-18

THIS PAGE INTENTIONALLY LEFT BLANK

Approved for public release; distribution is unlimited

EFFECTS OF LOCAL OSCILLATOR ERRORS ON DIGITAL BEAMFORMING

Marcos Chi Lim Siu
Lieutenant, Brazilian Navy
B.S.E.E., Universidade Federal Fluminense, 2004

Submitted in partial fulfillment of
the requirements for the degree of

MASTER OF SCIENCE IN ELECTRICAL ENGINEERING

from the

NAVAL POSTGRADUATE SCHOOL
March 2016

Approved by: David C. Jenn
Thesis Advisor

Ric Romero
Second Reader

R. Clark Robertson
Chair, Department of Electrical and Computer Engineering

THIS PAGE INTENTIONALLY LEFT BLANK

ABSTRACT

Digital phased array antennas are sensitive to phase error among elements because it affects the coherence necessary to create the array factor. There are many sources for phase errors: local oscillators and clocks, quadrature modulators and demodulators, non-linear components, and so forth. Additionally, phased arrays are sensitive to element mislocation, which introduces another source of phase error.

In this research, three types of phase errors were studied: phase noise, gain unbalance in quadrature modulators and demodulators, and element mislocation. Modifications to the traditional array pattern expression were proposed to account for these errors, and equations were programmed in MATLAB to perform parametric simulations to generate information regarding gain loss, beam pointing error, pattern distortions, and degradation in sidelobe levels. The objective is to aid array designers in setting acceptable tolerance limits for these types of errors.

THIS PAGE INTENTIONALLY LEFT BLANK

TABLE OF CONTENTS

I. INTRODUCTION....1
- **A. BACKGROUND....1**
- **B. DISTRIBUTED DIGITAL PHASED ARRAY....3**
- **C. PROBLEM DESCRIPTION....5**
- **D. RELATED WORK....6**
- **E. THESIS OUTLINE....7**

II. CRITICAL TECHNOLOGY AND TECHNIQUES....9
- **A. T/R MODULES....9**
  - **1. Transmitting Architectures....9**
  - **2. Receiver Architectures....11**
  - **3. Transmitter and Receiver Components....13**
    - ***a. Local Oscillators....13***
    - ***b. Mixers and Digital Multiplication....13***
    - ***c. Direct Digital Synthesizer....16***
- **B. SYNCHRONIZATION: LO DISTRIBUTION APPROACHES....16**
- **C. SUMMARY....19**

III. DIGITAL ARRAY THEORY....21
- **A. ARRAY EQUATIONS....21**
  - **1. Array Pattern....21**
  - **2. Element Factor....22**
  - **3. Array of Subarrays....24**
  - **4. Including Phase Errors in the Array Factor....25**
    - ***a. Random Phase Noise....26***
    - ***b. Scan Weight Errors....27***
    - ***c. Element Location Errors....30***
    - ***d. Final Expression for Array Factor....30***
  - **5. Directivity and Gain....31**
  - **6. Array Average Power Pattern and Sidelobe Level....32**
- **B. SUMMARY....32**

IV. TIMING AND SYNCHRONIZATION....33
- **A. TIME AND PHASE SYNCHRONIZATION....34**
  - **1. Frequency, Phase and Time Models....34**
  - **2. Accuracy and Drift....36**
  - **3. Phase Noise....36**

a. Power-Law Model *37*
b. Leeson's Equation *40*
B. TIME AND PHASE SYNCHRONIZATION TECHNIQUES **42**
1. Phase and Frequency Synchronization Using Phased Locked Loop **42**
a. Phased Locked Loop *42*
b. Costas Loop *44*
c. Synchronization Using PLLs *45*
2. Phase and Frequency Synchronization Stable Local Oscillator **45**
C. SUMMARY **46**

V. SIMULATIONS AND RESULTS **47**
A. INTRODUCTION **47**
B. ARRAY FACTOR COMPLEX WEIGHTS **48**
C. PATTERN CHARACTERISTICS **48**
D. UNIFORM ARRAY HARDWARE ERROR SIMULATIONS **50**
1. Simulation Scenario for Phase Noise, Gain Unbalance and Frequency Drift Error **50**
2. Phase Noise Simulation **51**
a. Simulation Scenario *51*
b. Simulation Results *51*
3. *I* and *Q* Gain Unbalance **56**
a. Simulation Scenario *56*
b. Simulation Results *58*
4. Linear Frequency Drift **62**
a. Simulation Scenario *62*
b. Simulation Results *64*
5. Element Mislocation Error **67**
a. Simulation Scenario *67*
b. Simulation Results *69*
E. ARRAY OF SUBARRAYS HARDWARE ERROR SIMULATIONS **73**
1. Simulation Scenario for Phase Noise, Gain Unbalance and Frequency Drift Error **73**
2. Phase Noise Simulation Results **74**
3. *I* and *Q* Gain Unbalance Simulation Results **78**
F. TYPICAL SCENARIO **83**
1. Calculating Phase Noise **84**
2. Crystal Oscillator Wenzel 501-26636 ..... **86**

3. Voltage Controlled Oscillator Hittite HMC834LP6GE 87
4. Phase Errors Due to *I* and *Q* Gain Unbalance 89
5. Overall Pattern Degradation 90
G. SUMMARY 91

VI. CONCLUSION AND FUTURE WORK 93
A. CONCLUSION 94
B. FUTURE WORK 95
1. Phase Noise Analysis for EHF Systems.....95
2. LO Distribution Techniques 96

APPENDIX. LOCAL OSCILLATORS.....97

LIST OF REFERENCES 105

INITIAL DISTRIBUTION LIST 111

THIS PAGE INTENTIONALLY LEFT BLANK

LIST OF FIGURES

Figure 1. DDG-74 (USS McFaul) with AN/SPY-1 Radar Highlighted.....2

Figure 2. A Phased Array Antenna 3

Figure 3. Phased Array Architectures 4

Figure 4. Homodyne Transmitter Architecture 9

Figure 5. Heterodyne Transmitter Architecture 10

Figure 6. Direct Downconversion Receiver Architecture 11

Figure 7. Heterodyne Receiver Architecture.....12

Figure 8. Low IF Receiver Architecture 12

Figure 9. Spurious-Response for a 30 GHz Mixer. LO Frequency is 26 GHz. The IF Band is from 3 to 4 GHz. 15

Figure 10. General DDS Architecture.....16

Figure 11. Residual Phase Error After Synchronization with 4-bit Phase Steps 18

Figure 12. Subarray *m* and its Local Coordinate System Relative to the Global Origin O. 25

Figure 13. Random Time Deviation PSD Obeying the Power-Law Model Plotted on a Log-Log Diagram 39

Figure 14. Phase Noise of the Voltage Controlled Oscillator Model ROS-2600-1119, Manufacture Minicircuits.....40

Figure 15. Block Diagram of PLL.....43

Figure 16. Block Diagram of Demodulator using Costas Loop 44

Figure 17. A T/R Module Block Diagram. Phase Error Sources are Highlighted in Red. 47

Figure 18. Linear Array Pattern Degraded by Phase Noise (solid). (a) $\varphi_{RMS} = 0.05$ rad and (b) $\varphi_{RMS} = 0.5$ rad 52

Figure 19. Relative Average Sidelobe Level $\langle SLL \rangle$ vs. Phase Noise Standard Deviation φ_{RMS} Plotted for Four Scanning Angles 53

Figure 20. Relative Peak Sidelobe Level $MAX(SLL)$ vs. Phase Noise Standard Deviation φ_{RMS} Plotted for Four Scanning Angles 53

Figure 21. Array Gain Loss Due to Phase Noise Plotted for Four Different Scanning Angles 54

Figure 22. Average Beam Pointing Error $\langle BPE \rangle$ vs. Phase Noise Deviation φ_{RMS} Plotted for Four Different Scanning Angles.....55

Figure 23. Relative Standard Deviation σ_{BPE} vs. Phase Noise Deviation φ_{RMS} Plotted for Four Different Scanning Angles.....55

Figure 24. Half-Power Beamwidth vs. Phase Noise Deviation φ_{RMS} Plotted for Four Different Scanning Angles 56

Figure 25. Receiving Simulation Scenario where L_I and L_Q are Hypothetical Random Attenuators 57

Figure 26. Linear Array Pattern Degraded by *I* and *Q* Gain Unbalance (Solid). (a) L = 0.4 dB and (b) L = 1.0 dB 58

Figure 27. Relative Average Sidelobe Level $\langle SLL \rangle$ vs. *I* and *Q* Gain Unbalance *L* Plotted for Four Scanning Angles.....59

Figure 28. Relative Peak Sidelobe Level vs. *I* and *Q* Gain Unbalance *L* Plotted for Four Scanning Angles 59

Figure 29. Array Gain Loss Due to *I* and *Q* Gain Unbalance *L* Plotted for Four Scanning Angles 60

Figure 30. Relative Average Beam Pointing Error $\langle BPE \rangle$ vs. *I* and *Q* Gain Unbalance *L* Plotted for Four Scanning Angles 61

Figure 31. Relative Standard Deviation σ_{BPE} vs. *I* and *Q* Gain Unbalance *L* Plotted for Four Scanning Angles.....61

Figure 32. Half-Power Beamwidth vs. *I* and *Q* Gain Unbalance *L* Plotted for Four Scanning Angles.....62

Figure 33. Gain Loss Due to LO in Free-Run as a Function of Time. Different Colors Represent Different LO Accuracies, Operating at 300 MHz. 65

Figure 34. Average Sidelobe Level Due to LO in Free-Run as a Function of Time. Different Colors Represent Different LO Accuracies, Operating at 300 MHz. 65

Figure 35. Pattern Degradation Due to LO in Free-Run. LO Accuracies of 0.1 ppm or Better (a) t = 1.8 μs (b) t = 1.9 ms and (c) t = 920 ms 66

Figure 36. Pattern Degradation Due to LO in Free-Run. LO Accuracies of 100 ppm or Better (a) t = 1.8 μs (b) t = 1.9 ms and (c) t = 920 ms 66

Figure 37. (a) Ideal Linear Array. (b) Linear Array with Elements non-Uniformly Distributed.....67

Figure 38. Linear Array Aattern Degraded by Element Mislocation (a) RMS Mislocation Error 0.006 Wavelength and (b) RMS Mislocation Error 0.058 Wavelength 69

Figure 39. Relative Average Sidelobe $\langle SLL \rangle$ vs. RMS Element Mislocation (P_ϵ) Expressed in Fraction of Wavelength Plotted for Four Different Scanning Angles 70

Figure 40. Relative Peak Sidelobe vs. RMS Element Mislocation (P_ϵ) Expressed in Fraction of Wavelength Plotted for Four Different Scanning Angles 70

Figure 41. Array Gain Loss Due and RMS Element Mislocation (P_ϵ) Plotted for Four Scanning Angles 71

Figure 42. Magnitude of Average Beam Pointing Error $\langle BPE \rangle$ vs. RMS Element Mislocation (P_ϵ) Plotted for Four Different Scanning Angles 72

Figure 43. Relative Standard Deviation Beam Pointing Error σ_{BPE} vs. RMS Element Mislocation (P_ϵ) Plotted for Four Different Scanning Angles 72

Figure 44. Half-Power Beamwidth vs. RMS Element Mislocation (P_ϵ) Plotted for Four Different Scanning Angles 73

Figure 45. Linear Array of Subarrays Pattern Degraded by Phase Noise (blue), the Dotted Line is the Array Without Phase Noise Error (a) $\varphi_{RMS} = 0.05$ rad and (b) $\varphi_{RMS} = 0.5$ rad 75

Figure 46. Relative Average Sidelobe $\langle SLL \rangle$ vs. RMS Phase Deviation φ_{RMS} Plotted for Four Different Scanning Angles 75

Figure 47. Relative Peak Sidelobe Level vs. RMS Phase Deviation φ_{RMS} Plotted for Four Different Scanning Angles 76

Figure 48. Array Gain vs. RMS Phase Deviation φ_{RMS} Plotted for Four Scanning Angles 76

Figure 49. Average Beam Pointing Error $\langle BPE \rangle$ vs. RMS Phase Deviation φ_{RMS} Plotted for Four Different Scanning Angles 77

Figure 50. Relative Standard Deviation Beam Pointing Error σ_{BPE} vs. RMS Phase Deviation φ_{RMS} Plotted for Four Different Scanning Angles 77

Figure 51. Half-Power Beamwidth vs. RMS Phase Deviation φ_{RMS} Plotted for Four Different Scanning Angles 78

Figure 52. Linear Array of Subarrays Pattern Degraded Because of Unbalanced Gain (blue), and the Dotted Line is the Array without Errors (a) L= 1.0 dB and (b) L = 5.0 dB 79

Figure 53. Relative Average Sidelobe $\langle SLL \rangle$Increase Due to I and Q Gain Unbalance Plotted for Four Different Scanning Angles 80

Figure 54. Relative Peak Sidelobe Level Increase Due to I and Q Gain Unbalance Plotted for Four Different Scanning Angles 80

Figure 55. Array Gain Loss Due due to I and Q Gain Unbalance Plotted for Four Scanning Angles....81

Figure 56. Average Beam Pointing Error $\langle BPE \rangle$ vs. I and Q Gain Unbalance Plotted for Four Different Scanning Angles 81

Figure 57. Relative Standard Deviation Beam Pointing Error σ_{BPE} vs. I and Q Gain Unbalance Plotted for Four Different Scanning Angles 82

Figure 58. Half-Power Beamwidth vs. I And Q Gain Unbalance Plotted for Four Different Scanning Angles 82

Figure 59. T/R Module Block Diagram Used as Example of Digital Phased Array with Non-Ideal Components....83

Figure 60. Phase Noise Frequency-Domain Representation of A MCXO Model Vectron MX-503. The Colored Area under the Curve Represents the Phase Noise Power....85

Figure 61. The Four Possible Modes of Oscillation for Quartz Crystals 97

Figure 62. CsFS Operation. Left the Atomic State Selection. Right Beam Detection 99

Figure 63. Rbfs Operation Block Diagram 100

Figure 64. CSAC Using Coherent Population Trapping Technique 101

LIST OF TABLES

Table 1. Array Characteristics used in MATLAB Simulations.....51

Table 2. Array Characteristics used in MATLAB Simulations.....67

Table 3. Array of Subarrays Characteristics used in MATLAB Simulations.....74

Table 4. Subarray Characteristics used in MATLAB Simulations.....74

Table 5. Example T/R Module Components and Function 84

Table 6. XO Wenzel 501-26636 Phase Noise Specification 87

Table 7. VCO Hittite HMC834LP6GE Phase Noise Specification at 4 GHz.....87

Table 8. VCO Hittite HMC834LP6GE Phase Noise Specification at 100 MHz.....88

Table 9. Pattern Degradation Due to LO Phase Noise.....89

Table 10. Modulator, Demodulator Gain Unbalance at 3500 MHz, and DDS and A/D Converter Gain Error.....89

Table 11. Pattern Degradation Due to Transmission *I* and *Q* Gain Unbalance 90

Table 12. Pattern Degradation Due to Transmission *I* and *Q* Gain Unbalance 90

Table 13. Overall Pattern Degradation 91

Table 14. Oscillator Performance Comparison.....103

THIS PAGE INTENTIONALLY LEFT BLANK

LIST OF ACRONYMS AND ABBREVIATIONS

A/D	analog-to-digital converters
ACT	arrays at commercial timescales
AF	array factor
AM	amplitude modulation
BPF	band pass filter
COTS	commercial-off-the-shelf
CPT	coherent population trapping
CSAC	chip scale atomic clock
CsFS	cesium beam frequency standard
CW	continuous wave
D/A	digital-to-analog converters
DARPA	Defense Advanced Research Project Agency
DBF	digital beamformer
DDAR	distributed digital array radar
DDS	Direct Digital Synthesizer
DDSA	distributed digital subarray
DOD	Department of Defense
DSP	digital signal processor
EF	element factor
EW	electronic warfare
FFM	flicker frequency modulation
FOV	field-of-view
FPGA	field-programmable gate array
FPM	flicker phase modulation
H-maser	Hydrogen maser standard
HPBW	half-power beamwidth
I	in-phase
IF	intermediate frequency
IM	intermodulation
LC	inductor-capacitor

LNA	low noise amplifier
LO	local oscillator
LPF	low pass filter
MCXO	microcomputer compensated crystal oscillator
NPS	Naval Postgraduate School
NTP	network time protocol
OCXO	oven controlled crystal oscillator
PA	power amplifier
PD	phase detector
PLL	phased locked loop
PPM	parts-per-million
PPS	pulse-per-second
PSD	power spectral density
PTP	precision time protocol
PXO	packaged crystal oscillator
Q	quadrature
Q	quality factor
Rb	rubidium
RbFS	rubidium frequency standard
RC	resistor-capacitor
RF	radio frequency
RWFM	random walk frequency modulation
SiO2	silicon dioxide
SNR	signal-to-noise ratio
STALO	independent stable local oscillator
STAP	space-time-adaptive processing
T/R	transmit-receive
TCXO	temperature compensated crystal oscillator
UHF	ultra high frequency
UTC	coordinated universal time
VCO	voltage controlled oscillator
VCSELs	vertical-cavity surface emitting lasers

VCXO	voltage controlled crystal oscillator
VHF	very high frequency
WFM	white frequency modulation
WLAN	wireless local area network
WPM	white phase modulation
WSN	wireless sensor network
XO	crystal oscillator

THIS PAGE INTENTIONALLY LEFT BLANK

ACKNOWLEDGMENTS

I would like to express my sincere gratitude to my advisor Professor David Jenn for his guidance, continuous support, and patience on the development of this thesis. I would like to thank Professor Ric Romero for his valuable time and willingness as a second reader of this thesis.

I would like to express my gratitude and love for my amazing wife, Liane, whose support, patience, and love made me finish this journey successfully. To my parents, Lina and Ming; friends Pornrerk Rerkngamsanga, Michail Pothitos and Jesus Zegarra; brothers Marcelo and Marx; and all those that in one way or another made this journey an amazing experience, I would like to express my appreciation for their constant encouragement, which drove me where I am today.

THIS PAGE INTENTIONALLY LEFT BLANK

I. INTRODUCTION

A. BACKGROUND

Friis and Feldman [1] proposed the idea of an electronic beamformer in 1937, when they published "Multiple unit steerable antenna for short wave reception," which, according to [2], "supported a very sophisticated test of angle and time diversity combining." Although their studies led to the development of modern technologies like multiple beam arrays, digital beamforming, and space-time-adaptive processing (STAP), they were limited to existing technology in the 1930s and 1940s and had to use mechanically rotated phase shifters to develop multiple unit steerable antenna. In the 1950s, the ferrite phase shifter was introduced, which led to improvements that allowed better beam steering control [2].

In the following decades, radar systems took advantage of electronically steered phased arrays. Aperture antennas (e.g., reflectors) are efficient and simple to construct but are limited by mechanical beam control. For electronic warfare (EW) applications, arrays play a major role in direction finding and tracking systems. One important example of a phased array antenna application is the U.S. Navy AN/SPY-1, shown in Figure 1. The electronically controlled beam steering is faster, more precise and versatile, and allows the radar to search for and track multiple targets simultaneously.

Phased array antennas are not exclusively employed in military applications. For example, distributed antenna arrays have been used for decades in long baseline interferometry in astronomy [3]. In meteorology applications, weather radars take advantage of electronic beamforming to improve weather radar performance, such as in the MWR-05XP mobile phased array weather radar [4]. Recently, automotive collision avoidance radars using phased arrays have been installed in automobiles for "automatic cruise control, parking aid, blind spot detection, and side collision warning capabilities" [5].

Figure 1. DDG-74 (USS McFaul) with AN/SPY-1 Radar Highlighted

Source [6]: "Ballistic Missile Defense: The Aegis SPY-1 Radar," Mostly Missile Defense, 2012. [Online]. Available: http://mostlymissiledefense.com/2012/08/03/ballistic-missile-defense-the-aegis-spy-1-radar-august-3-2012/. [Accessed: 23-Nov-2015].

More recently, the Defense Advanced Research Project Agency (DARPA) sponsored a program to develop new phased array hardware technology which will form the basis for new DOD projects employing arrays. The Arrays at Commercial Timescales (ACT) will research and expand existing technologies to develop:

1. A common building block for RF arrays,
2. A reconfigurable electromagnetic interface (the antenna interface from the electronics to the RF signal), and
3. Over-the-air coherent array aggregation [7].

If successful, the DARPA ACT program will provide a starting point for all array development programs. The main factor leading to expensive array projects is the engineering costs for developing a new product, which are usually specific for an application and platform [7]. ACT acknowledges that a "technical solution is needed to bring military array programs to more manageable cost levels and timescales," [7] and this program will facilitate the access of this technology by industry to manufacture civilian systems.

B. DISTRIBUTED DIGITAL PHASED ARRAY

To achieve a narrow pencil beamwidth and high gain and, consequently, long-range detection, systems like the AN/SPY-1 are physically large and structurally difficult to handle. The system, once implemented, is not flexible (i.e., it is not suitable for significant changes).

To perform beam steering and side lobe suppression, the array beamformer needs to accurately control the element excitation phase and magnitude (i.e., the element weights). Note that the following discussion is with regard to a transmitting array, but the same concepts apply to receiving arrays.

Traditionally, analog beamforming requires a large and complex network of transmission lines, phase shifters, and attenuators to control the radiated waveform at each individual element. A photograph of an S-band ground-based radar phased array is shown in Figure 2, which clearly illustrates the weight and size disadvantages of an analog beamforming network.

Figure 2. A Phased Array Antenna

Source [8]: "Phased Array Antenna," Hughes Aircraft Co., Culver City, CA (unpublished photo).

Digital arrays use a digital beamformer (DBF) controller, which is a computer, instead of the analog beamforming network. The analog portion of the array resides in the transmit-receive (T/R) module, which is located at the element level. The differences among these architectures are illustrated in Figure 3(a) and 3(b).

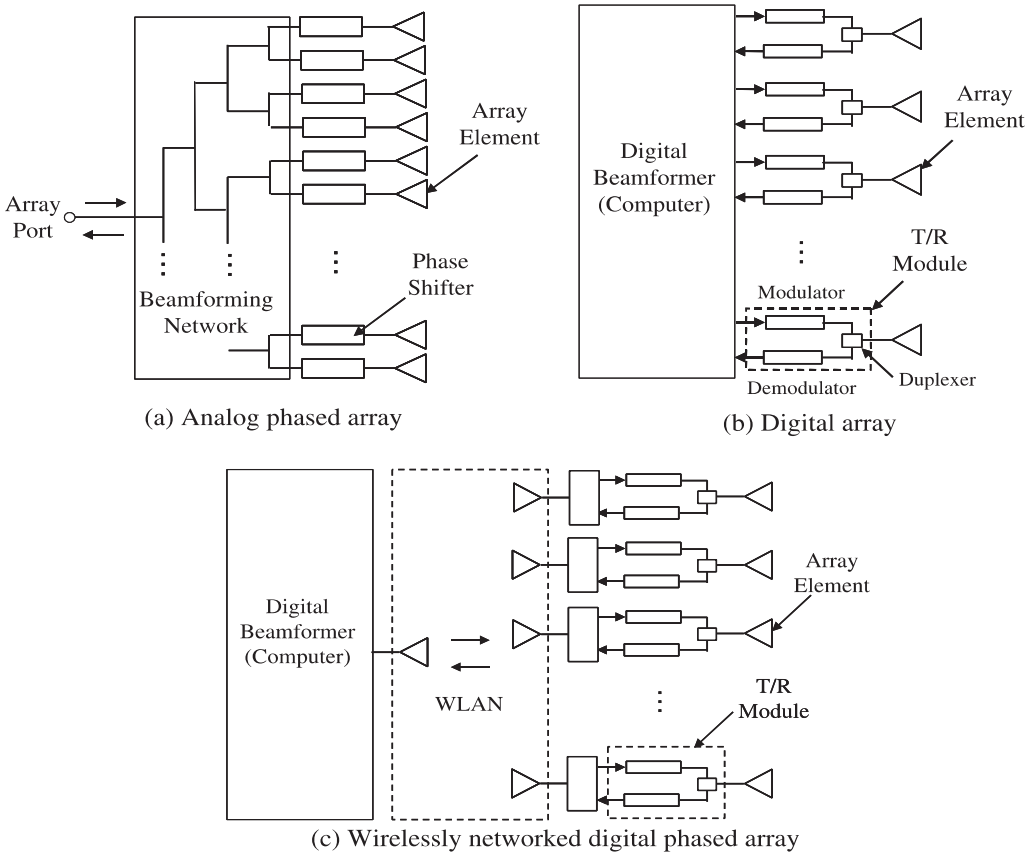

Figure 3. Phased Array Architectures

Source [3]: D. Jenn, Y. Loke, T. C. H. Matthew, Y. E. Choon, O. C. Siang, and Y. S. Yam, "Distributed Phased Arrays and Wireless Beamforming Networks," *Int. J. Distrib. Sens. Networks*, vol. 5, no. 4, 2009. p. 284.

In a distributed architecture, digital arrays can have their elements spread along large surfaces like the entire ship hull or a hillside [3], overcoming some of the problems that arise with large arrays.

In similar fashion, the wireless distributed phased array proposed in [3] has the beamformer network replaced by wireless network. “This architecture brings a set of advantages including flexibility, scalability, adaptability to the operational environment, and survivability” [3].

The DBF connects to T/R modules through a wireless local area network (WLAN) using commercial off-the-shelf (COTS) equipment. The wirelessly controlled phased array is illustrated in Figure 3 (c). The wirelessly networked, digital distributed phased array is aligned with the concepts in the third technological area of ACT, i.e., the development an over-the-air coherent array aggregation.

The great advantage for ship-based digital distributed arrays is the possibility of connecting subarrays that are spatially separated through a wireless or wired network; therefore, the possibility of synthesizing large arrays on a single platform exists using this distributed digital subarray (DDSA) concept [9].

C. PROBLEM DESCRIPTION

Phased arrays are designed to have high gain, accurate beam pointing and low sidelobes; however, due to the use of non-ideal components, magnitude and phase errors occur, altering the pattern characteristics if these errors are large enough.

There are many sources of phase errors, and all components of the system contribute, direct and indirectly, to increase these errors. Timing and phase errors related to local oscillators (LOs) are the main source of phase noise and frequency drift, and LOs are used as a reference for clocking in digital systems; hence, phase noise and frequency drift affect all digital components, such as direct digital synthesizers (DDSs), analog-to-digital (A/D) converters and digital-to-analog (D/A) converters.

There are other sources of phase errors that are not directly related to LOs. Quadrature mixers, which usually are integrated into modulator and demodulator boards, can distort phase information if an exact 90^{o} phase shift between in-phase (I) and quadrature (Q) LO is not supplied. For example, homodyne modulators use independent

DDS channels to generate *I* and *Q*; consequently, a difference in D/A gain can impact the phase balance. The same occurs in homodyne receivers [10].

Moreover, phased array antennas rely on the coherent processing of transmitted and received signals among their elements for beamforming; therefore, phase errors are introduced if the element position is not correctly processed.

The objective of this thesis research is to find acceptable limits on amplitude and phase errors in the up and downconversion processes by examining their effects on gain loss, beam pointing, pattern distortions, and degradation in sidelobe levels based on parametric simulations.

In most instances it is assumed that all errors are uncorrelated. It is important to mention that there are several types of highly correlated errors which can increase sidelobe peaks significantly. The frequency-dependent phase errors due to transmission lines, quantization errors, and imprecise tapering may generate frequency and spatially correlated errors [11].

D. RELATED WORK

For the past several years, many students have contributed to distributed digital phased array research at Naval Postgraduate School (NPS). One of the most critical challenges to overcome is the problem of time and frequency synchronization. Loke [12] and Tsai [13] investigated wireless local oscillator distribution and element synchronization using a "brute force" algorithm. In [13] Tsai achieved phase synchronization with a 20-degree tolerance range.

Additionally, Loke [12] also investigated the impact of deforming surfaces, i.e., ship hull deflection, in studying element mislocation effects on synchronization. For large wavelengths such as the VHF/UHF frequency bands, it was found that no correction was needed; however, at higher frequencies phase errors due to position errors can be significant.

In 2008, Djerf and Tornazakis [14] designed and tested T/R modules for a distributed digital array radar (DDAR) and also developed a control and processing

program in LabVIEW to control elements using a field programmable gate array (FPGA). They also addressed phase synchronization problems by investigating different T/R module components, such as circulators, power dividers and low noise amplifiers (LNAs). In their experiments synchronization was achieved with 10 degrees of deviation.

In addition to phase error introduced by the synchronization algorithm, addressed in [12], [13] and [14], other aspects of phase synchronization such as jitter, frequency drift and frequency offset contribute to distort beam pattern and sidelobe levels. These phenomena are described in [15], where a mathematical model for instantaneous phase is described.

Array error effects due to random magnitude and phase errors were analyzed in [11] by Mailloux. Analytical expressions were derived to evaluate the impact on residual sidelobe errors, peak sidelobe expectation, gain degradation and beam pointing error.

E. THESIS OUTLINE

This thesis is arranged into six chapters. In Chapter I, general background about phased array antennas is presented. The thesis objective and problem description were also provided, along with a summary of previous work.

In Chapter II, the T/R module architectures and the issue of phase errors in the frequency multiplication stage caused by LOs errors are presented. Additionally, in this chapter is summarized the research on LO distribution and synchronization techniques published in [12], [13], [14] and [16].

In Chapter III, digital array theory is reviewed. The expressions for array pattern, array factor and gain are presented, along with a modified array factor model that includes phase errors.

In Chapter IV, a mathematical model for non-ideal LO instantaneous time and phase, which includes the impact of phase noise and frequency deviations is presented. The phase noise phenomenon is addressed in this chapter by discussing the Power-Law and the Leeson's models.

In Chapter V, the simulation results are presented, and the effects of phase errors on pattern distortions, degradation in sidelobe levels, gain loss and beam pointing are illustrated. Additionally, a typical scenario is analyzed to exemplify the effects of amplitude and phase errors in the up and downconversion processes using the simulation results presented in this chapter.

In Chapter VI, the research is summarized and conclusions are presented, along with suggestions for possible future research.

II. CRITICAL TECHNOLOGY AND TECHNIQUES

A. T/R MODULES

1. Transmitting Architectures

Transmitters can be divided into homodyne and heterodyne types. Homodyne transmitters have only one upconversion stage and for this reason are also called direct upconversion transmitters. Heterodyne transmitters generally have two upconversion stages, which take baseband signals to an intermediate frequency (IF) and then use another mixer to convert IF to the carrier frequency at a radio frequency (RF). The architectures are illustrated in Figure 4 and Figure 5, respectively. The digital portion of the receiver is highlighted with a dotted box. The array beam control is performed with a digital signal processor (DSP). A power amplifier (PA) is used to provide the necessary gain for transmission, whereas, a band pass filter (BPF) is employed to suppress spurious signals.

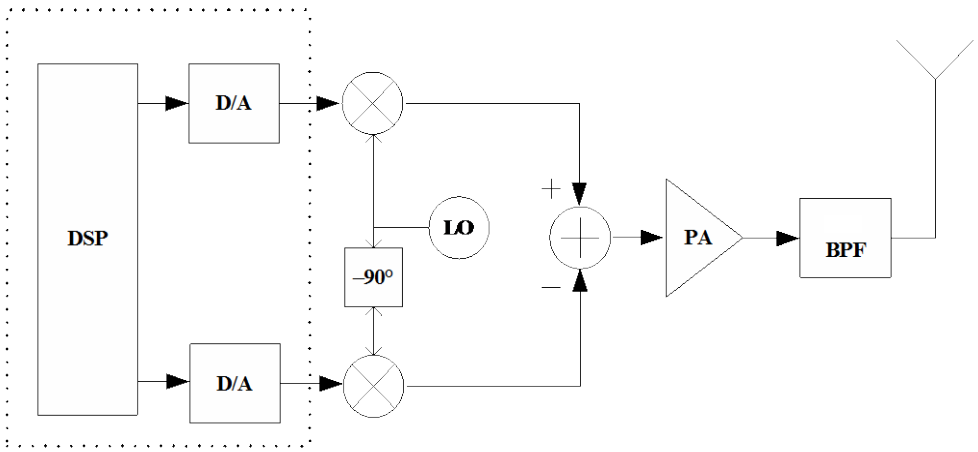

Figure 4. Homodyne Transmitter Architecture

Adapted from [10]: L. B. Oliveira, J. R. Fernandes, I. M. Filanovsky, C. J. M. Verhoeven, and M. M. Silva, *Analysis and Design of Quadrature Oscillators*, vol. 1. Springer Science+Business Media B.V., 2008. p. 16.

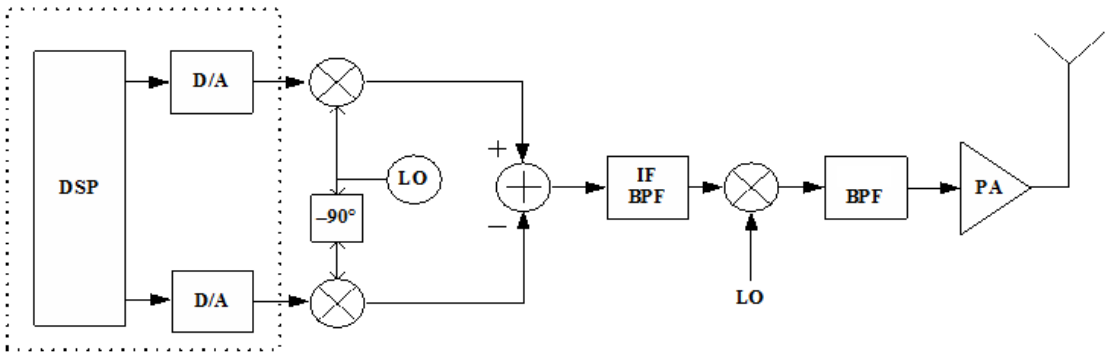

Figure 5. Heterodyne Transmitter Architecture

Adapted from [10]: L. B. Oliveira, J. R. Fernandes, I. M. Filanovsky, C. J. M. Verhoeven, and M. M. Silva, *Analysis and Design of Quadrature Oscillators*, vol. 1. Springer Science+Business Media B.V., 2008. p. 16.

Complex analog baseband signals, i.e., *I* and *Q*, are generated in homodyne transmitters by a DDS in two different branches. In the modulator, *I* and *Q* signals are mixed with the LO independently and then combined in the RF front end. This architecture requires two D/A converters and a high power BPF.

The main constraint with this architecture is the local oscillator "injection pulling" and "injection locking" effects due to poor isolation between the mixer and power amplifier. Both effects cause a frequency disturbance in the transmitted signal [10].

The heterodyne transmitters combine *I* and *Q* signals at an intermediate frequency and then upconvert them to RF using a single mixer. By using two stages of upconversion, heterodyne transmitters have to deal with image frequency rejection and also demand high attenuation band pass filters (around 60 dB) to reduce unwanted spurious frequencies [10].

2. Receiver Architectures

Receiver architectures are divided into three groups: homodyne, heterodyne and low IF.

Homodyne and heterodyne receivers have one and two downconversion stages, respectively. Homodyne receivers downconvert RF signals using two mixers to generate baseband *I* and *Q*, which are sampled and digitalized, as shown in Figure 6. Heterodyne receivers first downconvert from RF to IF and then use another stage to obtain baseband *I* and *Q*, as shown in Figure 7. A LNA is used to improve the received signal power.

Homodyne receivers are sensitive to flicker noise, channel selection, LO leakage, quadrature errors (*I* and *Q* amplitude and phase errors), DC offsets, and intermodulation (IM) effects [10], and consequently might not be the best architecture for T/R modules.

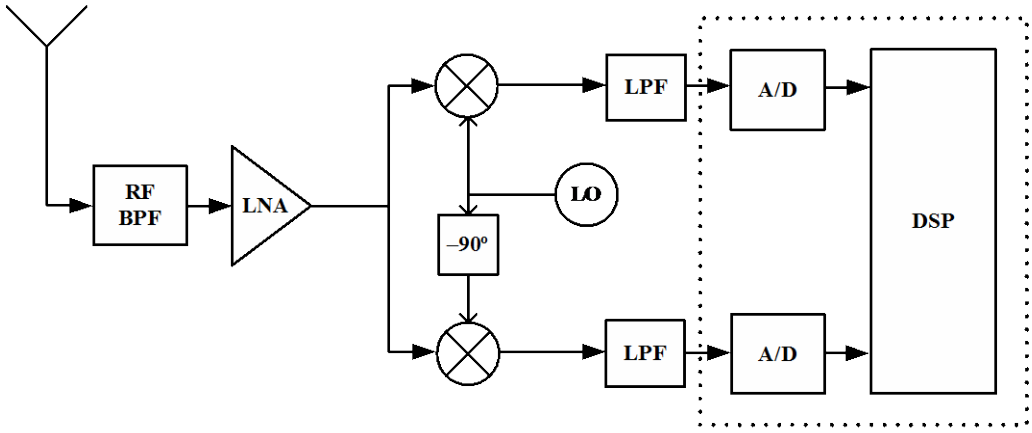

Figure 6. Direct Downconversion Receiver Architecture

Source [10]: L. B. Oliveira, J. R. Fernandes, I. M. Filanovsky, C. J. M. Verhoeven, and M. M. Silva, *Analysis and Design of Quadrature Oscillators*, vol. 1. Springer Science+Business Media B.V., 2008. p. 10.

The drawback for heterodyne receivers is the necessity of two downconversion stages, which complicates chipset integration and requires an RF filtering stage to suppress the possible image frequency before mixing [10]; furthermore, the additional downconversion stage increases phase noise and spurious responses.

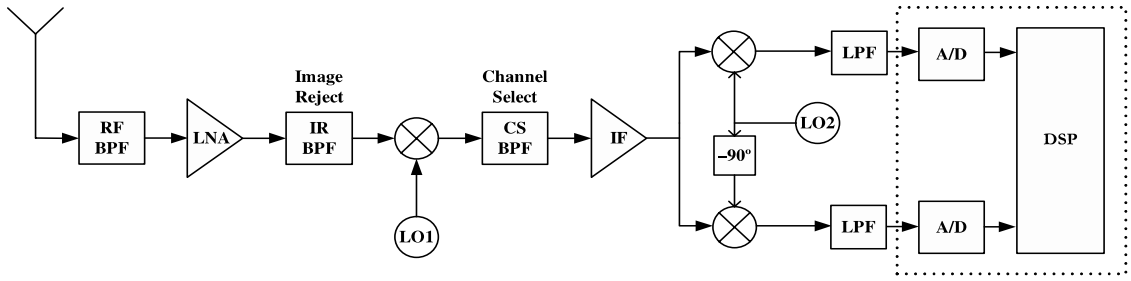

Figure 7. Heterodyne Receiver Architecture

Source [10]: L. B. Oliveira, J. R. Fernandes, I. M. Filanovsky, C. J. M. Verhoeven, and M. M. Silva, *Analysis and Design of Quadrature Oscillators*, vol. 1. Springer Science+Business Media B.V., 2008. p. 9.

Combining previous techniques, we obtain a third approach with the benefits of both heterodyne and homodyne receivers. A low IF receiver is a heterodyne receiver that suppresses the image frequency in the mixing stage. An example is the Hartley architecture, illustrated in Figure 8, in which the RF signal is first downconverted to complex IF (i.e., *I* and *Q*). The image frequency is suppressed by adding *I* shifted by 90^{o} with *Q*. The output of a Hartley mixer is a clean IF output, which is treated like regular IF in heterodyne receivers. This architecture requires a very accurate quadrature signal; therefore, in the case of *I* and *Q* unbalance, the image frequency rejection is incomplete.

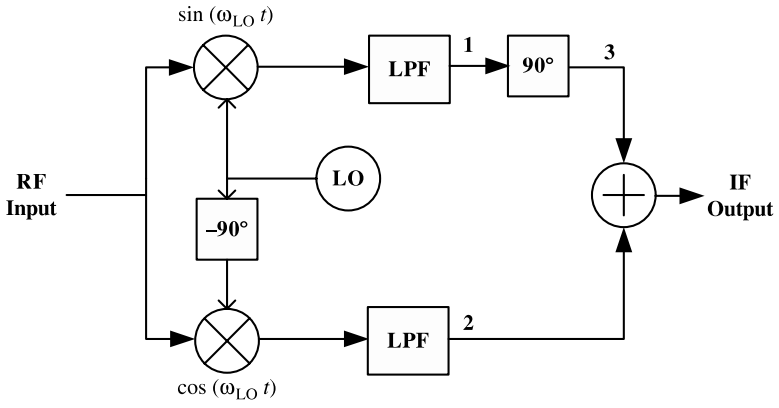

Figure 8. Low IF Receiver Architecture

Source [10]: L. B. Oliveira, J. R. Fernandes, I. M. Filanovsky, C. J. M. Verhoeven, and M. M. Silva, *Analysis and Design of Quadrature Oscillators*, vol. 1. Springer Science+Business Media B.V., 2008. p. 12.

3. Transmitter and Receiver Components

a. Local Oscillators

Oscillators are used to supply an accurate reference signal to quadrature mixers for converting the RF signals to baseband or IF signals, and vice versa. Their main characteristics are a high Q factor, low phase noise, and tunability [10]. Beamforming literature usually deals with an ideal LO; however, an inaccurate LO reference causes distortion in the beamforming process that affects sidelobes, gain and beam pointing angle.

Oscillators are divided in two groups [10]:

1. Strongly non-linear or relaxation oscillators are usually designed as resistor-capacitor (RC) active circuits, a feature that allows them to be integrated into a chipset. They are often used in applications that are resilient to phase noise.

2. Quasi-linear oscillators are those, which have a resonator element, such as dielectric resonators, crystals, striplines, and inductor-capacitor (LC) tanks. Resonators give the circuit better performance when compared to relaxation oscillators.

One common example of quasi-linear oscillator is the voltage controlled crystal oscillators (VCXO) using a quartz resonator. A quartz resonator is a capacitor using a piece of quartz crystal as dielectric. Since quartz is a piezoelectric crystal, when excited it converts electric potential into mechanical oscillation [17]. The advantages of a VCXO are high Q and low phase noise, which is desired for distributed arrays; however, the frequency selection range is very limited.

b. Mixers and Digital Multiplication

Mixers are non-linear circuits used to achieve a multiplication of two signals. In receivers, mixers downconvert RF signals by combining them with a local oscillator reference. Most of the applications use balanced mixers, which have inherent isolation of RF, IF and LO ports and the ability to reject spurious frequencies. On the other hand, balanced mixers require a large number of components, i.e., diodes, and require high LO power, limiting their use to applications without LO power constraints.

Furthermore, there are other interactions between a LO and mixer that must be mentioned. The LO amplitude modulated noise is added to LO signals when it is amplified and frequency multiplied. Additionally, temperature variations and vibration cause noise insertion. These random errors are represented by LO phase noise, which is proportional to the inverse square of resonator Q factor [18]; therefore, phase noise is reduced using high Q oscillators.

Another concern is LO spurious frequencies (or spurs) generated in mixing. Spurs are the result of non-linear combining in the mixing process. Unlike noise spurs, they are usually phase modulated and difficult to filter when they lie in the RF or IF bands.

Intermodulation (IM) products are the consequence of the interaction between two tones in a non-linear device. In the mixer, the two-tone interaction (i.e., LO and RF signals) is desired to up or downconvert; however, mixing also generates other unwanted product frequencies. For example the output in the mixing process gives the following frequencies [18]:

$$f_{o_{IF}} = mf_o + nf_{LO} \tag{2.1}$$

where

$f_{o_{IF}}$ = an intermediate frequency,

f_o = radio frequency

f_{LO} = local oscillator frequency,

m,n = $0, \pm 1, \pm 2 \ldots \infty$.

Additionally, the LO spur frequencies $f_{LO_{spur}}$ in turn generate products in downconversion:

$$f_{o_{IF_{spur}}} = mf_o + nf_{LO_{spur}}, \tag{2.2}$$

and likewise in upconversion:

$$f_{o_{spur}} = mf_{o_{IF}} + nf_{LO_{spur}}. \tag{2.3}$$

The frequencies $f_{o_{IF_{spur}}}$ and $f_{o_{spur}}$ must be sufficiently far from the passband to be efficiently filtered out. For example, as illustrated in Figure 9, the desired signal is the lower sideband $m,n = -1$ which crosses through the passband. No other products enter the passband, and all are sufficiently removed from the passband to be filtered effectively.

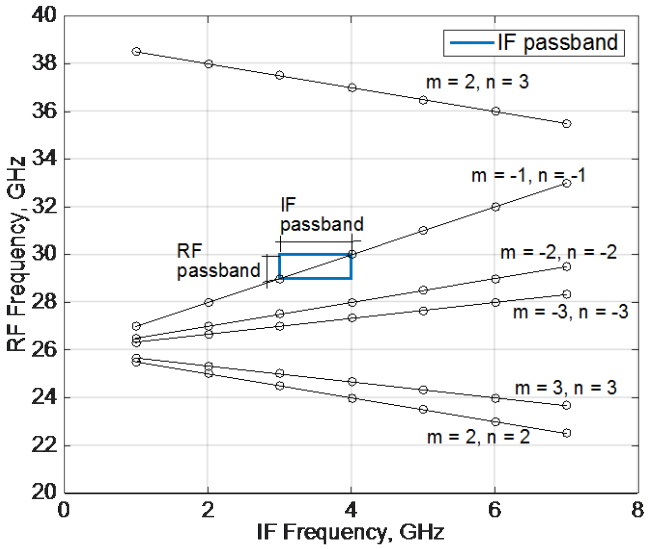

Figure 9. Spurious-Response for a 30 GHz Mixer. LO Frequency is 26 GHz. The IF Band is from 3 to 4 GHz.

Adapted from [18]: S. A. Maas, "System Considerations," in *Microwave Mixers*, Boston: Artech House, 1993, p. 182.

Third-order intermodulation should be avoided for heterodyne receivers since co-channel intermodulation can cause interference, whereas the second order intermodulation is worse for homodyne receivers because co-channel intermodulation might cause DC value insertion. A balanced mixer combined with a high Q oscillator might avoid some of these issues [10].

In [10] the authors present a concept of a balanced mixer integrated with oscillator that provides very accurate quadrature conversion, which reduces undesirable intermodulation products and additionally provides a precise LO reference for *I* and *Q*.

c. Direct Digital Synthesizer

The DDS is a component that uses digital signal processing to generate analog signals. DDS digital characteristics allow for a production of a variety of signals with precision and stability when compared with analog techniques. The DDS architecture, exemplified in Figure 10, comprises of frequency and phase accumulators, a lookup table and D/A converters [19].

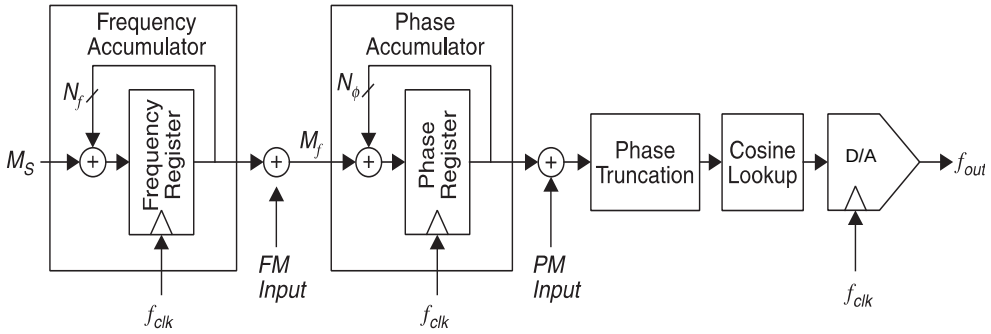

Figure 10. General DDS Architecture

Source [19]: M. I. Skolnik, *Radar Handbook*, 3rd ed., vol. 1. McGraw-Hill, 2008, p. 6.48.

B. SYNCHRONIZATION: LO DISTRIBUTION APPROACHES

A digital array requires accurate phase synchronization among all elements in order to achieve high performance beamforming. An inaccurate LO reference corrupts the waveform by introducing magnitude and phase errors, which causes distortions of the array pattern.

In order to maintain the array synchronization, three different LO distribution approaches can be taken:

1. Direct distribution of a single LO
2. Use of independent stable LOs (STALOs)
3. Phase estimation through a data network clock

Direct distribution of a LO through a wired or wireless channel is the simplest architecture to keep remote nodes synchronized. In a direct distribution scenario, the LO signal can be a single tone radio frequency transmitted from a controller to the elements. In an ideal hardwire distribution scenario, all cables should have the same length in order to guarantee the same phase reference for all nodes; however, this implementation may be impractical for large distributed arrays, demanding several of meters lossy coaxial cables installed along the platform.

Loke [12] and Tsai [13] tested a wireless LO distribution technique using variable phase shifters on T/R modules which consisted of increased phase delay on shorter path elements to match the delay of longer ones. This LO distribution technique required high power LO signal transmission to compensate for propagation spreading loss and deal with different path distances; for instance, Tsai in [13] used the modulator board AD8346 that requires LO input power within -6 and -12 dBm.

In 2006, Loke [12] investigated a ‘‘brute force’’ synchronization approach. A reference continuous wave (CW) signal was sent by the digital beamformer where one element was selected as master and other as slaves. The received CW from the master is transmitted back to beamformer and is used as a reference signal. The synchronization is performed one slave element at a time. The slave element gradually phase shifts its LO signal and transmits back to the beamformer. The beamformer verifies element synchronization by subtracting the reference (master) and element returns and searching for a null. The master and slave are synchronized when the null is achieved. If the algorithm is performed often, then slow channel changes will not affect array synchronization. During experiments, Loke [12] showed that the whole process requires only a few iterations to achieve sufficient phase synchronization.

The plot in Figure 11 is the residual phase error for simulation of synchronization for an array of 100 elements that are randomly located. After convergence the residual phase error is within ± 11.25 degrees using four bits of phase shift, which represents 22.5 degrees per iteration. An advantage of this approach, which uses a single common LO, is that frequency drift is common to all elements.

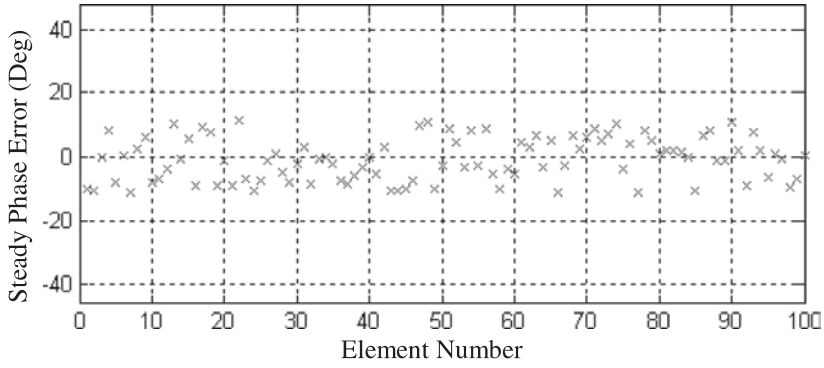

Figure 11. Residual Phase Error After Synchronization with 4-bit Phase Steps

Source: [12] Y. Loke, "Sensor synchronization, geolocation and wireless communication in a shipboard opportunistic array," M.S. thesis, Department of Electrical and Computer Engineering, Naval Postgraduate School, 2006.

In 2008, Djerf and Tornazakis [14] looked at two techniques for achieving stable local oscillators in the T/R module: (1) using phased locked loops (PLLs) or (2) using use demodulator boards to recover *I* and *Q* and estimate the phase through *I* and *Q* magnitude. A PLL has the ability to control a voltage controlled oscillator (VCO) based on a reference input signal, which can be a LO signal. The PLL can complement the direct distributed LO scheme because it does not require constant LO transmission and has the possibility of transmitting a lower frequency. A PLL in locked mode can synchronize an element using hardwire or wireless link connected to a digital beamformer using the process explained previously. After synchronization the PLL is set to hold-over mode.

Djerf and Tornazakis [14] investigated the use of demodulator boards to recover *I* and *Q*, where an independent LO is used for each element. For ideal components and the LO operating at nominal frequency, the baseband *I* and *Q* results in two DC valued signals that give the phase

$$\Phi = \tan^{-1}\left(\frac{Q}{I}\right). \tag{2.4}$$

This technique is sensitive to *I* and *Q* unbalance and AM noise; furthermore, the LO operating at exact nominal frequency is unlikely. In this case the phase error propagates to other components of T/R module, disrupting the array pattern.

Recently, many time and phase estimation techniques for wireless sensor networks (WSNs) have been studied using phase estimating algorithms through time stamps on data packets. One consolidated time-estimation protocol used for communications to data stream synchronization is the IEEE 1588 Precision Time Protocol (PTP); however, the accuracy of the recovered clock is still not sufficient for radars that employ frequencies higher than VHF. For example, in [16] Texas Instruments reported a test regarding clock synchronization using PTP. For the experiment a slave DP83640 device generated a 10-MHz nominal clock with 226 ps mean and 2.7 ns standard deviation using information transmitted through an Ethernet network. In other words, for a 10-MHz clock, 95.4% of the time the phase deviation is less than 20^{o} and clock frequency error is around 2200 parts per million (ppm).

C. SUMMARY

In this chapter, the basic T/R module architecture was presented along with the technological challenges for digital phased array development. In the next chapter the digital array theory is reviewed and a modified array factor model including phase errors is proposed.

THIS PAGE INTENTIONALLY LEFT BLANK

III. DIGITAL ARRAY THEORY

The concept and theory behind digital arrays is described in this chapter. The basic expression for array factor is used for both analog and digital arrays. For the latter, signals are synthesized at each element, emulating the effect of a beamforming network, and for this reason, the sources for phase errors are different than for analog arrays. A modified array factor taking into account the architecture specific magnitude and phase errors is derived, and expressions for gain and directivity are given.

A. ARRAY EQUATIONS

1. Array Pattern

The total pattern array is the joint contribution of all elements of the array. Each element is weighted to point the mainlobes of the transmission and reception patterns in the same direction. To compute the pattern it is necessary to specify the element locations and orientations. The frequency domain (phasor) expression for the pattern factor for an array of size *N*, for which elements are located at positions (x_n, y_n, z_n), $n = 1, 2, 3, \ldots, N$, as derived in [3] and [13] is

$$\overrightarrow{F}(\theta,\phi) = \sum_{n=1}^{N} W_n e^{j\vec{k}\cdot\vec{r}_n} \overrightarrow{EF}_n(\theta,\phi) \tag{3.1}$$

where

W_n = weight coefficient,

= $A_n e^{j\Psi_n}$, $\Psi_n = \psi_{s_n} + \psi_n$

A_n = magnitude of complex weight for the n^{th} element,

ψ_n = phase of complex weight for the n^{th} element,

ψ_{s_n} = beam scanning phase,

= $-k\left[u_s x_n + v_s y_n + w_s z_n\right]$

u_s = scan x direction cosine,

= $\sin\theta_s \cos\phi_s$

v_s = scan y direction cosine,

= $\sin\theta_s \sin\phi_s$

w_s = scan z direction cosine,

= $\cos\theta_s$

(θ_s, ϕ_s) = scanning angle,

$\vec{r}_n$ = position vector from array origin to n^{th} element,

= $\left[x_n\hat{x} + y_n\hat{y} + z_n\hat{z}\right]$

u = observation x direction cosine,

= $\sin\theta\cos\phi$

v = observation y direction cosine,

= $\sin\theta\sin\phi$

w = observation z direction cosine,

= $\cos\theta$

λ = wavelength.

The complex weight W_n is set for beam scanning, sidelobe control and phase corrections.

2. Element Factor

The characteristics of an array beam pattern are also dependent on the electric field radiation pattern of the individual elements, called the element factor (EF). The EF is the electric field pattern due to the current flowing on the antenna. We assume that the

array is large so that mutual coupling variations can be ignored and all element patterns are identical.

The element factor of a general cosine type pattern in the direction $\hat{\boldsymbol{r}}$ is expressed as [13]

$$\overrightarrow{EF} = \begin{cases} \hat{p}\left|\hat{n}\bullet\hat{r}\right|^{q}, & \hat{n}\bullet\hat{r}>0 \\ 0 \quad\quad , & \text{otherwise} \end{cases} \tag{3.2}$$

where the exponent q controls the half-power beamwidth (HPBW). The unit vector $\hat{\boldsymbol{p}}$ is added to indicate polarization direction. For example, for an element beam pointing along the z-axis $(\hat{\boldsymbol{n}}=\hat{z})$, a general far-field linearly polarized element factor can be expressed as

$$\overrightarrow{EF} = EF\hat{p} = EF(\hat{\theta}\cos\phi + \hat{\phi}\sin\phi)\frac{e^{jkr}}{r} \tag{3.3}$$

where

EF = element factor, and

$\hat{p}$ = polarization vector.

For a distributed array the element pointing directions and polarizations can vary. For a planar array with uniform element spacing and alignment, the polarization vectors and normal vectors are the same for all elements. When calculating the array radiation properties only the normalized EF is needed. A convenient expression for the element factor is a cosine to a power q as defined in (3.2).

Another concern regarding element pattern is the field-of-view (FOV), which is generally considered to be the element's HPBW. For uniform arrays, all elements have the same FOV. In contrast, arrays distributed along curved surfaces have elements that might not be able to illuminate the target due to obstruction or limitation of their FOV [3]; hence, these obstructed elements do not contribute to the array pattern and $EF=0$.

Given identical element factors, (3.1) can be reduced to

$$\vec{F}(\theta,\phi) = \overrightarrow{EF}\left(\sum_{n=1}^{N} W_n e^{j\vec{k}\bullet\vec{r}_n} \right) = \overrightarrow{EF}\, AF \tag{3.4}$$

where the sum in parentheses is the array factor (*AF*)

$$AF = \sum_{n=1}^{N} W_n e^{j\vec{k}\bullet\vec{r}_n}. \tag{3.5}$$

For the remainder of this study we focus on the properties of the array factor and suppress EF. With regard to (3.4) we consider *F* to be a complex scalar equal to *AF*.

3. Array of Subarrays

The use of subarrays is motivated by the difficulty in allocating sufficient area of a platform surface for a large array. Breaking the array into smaller subarrays and having them installed in noncontiguous (separated) areas minimizes the impact of the array on the platform structure. On the other hand, the received and transmitted signals from multiple subarrays must be coherently processed.

Consider a collection of *M* arrays, $m = 1,2,3\ldots M$ where the subarray centers are at $[x_s(m), y_s(m), z_s(m)]$, as illustrated in Figure 12. Let $F_m(\theta,\phi)$ be the array factor for the m^{th} subarray. In this case the total array factor of the combined subarrays is expressed as [9]

$$F(\theta,\phi) = \sum_{m=1}^{M} F_m(\theta,\phi) \exp\left\{ jk\left(\left[x_s(m)(u-u_s) \right] + \left[y_s(m)(v-v_s) \right] + \left[z_s(m)(w-w_s) \right] \right) \right\} \tag{3.6}$$

where $F_m(\theta,\phi)$ is the array factor for the subarray *m* as given in (3.5).

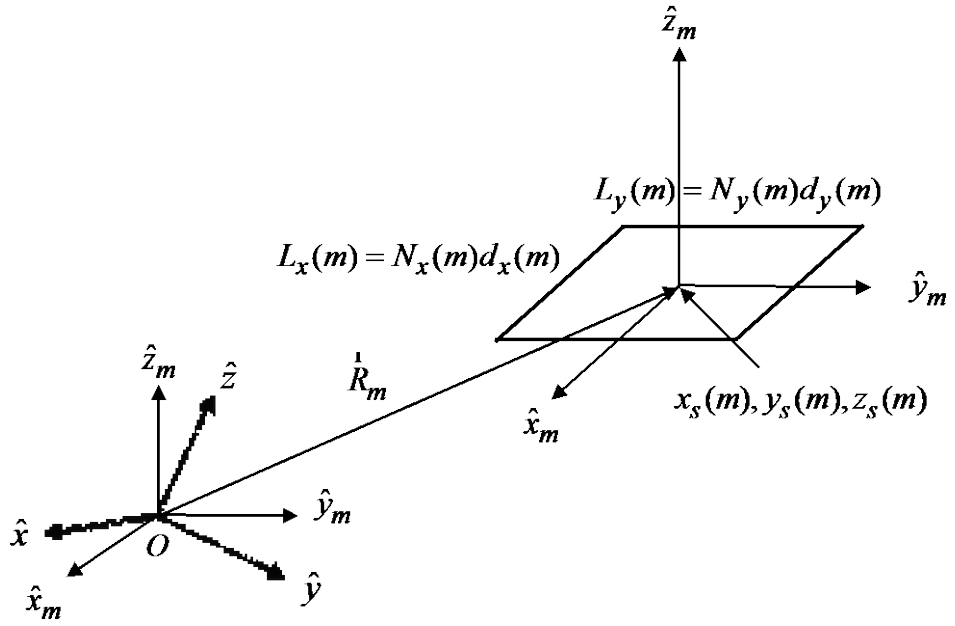

Figure 12. Subarray *m* and its Local Coordinate System Relative to the Global Origin O.

Source: B. Feng, D. C. Jenn, and S. Member, "Two-Way Pattern Grating Lobe Control for Distributed Digital Subarray Antennas," *IEEE Trans. On Antennas Propag.*, vol. 63, no. 10, pp. 4375–4383, 2015.

4. Including Phase Errors in the Array Factor

The precision of pattern control depends on two main factors: the application of the correct value for complex scanning weights W_n for each element and the knowledge of the exact location of the elements; therefore, the use of non-ideal devices that might insert magnitude and phase errors must be accounted for in array design [11]. The effects on the pattern can include loss in gain, increased sidelobe levels, beam pointing errors and increased cross polarization.

Many factors contribute to deviations in phase. The passive microwave circuitry in the antenna is one source and can be considered to be independent of time. Other phase errors (as well as amplitude errors) are introduced in the mixing process. Phase noise, phase offset and inaccurate frequency are some problems found in non-ideal devices. Likewise, magnitude error can occur in any stage of transmission and reception due to gain mismatch, interference, or noise. This type of error can affect the sidelobe level

when using taper to lower sidelobes. Furthermore, array elements are likely to be physically displaced by a fraction of wavelength, which is caused by array surface deflection, installation errors and surface vibration; thus, when elements are displaced from their designed location, phase errors increase.

a. Random Phase Noise

The phase noise represents frequency fluctuations, which have their origin in either internal devices or external phenomena, such as mechanical vibrations and electromagnetic interference. For timing and metrology, instead of phase noise in the frequency domain, one can measure jitter, which is a time fluctuation. For RF design purposes, phase noise is preferred because it is obtained directly from a spectrum analyzer [15].

Phase noise is modeled as frequency-selective random process and is characterized using the *power-law model*, which is composed by five types of noise, discussed further in Section IV.A.3:

1. Random walk frequency modulation noise
2. Flicker frequency modulation noise
3. White frequency modulation noise
4. Flicker phase noise
5. White phase noise

By integrating the phase noise over the signal bandwidth, one obtains the RMS value for random phase deviation $\varphi(t)$, where φ is the symbol used for phase noise, whereas ϕ is the spherical azimuth variable, and

$$\varphi_{RMS} = \left[\int_{f_R}^{\infty} S_{\varphi}(f)\,df \right]^{1/2} \tag{3.7}$$

where

f_R = starting reference frequency far from signal of interest ($f_R >> f_o$), and

S_φ = phase noise spectrum.

Notice the expression for φ_{RMS} is bandwidth dependent; hence, the use of a narrowband source is preferable. For example, the phase noise inserted by a crystal oscillator is usually small because this type of oscillator usually has a high Q factor [10].

Although the random phase deviation $\varphi(t)$ is not constant over time, if $\varphi(t)$ can be modeled as a wide sense stationary process, then at time t_o, the phase deviation can be expressed as $\varphi(t_o) = \varphi$, which is independent from the time origin. In this case the random phase model is accounted in the array factor expression (3.5) by adding $e^{j\varphi_n}$, which is the phase error due to phase noise at the n^{th} element. The modified expression of array factor including phase noise is

$$AF(\theta,\phi) = \sum_{n=1}^{N} W_n e^{j\vec{k}\bullet\vec{r}_n} e^{j\varphi_n}. \tag{3.8}$$

b. Scan Weight Errors

In (3.5), the term W_n represents the n^{th} element complex weight. This coefficient is precisely selected in order to coherently phase the element transmissions and receptions to obtain the maximum gain for a chosen direction ψ_{s_n}. The magnitude of W_n is also used to control sidelobe levels through tapering. In a digital array, the coefficient is obtained through quadrature modulation.

The complex weight is a part of the array factor expression and is expressed in polar or rectangular form as

$$W_n = A_n e^{\Psi_n} = A_n\left[\cos(\Psi_n) + j\sin(\Psi_n)\right] \tag{3.9}$$

where $\Psi_n = \psi_{s_n} + \psi_n$. The weight is upconverted to RF frequency $\left(\omega_o = 2\pi f_o\right)$ to the in-phase and quadrature signals given, respectively, by

$$I_n(t) = \mathrm{Re}\left\{ A_n e^{\Psi_n} \right\} \cos(\omega_o t) = A_n \cos(\Psi_n) \cos(\omega_o t) \tag{3.10}$$

and

$$Q_n(t) = \mathrm{Im}\left\{ A_n e^{\Psi_n} \right\} \cos(\omega_o t) = A_n \sin(\Psi_n) \sin(\omega_o t). \tag{3.11}$$

The result after subtracting (3.10) from (3.11) is

$$S_n(t) = A_n \cos(\omega_o t + \Psi_n). \tag{3.12}$$

The expression for $S_n(t)$ represents the transmitted RF signal by the n^{th} element. The polar form of the complex weight is obtained from the relationships

$$A_n = \sqrt{I_n^2(t) + Q_n^2(t)} \tag{3.13}$$

and

$$\Psi_n = \tan^{-1}\left(\frac{Q_n(t)}{I_n(t)} \right). \tag{3.14}$$

For demodulation, the received signal is downconverted to *I* and *Q* channels using a process similar to transmission. Let $R_n(t)$ be the received RF signal by the n^{th} element, which is expressed as

$$R_n(t) = K_n(t) \cos\left[\omega_o t + \kappa_n(t) \right] = \mathrm{Re}\left\{ \left[K_n(t) e^{j\kappa_n(t)} \right] e^{j\omega_o t} \right\} \tag{3.15}$$

where $K_n(t) e^{\kappa_n(t)}$ is the received signal complex envelope. A low pass filter is applied to reject the high frequency component [20]. For direct downconversion, the expression for $I_n(t)$ is

$$
\begin{aligned}
I_n(t) &= LPF\left\{R_n(t)\cos(\omega_o t)\right\} \\
&= \frac{1}{2} LPF\left\{\mathrm{Re}\left(K_n(t)\left[e^{j\kappa_n(t)} + e^{j\left(\kappa_n(t)+2\omega_o t\right)} \right]\right)\right\} \\
&= \frac{1}{2} K_n(t)\cos\left[\kappa_n(t)\right]
\end{aligned}
\tag{3.16}
$$

where $LPF\left\{\cdot\right\}$ denotes a low-pass filter operator. Similarly,

$$
\begin{aligned}
Q_n(t) &= LPF\left\{R_n(t)\sin(\omega_o t)\right\} \\
&= \frac{1}{2} LPF\left\{\mathrm{Re}\left(K_n(t)\left[e^{j\kappa_n(t)} + e^{j\left(\kappa_n(t)+2\omega_o t\right)} \right]\right)\right\} \\
&= \frac{1}{2} K_n(t)\sin\left[\kappa_n(t)\right].
\end{aligned}
\tag{3.17}
$$

The $I_n(t)$ and $Q_n(t)$ are sampled and recombined in the digital domain and the complex envelope is recovered. Lastly, the $I_n(t)$ and $Q_n(t)$ are multiplied by the complex weight W_n in order to obtain the maximum radiated power in the scanned direction set by phase shift ψ_{s_n}.

Any unknown magnitude and phase errors that modify $I_n(t)$ and $Q_n(t)$ during the demodulation process are not incorporated into the complex weight coefficient. Consequently, these errors change the array factor; therefore, one quadrature modulation and demodulation weakness is the required balance between *I* and *Q* channels.

The following sources can lead to significant phase and amplitude errors [20]:

1. Phase error between the *I* and *Q* channels
2. Differential gain error between the two channels
3. Leakage of the LO signal
4. DC offsets in the *I* and *Q* signals

An expression for complex weight accounting for quadrature errors is

$$W_n = (1+\delta_n) A_n e^{j(\Psi_n+\epsilon_n)} \tag{3.18}$$

where $\boldsymbol{\delta_n}$ is the magnitude error and ϵ_n is the phase error.

Introducing the modified complex scan weight into array pattern expression of (3.5), we get

$$AF(\theta,\phi) = \sum_{n=1}^{N} W_n e^{j\vec{k}\bullet\vec{r}_n} = \sum_{n=1}^{N} (1+\delta_n) A_n e^{j(\Psi_n+\epsilon_n)} e^{j\vec{k}\bullet\vec{r}_n}. \tag{3.19}$$

c. Element Location Errors

The array factor term $e^{j\vec{k}\bullet\vec{r}_n}$ is the phase shift to element *n*. By knowing this information, we can set the scan weight to cancel this phase effect in the direction of the beam; however, in case of imprecise location of the element, this can cause a phase error that affects the beam pattern. If the element position is expressed as [12]

$$\vec{r}_n = \vec{r}_{on} + \Delta\vec{r}_n = \left[(x_n+\Delta x)\hat{x} + (y_n+\Delta y)\hat{y} + (z_n+\Delta z)\hat{z}\right], \tag{3.20}$$

the array factor described in (3.5) can be rewritten as

$$AF(\theta,\phi) = \sum_{n=1}^{N} W_n e^{j\vec{k}\bullet(\vec{r}_{on}+\Delta\vec{r}_n)} = \sum_{n=1}^{N} W_n e^{j\vec{k}\bullet\vec{r}_{on}} e^{j\vec{k}\bullet\Delta\vec{r}_n}. \tag{3.21}$$

Note that the phase error due to element displacement is angle dependent.

d. Final Expression for Array Factor

In summary, the phased array is sensitive to phase and magnitude errors caused by random phase noise, quadrature modulation and demodulation errors, and element dislocation. Considering all the possible phase and magnitude errors, we get the final expression for array factor as

$$AF(\theta,\phi)=\sum_{n=1}^{N}\left[(1+\delta_n)e^{j(\varphi_n+\epsilon_n+\vec{k}\bullet\Delta\vec{r}_n)}\right]A_n e^{j\Psi_n}e^{j\vec{k}\bullet\vec{r}_{on}} \tag{3.22}$$

where $\left(\varphi_n+\epsilon_n+\vec{k}\bullet\Delta\vec{r}_n\right)$ is the total phase error due to phase noise, *I* and *Q* unbalance and localization errors, whereas $(1+\delta_n)$ is magnitude error.

5. Directivity and Gain

The directivity is an important characteristic of antenna performance and can be expressed in terms of normalized pattern factor $F_{norm}(\theta,\phi)$[3]:

$$D(\theta,\phi)=\frac{4\pi}{\int_0^{2\pi}\int_0^{2\pi}\frac{|F(\theta,\phi)|^2}{|F_{max}|^2}\sin\theta\,d\theta\,d\phi}=\frac{4\pi}{\int_0^{2\pi}\int_0^{2\pi}|F_{norm}|^2\sin\theta\,d\theta\,d\phi}. \tag{3.23}$$

In the case of a lossy array, the gain can be computed from the directivity by including the antenna efficiency η[3]:

$$G(\theta,\phi)=\eta D(\theta,\phi)=\frac{4\pi A_e}{\lambda^2}|F_{norm}(\theta,\phi)|^2 \tag{3.24}$$

where

η = the antenna efficiency, $0\le\eta\le 1$,

= P_{rad}/P_{in}

P_{rad} = power radiated by the antenna,

P_{in} = power into the antenna, and

A_e = the array effective area.

The peak gain G_o is the maximum value of the gain [3], $G_o=\max\{G(\theta,\phi)\}$. Except for very simple antennas, the integral in (3.23) must be evaluated numerically.

6. Array Average Power Pattern and Sidelobe Level

There are two approaches to evaluate the effect of amplitude and phase errors on array performance. The errors can be modeled as random and Monte Carlo simulations can be performed. A large number of independent trials are conducted and the results averaged to estimate the expected gain, sidelobe level and beam pointing error. This is the approach taken in Chapter V.

The array average power pattern is equivalent to averaging the square of the absolute value of the array pattern, given by (3.1), which represents the radiated electric field. For an array with N elements, the average power pattern was derived in [3]. Assuming small, zero mean Gaussian errors, we get

$$\langle P \rangle = \left| \langle F(\theta,\phi) \rangle \right|^2 \left(1 - \frac{1}{N} \right) + \frac{1}{N} \tag{3.25}$$

where $\langle \cdot \rangle$ denotes expected value. The first term is the error free pattern reduced in intensity. The second term is the average sidelobe level.

The expected power of the main lobe is

$$\langle P_{mainlobe} \rangle = \left| \langle F(\theta,\phi) \rangle \right|^2 \left(1 - \frac{1}{N} \right) \tag{3.26}$$

and the average side lobe ratio

$$\frac{\langle P_{sidelobe} \rangle}{\langle P_{mainlobe} \rangle} = \frac{1}{N}. \tag{3.27}$$

B. SUMMARY

In this chapter the digital array theory was reviewed by revisiting the expressions for calculation of the array pattern, element factor, array factor, gain and sidelobe level, and modified equations were proposed for the array pattern, including phase errors, which are used in Chapter V simulations. In the next chapter the mathematical model for instantaneous phase for non-ideal LO and the random phase noise model, which is used in array pattern simulations, is presented.

IV. TIMING AND SYNCHRONIZATION

Operation of a distributed digital array relies on phase and time synchronization of large number of elements in order to coherently process transmitted pulses and achieve high efficiency. Even though time and phase synchronization are closely related, these concepts are applicable to different situations.

In order to describe time synchronization, first it is necessary to define *chronosignal* or *timing signal*, which is a signal used to control actions that are required to be timed and is generated by a clock [15]. Ideally, clocks with identical frequency generate chronosignals that differ only by a constant offset, but in reality not even the world's most important time standard is perfectly synchronized with the Earth's rotation clock standard. The coordinated universal time (UTC) is periodically adjusted using leap seconds to keep synchronized with legacy standard. The leap second information is transmitted for applications that use UTC as a standard [21]; therefore, the notion of time synchronization depends on the application. The definition from [22] considers two clocks to be synchronized if both have the same time origin and time interval and do not differ by a specified uncertainty.

Phase is also a linear function of time, but phase has a physical meaning for periodic signals. To perform a frequency demodulation, the received signal and local oscillator must be phase synchronized, i.e., locked; even if the signal phases are 360 degrees apart, they remain synchronized because of the periodicity.

Every distributed sensor network requires time synchronization, and many improvements have been achieved in recent years to provide better performance. Likewise, a digital array radar is a type of sensor network, consisting of nodes that transmit and process radar pulses coherently. A digital array also demands phase synchronization for beamforming purposes.

A. TIME AND PHASE SYNCHRONIZATION

A mathematical model for timing signals, generally used for clock and oscillator characterization, is described in this section. The type of oscillator depends upon the design and application. There are a variety of devices available on the market using different technologies such as those described in the Appendix.

In [15] the author divides clocks in two groups: autonomous and slave clocks. Autonomous clocks are those that have an internal oscillator and do not depend on external influence to supply a timing signal, such as crystal oscillators; slave clocks are those that require external control.

1. Frequency, Phase and Time Models

The model used in [15] to depict the behavior of instantaneous frequency in real clocks consists of three terms given by

$$f(t) = f_s + f_d(t) + f_a(t) \tag{4.1}$$

where

f_s = starting frequency,

= $f_n + f_{offset}$

f_n = nominal frequency,

f_{offset} = frequency offset,

$f_d(t)$ = frequency drift, and

$f_a(t)$ = random frequency.

This definition is not specific for a particular oscillator or signal. Any synthesized continuous wave (CW) signal is subject to these phenomena. Although the focus here is the local oscillator frequency errors $f_{LO,}$ (4.1) is also applied for errors in f_o and f_{oIF}.

The starting frequency is a constant value and includes the oscillator nominal frequency plus an initial calibration error; in other words, it is the device initial accuracy. Another factor that affects the instantaneous frequency is the drift, which is a time-dependent factor, and older devices tend to be less accurate. Usually, frequency drift is approximated by a linear function, called linear fractional frequency drift rate [15]:

$$f_d(t) = Df_n t \tag{4.2}$$

where *D* is the linear fractional frequency drift rate.

The last term in (4.1) is a random frequency deviation that represents the oscillator phase noise

$$f_a(t) = \frac{1}{2\pi}\frac{d\varphi}{dt} \tag{4.3}$$

where the term φ represents the random phase deviation, and the instantaneous frequency expression can be rewritten as

$$f(t) = f_s + Df_n t + \frac{1}{2\pi}\frac{d\varphi}{dt}. \tag{4.4}$$

Consequently, from (4.4) it is possible to derive an expression for instantaneous phase

$$\Phi(t) = 2\pi f_s t + Df_n t^2 + \varphi(t) + \Phi_o \tag{4.5}$$

where Φ_o is the initial phase. Finally, the expression for a time signal generated by an oscillator is

$$T(t) = \frac{\Phi(t)}{2\pi f_n}. \tag{4.6}$$

Note that for the ideal case, where $D = 0,\ \varphi(t) = 0$ and $\Phi_o = 0,$

$$T(t) = \frac{\Phi(t)}{2\pi v_n} = \frac{2\pi v_n t}{2\pi v_n} = t. \tag{4.7}$$

2. Accuracy and Drift

The maximum frequency error of a clock during its life cycle determines the accuracy. Frequency error is mainly affected by the offset and drift and is expressed as a ratio of clock deviation to its nominal frequency [15]

$$f_{\epsilon} = \frac{\Delta f_{max}}{f_n} \tag{4.8}$$

where Δf_{max} is the maximum frequency deviation.

The oscillator frequency drifts due to internal or external phenomena. The main internal factor is the aging of the oscillator components; although, it is very difficult to determine an exact reason for internal drift [15].

Drift can also occur by external factors such as interference, temperature and vibration. Oscillators in modulators and demodulators are subject to injection pulling and locking, i.e., a frequency disturbance due to influence of an external signal which is close in frequency to that second oscillator or device. When the oscillator starts to resonate with the frequency of the disturbance, this is called injection locking, but if two frequencies remain different, this is called injection pulling [23].

Frequency accuracy is essential for distributed array functioning. A slight frequency deviation, after a long period of time, might represent a significant phase difference that degrades pattern characteristics.

3. Phase Noise

Phase noise is composed by the oscillator frequency and amplitude fluctuations affecting other components that use this signal as reference. There are other sources of phase noise, but oscillators tend to increase the noise close to its resonance and harmonics [24]. For this reason, after the mixing process, oscillator noise is more significant than other contributors.

Phase noise can be characterized in the time domain or the frequency domain. Time-domain models observe deviations during a period of time and establish a statistical

model by measuring the Allan variance, for instance. In metrology, time-variance measurements, such as the Allan variance, are preferable because long-term variations are registered. Furthermore, frequency-domain model parameters are estimated from time-domain observations, which also include drift effects [15]. The model used in this thesis assumes independent phase noise and drift.

Frequency-domain models have been used for decades and accurately represent oscillator noise over short time intervals. Moreover, frequency-domain phase noise can be obtained directly from a spectrum analyzer, simplifying oscillator design and characterization [10].

a. Power-Law Model

To characterize the oscillator phase noise, the *power-law* model is usually used, which is expressed as one-sided, power spectral density (PSD) of random time deviation $\tau(t)$ [15]

$$S_\tau(f) = \begin{cases} \dfrac{1}{(2\pi)^2} \displaystyle\sum_{\alpha=-4}^{0} h_{\alpha+2} f^\alpha, & 0 \le f \le f_h \\ 0, & f > f_h \end{cases} \tag{4.9}$$

where $h_{-2}, h_{-1}, h_0, h_1, h_2$ are device-dependent coefficients. Each particular clock is defined by a set of coefficients. The term f_h is the oscillator bandwidth cut-off frequency. The relationship between random time deviation and random phase deviation is

$$\tau(t) = \frac{\varphi(t)}{2\pi f_n}. \tag{4.10}$$

Consequently, the power spectra are related by

$$S_\tau(f) = \frac{S_\varphi(f)}{(2\pi f_n)^2}. \tag{4.11}$$

The phase noise power is related to the RMS value of the random phase deviation φ_{RMS}, expressed in (3.7). The parameters h_{-2}, h_{-1}, h_o, h_1, h_2, are related to five different types of noise components:

1. Random walk frequency modulation $\left[h_{-2}/f^4\right]$

Random walk frequency modulation (RWFM) is the part of phase noise attributed to environmental perturbation such as mechanical shocks, temperature variation [15], and random changes in oscillator frequency [25]. RWFM has main frequency components close to oscillator resonance. For this reason it is more significant near these frequencies and also more difficult to measure [15].

2. Flicker frequency modulation $\left[h_{-1}/f^3\right]$

The source for flicker frequency modulation (FFM) is attributed to a physical resonance mechanism of an oscillator or issues controlling electronic components. Some oscillators might not show FFM noise, which might be covered by white frequency modulation (WFM) or FPM, but in high quality factor oscillators, FFM is more significant.

3. White frequency modulation $\left[h_o/f^2\right]$

White frequency modulation is generated by electronic components, and for most oscillators, white frequency noise is less significant close to the resonance frequency [25].

4. Flicker phase modulation $\left[h_1/f\right]$

Flicker phase modulation (FPM) is a colored type of noise and is related to oscillator resonance mechanism. In mixing and amplification, the local oscillator noise is amplified, especially close to carrier frequencies [15].

5. White phase modulation $\left[h_2\right]$

White phase modulation (WPM) noise is a wideband, uncorrelated noise with constant magnitude over the spectrum and can be interpreted as a phase noise floor. The main source for WPM is the noise inserted by electronic devices. Even though oscillators

have low WPM noise, circuits that employ digital devices increase WPM due to errors in clock reference and phase quantization errors [15].

The PSD of random time deviation in its components is shown in Figure 13, and an example of phase noise from VCO manufacturer Minicircuits is shown in Figure 14.

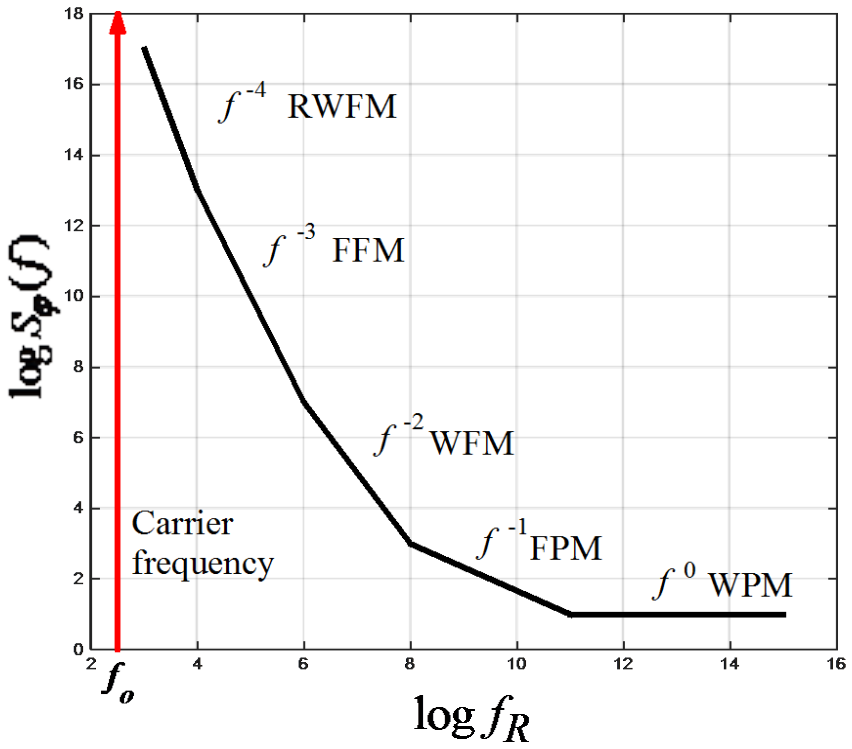

Figure 13. Random Time Deviation PSD Obeying the Power-Law Model Plotted on a Log-Log Diagram

The frequency f_R is a reference frequency far from the carrier frequency. The figure of interest is the area under the phase noise curve, which represents the power and is related to random phase deviation. Adapted from [15]: S. Bregni, *Synchronization of Digital Telecommunications Networks*, Vol. 1. John Wiley & Sons, 2002, p. 248.

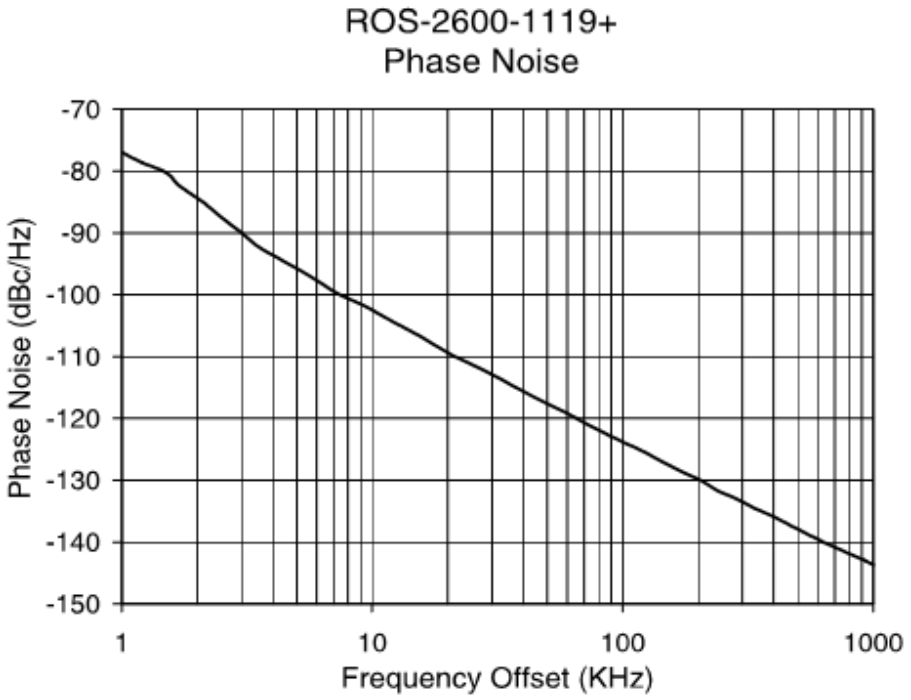

Figure 14. Phase Noise of the Voltage Controlled Oscillator Model ROS-2600-1119, Manufacture Minicircuits

Source [26]: (2015, Nov. 10) Voltage Controlled Oscillator ROS-2600-1119+. [Online]. Available: http://www.minicircuits.com/pdfs/ROS-2600-1119+.pdf.

b. Leeson's Equation

In 1966, Leeson [27] showed "a heuristic derivation, presented without formal proof" of the phase noise for an oscillator. The linear time-invariant theory assumes the oscillator is a linear device with some correction to account for its non-linearities. His first expression for phase PSD is [28]

$$S_{\varphi} = \left(\frac{N_F K_B T_S}{P_{out}}\right)\left[1+\left(\frac{f_o}{2Qf_R}\right)^2\right] \tag{4.12}$$

where

N_F = an empirical noise factor,

Q = oscillator open-loop unloaded Q-factor,

f_o = carrier frequency (RF),

f_R = reference frequency in signal bandwidth,

P_{out} = output power,

K_B = Boltzmann's constant ($= 1.38 \times 10^{-23}\,\mathrm{JK}^{-1}$), and

T_s = system temperature (in Kelvin).

In reference [28] the author describes a modified model including the flicker noise effects. The phase noise is usually given as a dB quantity

$$\mathcal{L}(f_m) = 10\log\left[\frac{1}{2}S_\varphi\right] \quad \text{dBc/Hz.} \tag{4.13}$$

The simplicity of this model is the great advantage over the power-law. While the power-law model requires measurements to estimate the coefficients h_{-2}, h_{-1}, h_0, h_1, h_2, Leeson's equation accounts for other oscillator parameters that are easier to obtain; moreover, this model includes frequency dependence for the phase noise. In upconversion, the ratio f_o/f_m increases the noise, adding a factor of 20 dB/decade, which is significant for high frequency radar applications.

For example, in [29] the author gave an example of a LO signal in the range of 5 GHz which was generated from a 10-MHz crystal oscillator using a frequency multiplication. This process increases the phase noise by

$$\begin{aligned}\mathcal{L}(5\text{ GHz}) &= (20\text{ dB/decade})(10\log 500) + \mathcal{L}(10\text{ MHz}) \\ &= (20\text{ dB/decade})26.99 + \mathcal{L}(10\text{ MHz}) \\ &= 53.9 + \mathcal{L}(10\text{ MHz})\text{ dB}.\end{aligned} \tag{4.14}$$

Consequently, the RMS phase noise increases by 245,470.

B. TIME AND PHASE SYNCHRONIZATION TECHNIQUES

Applications that require coherent detection and transmission, like phased array antennas, need carrier, bit and word synchronization [30]. In phase-coded CW radars, these three levels can be translated as carrier, subcode and code synchronization.

The most critical is the carrier synchronism because it requires errors smaller than a fraction of cycle, which can be sub-nanosecond for microwaves. Code and subcodes are more resilient to synchronization errors than the carrier. For example, a subcode period of 20 ns is used to achieve a 3.0-m range resolution, whereas a code period is 260 ns if a Barker code modulation of length 13 is used. Nevertheless, all three levels of synchronization are important to coherent transmission of the pulse and further detection.

In order to limit our discussion, time synchronization as a high level requirement is considered to assure code and subcode coherence; whereas, phase synchronization is required for a phased array beamforming. The time estimate can be extracted through some communications protocols such as network time protocol (NTP) or precision time protocol (PTP).

1. Phase and Frequency Synchronization Using Phased Locked Loop

For a distributed array, two-step synchronization is proposed: frequency and phase synchronization. In communications, coherent detection also requires carrier frequency recovery either from a pilot channel or through received signal [30]. The former is equivalent to a direct distribution LO introduced in Chapter II.B.1, and the latter uses a VCO. For carrier extraction from a received signal, a PLL is used to control the demodulator local oscillator; this architecture is known as a Costas loop. Once the local oscillator is synchronized to the received signal, coherent quadrature demodulation can be performed. We briefly introduce the important PLL concepts and operating modes.

a. Phased Locked Loop

A PLL is a type of slave clock that generates a timing signal controlled by a reference input. PLLs are widely employed in frequency synchronization. Despite the

name, PLLs are also used as non-linear filters and in modulation, demodulation and frequency synthesis [15]. The basic loop, illustrated in Figure 15, is composed of the following:

1. Phase Detector
2. Loop Filter / Amplifier
3. VCO

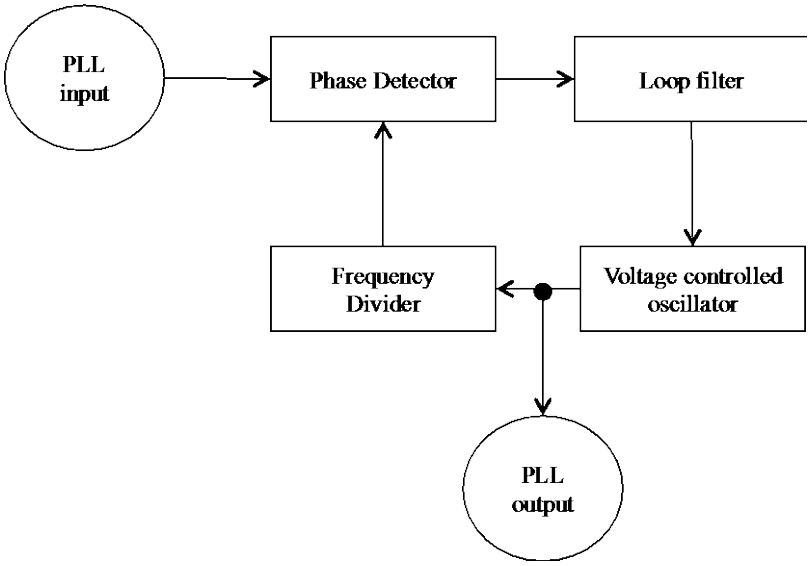

Figure 15. Block Diagram of PLL

Adapted from [15]: S. Bregni, *Synchronization of Digital Telecommunications Networks*, vol. 1. John Wiley & Sons, Ltd, 2002.

The phase detector (PD) is a non-linear circuit that compares the reference signal phase and the output from the VCO. If the VCO frequency is close to the reference input, then a low frequency output is expected from the PD. A low pass filter is used to eliminate PD noise and harmonics, and its output is feedback to the VCO. When the frequency is locked, the VCO input becomes a DC voltage.

A PLL has three operation modes:

1. Locked Mode: In locked mode the PLL is tracking the reference frequency. For an ideal case, the locked mode is receives a stable and continuous reference signal, but in real applications, noise, interference and component malfunctioning can corrupt the PLL

input. For this reason the locked mode operates in stressed mode, which means the PLL "incorporates phase build-out features to limit time-keeping error on transients after micro-interruptions" [15].

2. Free-run mode: In free-run mode, the PLL operates as an oscillator, supplying an output signal and disregarding the input reference. In fact, it is very rare that a PLL operates in free-run mode; it is preferable to run it in hold-over mode.

3. Hold-over mode:Similar to free-run, when the PLL is in hold-over mode, it generates a signal autonomously when the input reference fails; however, a PLL in hold-over mode keeps constant the voltage that feeds the VCO, using the last value before the reference interruption. A PLL might even store several past values, and in case of interruption the VCO is controlled using some estimation of these values.

b. Costas Loop

The Costas loop is a PLL application for carrier frequency and phase recovery. The block diagram is illustrated in Figure 16. The loop is a coherent quadrature demodulator with a VCO. The operation is similar to a PLL; however, the difference is that the output signal is not the oscillator reference, but the demodulated signal.

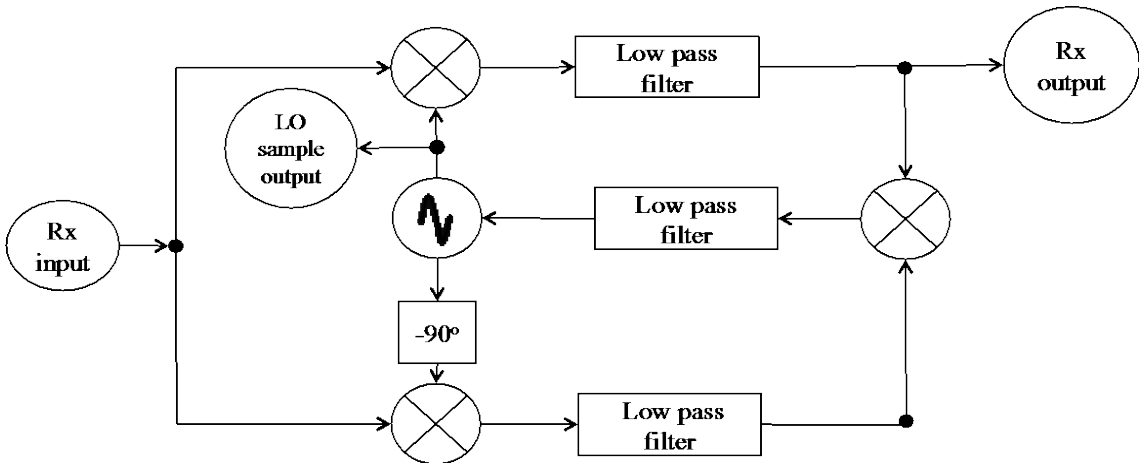

Figure 16. Block Diagram of Demodulator using Costas Loop

Adapted from [30] B. P. Lathi, *Modern Digital and Analog Communication systems*, 2nd ed. Sacramento, CA: The Dryden Press, 1989.

c. Synchronization Using PLLs

The DBF transmits the control signals to elements through a RF channel, which can be wired or wireless. A PLL can recover the carrier frequency and use it as a reference to generate a LO signal, which might have a frequency higher than its reference. The reason is because radars usually operate at frequencies in the S, X and K bands, whereas the WLAN might be at 2.4 GHz.

A Costas loop at each element recovers the frequency and phase of the received signal; however, the carrier cannot be used directly as LO because the link distance adds a time delay, which cannot be neglected. The elements are subjected to different delays because of their various distances to the DBF. The use of phase shifting to compensate the delay was experimented by Loke [12] and Tsai [13] in a brute force synchronization approach, which achieved synchronization phase errors as low as 22.5 degrees.

In [12] and [13], the authors used a circulator to isolate the received broadcasted LO signal from the element LO signal that is returned to the DBF for comparison with a master. The PLL synchronization eliminates this device since the LO is extracted from WLAN signal, and an independent path is used to transmit back the LO signal to the DBF.

Once the phase shifters are set and the PLL is locked to the reference, the element synchronization is accomplished. Theoretically, the element might not lose synchronization unless the frequency of the DBF reference carrier changes.

There is a limitation with this technique. The WLAN or wired LAN must have a single carrier frequency. Frequency-hopping channels, like WLAN standards IEEE 802.11 n/g, might not provide the PLL a stable LO.

2. Phase and Frequency Synchronization Stable Local Oscillator

A STALO can be used for phase and frequency synchronization of a digital distributed array. One example of a STALO is a chip scale atomic clock (CSAC) [31], which is a single frequency clock reference that can be used directly with a digital signal processing device, like a DDS, or feeding a PLL to synthesize a high frequency.

With the CSAC, phase synchronization can be achieved using digital delays once the output signal is a square shape waveform. The CSAC also provides a pulse per second (PPS) input for synchronization which can be used after compensating for the link distance delay.

C. SUMMARY

In this chapter a mathematical model for non-ideal LOs which have phase noise and inaccurate frequency was presented. Additionally, LO distribution techniques that can minimize phase errors were presented.

Results from parametric simulations programmed in MATLAB are presented in Chapter V, with the objective of illustrating the effects of phase errors on pattern distortions and to aid the array design process to set acceptable limits for these types of errors. These simulations were based on the models and equations presented in this chapter and Chapter III.

V. SIMULATIONS AND RESULTS

A. INTRODUCTION

A digital array beamformer controls each array element to generate the waveform and radiation pattern. The fact that all elements operate individually allows for the correction of phase and magnitude errors that originate during implementation [3].

There are random errors that are very difficult to eliminate or compensate. In large arrays these errors can limit the minimum sidelobe level and maximum array gain [32]. The block diagram in Figure 17 depicts the T/R module proposed in [3] for a distributed array, and it has highlighted in red the main sources of phase and amplitude errors that affect the array pattern which were considered in this study: LO phase noise, LO frequency linear drift and *I* and *Q* gain unbalance.

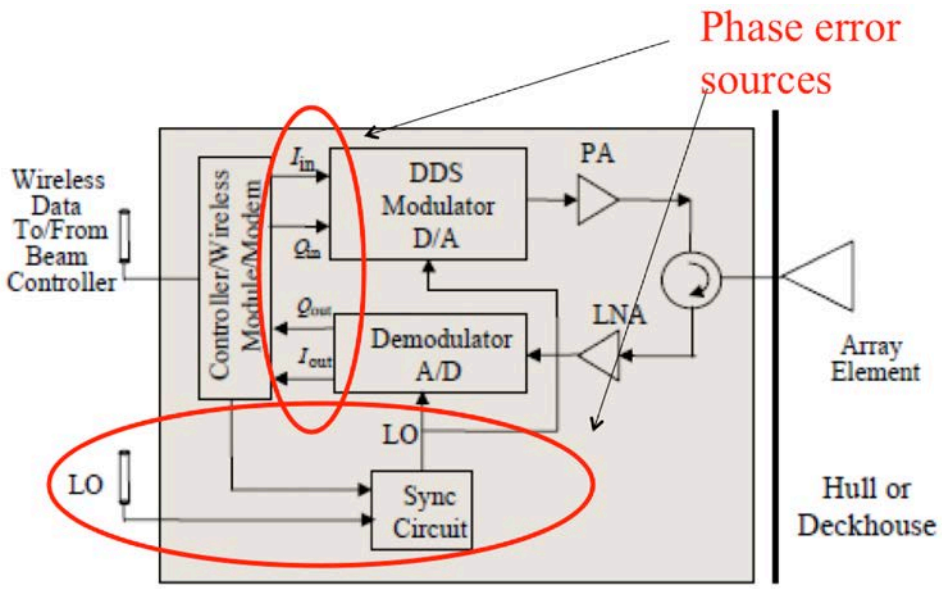

Figure 17. A T/R Module Block Diagram. Phase Error Sources are Highlighted in Red.

Adapted from [3]: D. Jenn, Y. Loke, T. C. H. Matthew, Y. E. Choon, O. C. Siang, and Y. S. Yam, "Distributed Phased Arrays and Wireless Beamforming Networks," *Int. J. Distrib. Sens. Networks*, vol. 5, no. 4, pp. 283–302, 2009. p. 284.

The LO supplies the reference signal for the modulator, demodulator and all digital components that demand a clock reference. Phase errors are generated if LOs errors are propagated into these components. A wireless LO distribution concept is shown in Figure 17; however, most applications employ a hardwired distribution circuit.

In Chapter III.A.4.b, the consequences of unbalanced gain between the *I* and *Q* branches, which adds a phase error that can degrade the array pattern characteristics, was explained. Mislocation of array elements is another source of phase error. Depending on the operating frequency, a couple of centimeters can represent more than one wavelength.

These phase errors were modeled using MATLAB, and the simulation results are presented in the following sections.

B. ARRAY FACTOR COMPLEX WEIGHTS

The array factor expressed in (3.5) has the complex weight W_n, which is set to scan the main beam, control sidelobes and also potentially compensate for phase errors [13]. In this simulation scenario, the magnitude of the complex weight is used for tapering, whereas the phase is employed for beam scanning.

Phased array antennas designed for radars typically use a Taylor taper for sidelobe level control. The main characteristics of arrays that use this taper are the monotonically decreasing sidelobes and the absence of edge discontinuities [33].

For the linear array simulations, the taper was set to obtain a maximum relative sidelobe level of -35 dB and Nbar of 5, which is the number of "nearly constant-level sidelobes adjacent to the mainlobe" [34]. For the array of subarrays simulations, for each subarray the taper was set to a maximum relative sidelobe level of -20 dB and an Nbar of 2. For beam pointing, the scan angles are given by direction cosine expressions u_s, v_s, w_s in (3.1), nulling the exponent in the scan direction.

C. PATTERN CHARACTERISTICS

The purpose of these simulations is the numerical calculation of the array pattern characteristics, i.e., gain, average and peak sidelobe levels, and pointing errors. The array

pattern formula given in (3.1) was programmed in MATLAB to simulate hardware errors in the arrays, and the results were used to extract the sidelobe information and beam pointing direction.

1. Average sidelobe level

The average SLL is computed from pattern samples from outside the mainbeam as

$$\langle SLL \rangle = \frac{1}{N-n_1} \sum_{n=-N}^{n_1} |F(n\Delta\theta,\phi)|^2 + \frac{1}{N-n_2} \sum_{n=n_2}^{N} |F(n\Delta\theta,\phi)|^2 \qquad (5.1)$$

where

$\langle SLL \rangle$ = average sidelobe level,

$F(\theta,\phi)$ = array pattern,

$\Delta\theta$ = numerical calculation step size (sampling interval) in degrees,

N_ρ = Array maximum angle, generally 90°,

n_1 = mainlobe first left null, and

n_2 = mainlobe first right null.

For this simulation ϕ is assumed to be zero, and the step size $\Delta\theta$ is 0.2 degrees. The mainlobe first nulls, left and right, were found using MATLAB function *findpeaks.m.*

2. Peak sidelobe level

In similar fashion, the peak sidelobe level relative to the mainbeam maximum is expressed by:

$$MAX(SLL) = MAX\left(|F(n\Delta\theta,\phi)|^2\right), \quad \text{for } n < n_1 \text{ and } n > n_2 \qquad (5.2)$$

where $MAX(\cdot)$ represents the maximum value of the vector.

3. Beam pointing angle

The beam pointing direction is the angle θ_{max} at which the radiation pattern has the maximum value

$$F(\theta_{max},\phi) = MAX\left(\left|F(n\Delta\theta,\phi)\right|^2\right), \quad \text{for } n_1 < n < n_2. \tag{5.3}$$

Ideally, the value for θ_{max} is equal to θ_s, the scanning angle; therefore, the difference between the θ_{max} and θ_s is the beam pointing error

$$BPE = \theta_{max} - \theta_s. \tag{5.4}$$

Under the influence of random phase noise, random *I* and *Q* gain unbalance, and element mislocation, the BPE is a random variable which has a standard deviation relative to the half-power beamwidth

$$\sigma_{BPE} = \left(\sqrt{\frac{VAR(\theta_{max} - \theta_s)}{\theta_{HPBW}}}\right) \tag{5.5}$$

where the $VAR(\cdot)$ is the variance and the θ_{HPBW} is the half-power beamwidth. In this thesis, the mean of the BPE is *not* expressed relative to θ_{HPBW} but is given by

$$\langle BPE \rangle = \langle \theta_{max} - \theta_s \rangle. \tag{5.6}$$

4. Pattern gain

The gain is calculated using (3.24), which requires the normalized antenna radiation pattern integration; therefore, the Gaussian quadrature technique was employed.

Gaussian quadrature is a numerical integration technique whose result approaches the optimum integration value [35]. It uses a weighting function and selects abscissa values to match the roots of a preselected orthogonal polynomial which depend on the integration interval. The simulation abscissas and weighting function can be found in many handbooks of mathematical functions, for example, reference [36].

D. UNIFORM ARRAY HARDWARE ERROR SIMULATIONS

1. Simulation Scenario for Phase Noise, Gain Unbalance and Frequency Drift Error

In Table 1 the simulation settings for a uniform linear array of 100 identical elements employed in the phase noise, *I* and *Q* gain unbalance and frequency linear drift simulation scenarios is summarized.

Table 1. Array Characteristics used in MATLAB Simulations

Number of elements	100
Elements spacing	0.2 wavelength
Element factor	$\cos(\theta)$
Nominal frequency	300 MHz
Tapering	Taylor (-35 dB SLL, Nbar = 5)

2. Phase Noise Simulation

a. Simulation Scenario

Non-ideal LOs are subject to phase noise, i.e., amplitude and phase fluctuations caused by internal and external factors. The phase noise characterization is detailed in Chapter IV.A.3. For simulation purposes, the phase noise was modeled as WPM converted to time-domain as random phase noise deviation φ, which is applied in the modified expression for array pattern given in (3.8). The estimation of φ is addressed in Section F.1.

This simulation scenario assumes independent LOs for all elements but assumes they are synchronized with each other. In other words, all LOs have the same frequency and phase offset, but the phase noise is present and independent for all oscillators.

b. Simulation Results

The simulation results are obtained from the average of 100 trials. The Taylor taper is set to give a maximum relative sidelobe of -35 dB. Four different scanning angles were simulated: 0^o, 15^o, 30^o and 45^o.

Shown in Figure 18 is the pattern distorted by phase deviation. The top pattern is based on a phase noise standard deviation of 0.05 rad, whereas for the bottom pattern the noise has 0.5 rad of standard deviation. The error free pattern is shown by the dotted line.

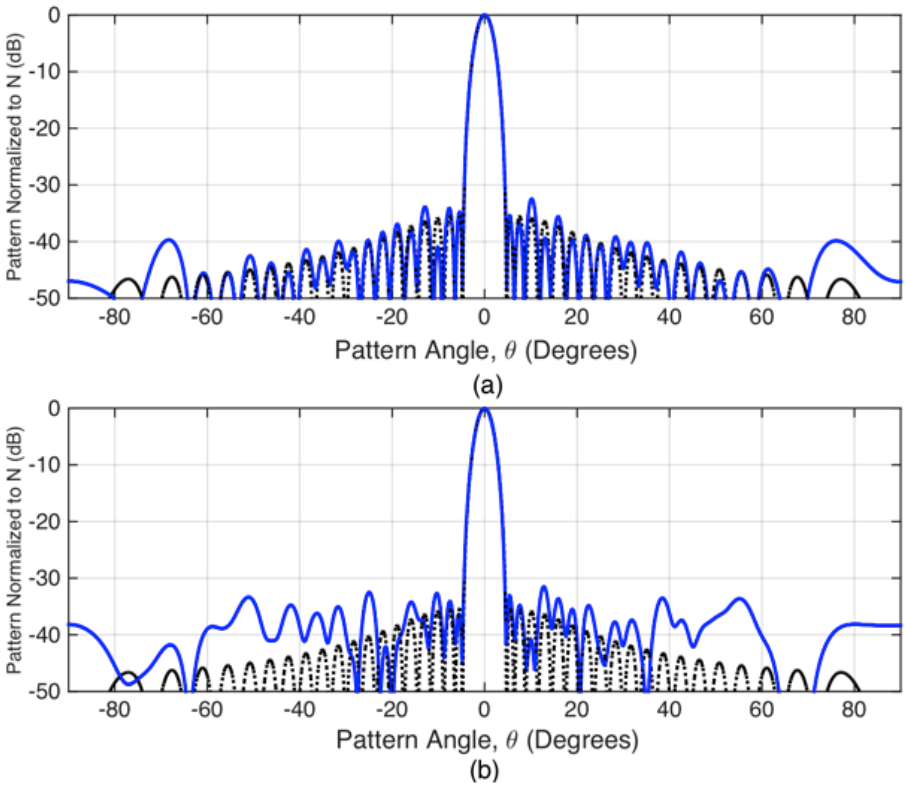

Figure 18. Linear Array Pattern Degraded by Phase Noise (solid). (a) $\varphi_{RMS} = 0.05$ rad and (b) $\varphi_{RMS} = 0.5$ rad

From Figure 18, there is a noticeable increase in sidelobes, which is confirmed by $\langle SLL \rangle$ and $MAX(SLL)$ results. The plot in Figure 19 illustrates the average sidelobe level, calculated using (5.1), as a function of phase deviation. Note that for $\varphi_{RMS} > 0.12$ rad, $\langle SLL \rangle$ is already larger than the maximum sidelobe level limited by the Taylor taper and is worse for oblique scanning angles.

In Figure 20 the peak sidelobe level, computed using (5.2), as a function of phase deviation is plotted. Note that for $\varphi_{RMS} > 0.16$ rad, the $MAX(SLL)$ is ten times larger than maximum desired sidelobe level, which is -35 dB. As expected, the mainlobe gain decreases as a consequence of the sidelobe level increase. In Figure 21 the array gain loss is illustrated as function of phase deviation. The loss is around 0.5 dB for $\varphi_{RMS} \approx 0.37$ rad.

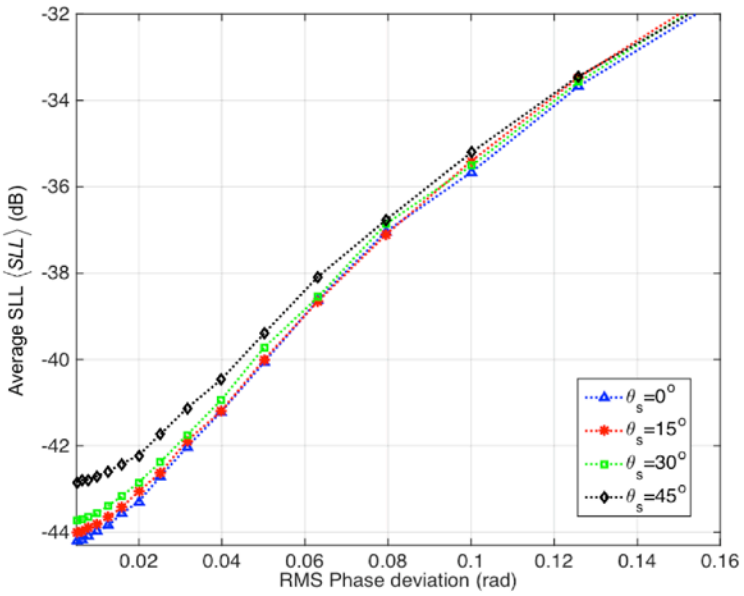

Figure 19. Relative Average Sidelobe Level $\langle SLL \rangle$ vs. Phase Noise Standard Deviation φ_{RMS} Plotted for Four Scanning Angles

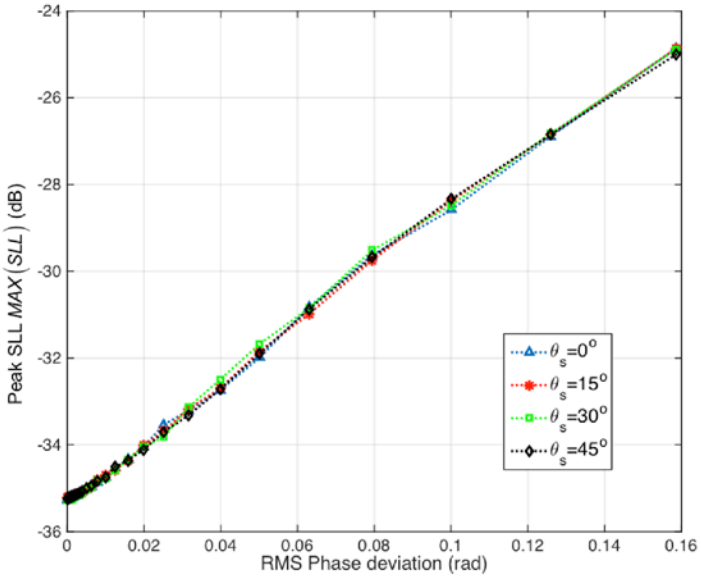

Figure 20. Relative Peak Sidelobe Level $MAX(SLL)$ vs. Phase Noise Standard Deviation φ_{RMS} Plotted for Four Scanning Angles

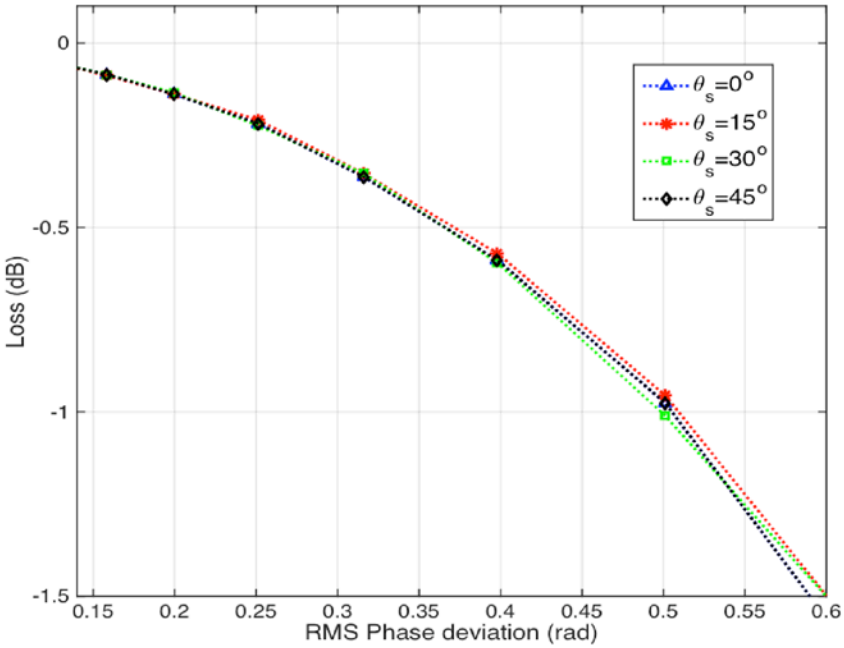

Figure 21. Array Gain Loss Due to Phase Noise Plotted for Four Different Scanning Angles

Pointing error is another concern for arrays performing tracking. In Figure 22 the average beam pointing error in degrees is illustrated, and the beam pointing error standard deviation relative to the HPBW is shown in Figure 23. Note that for the pointing error, standard deviation is larger than 5% of the HPBW, which is a significant error for high accuracy systems. Long-range applications such as satellite communications and radar are sensitive to small pointing errors that result in missing the target by several meters or kilometers. The HPBW as a function of gain unbalance is shown in Figure 24.

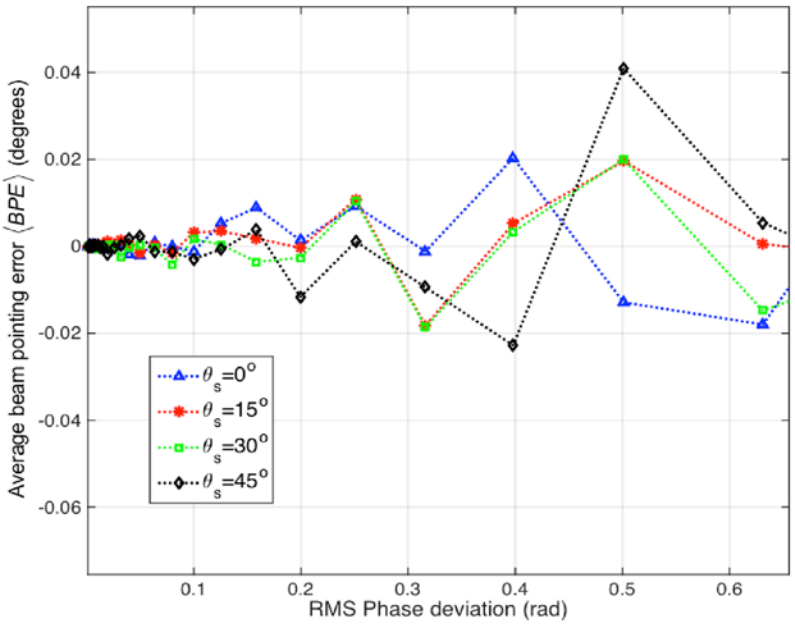

Figure 22. Average Beam Pointing Error $\langle BPE \rangle$ vs. Phase Noise Deviation φ_{RMS} Plotted for Four Different Scanning Angles

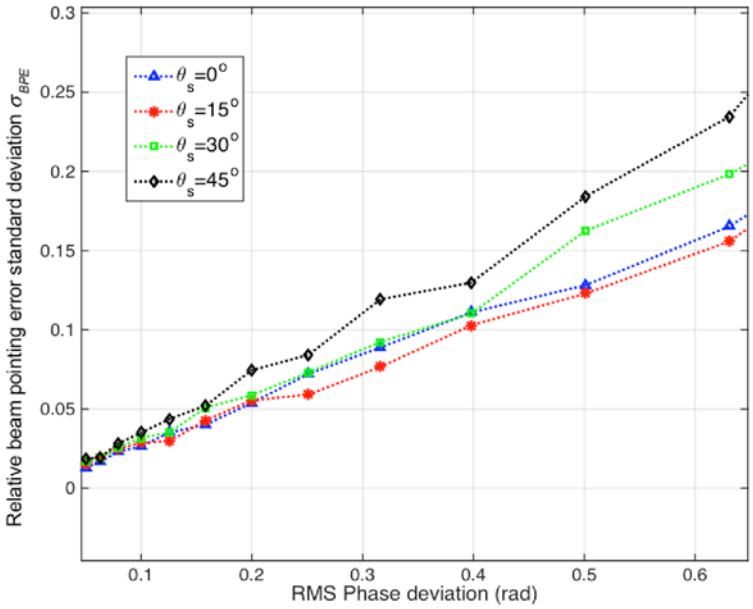

Figure 23. Relative Standard Deviation σ_{BPE} vs. Phase Noise Deviation φ_{RMS} Plotted for Four Different Scanning Angles

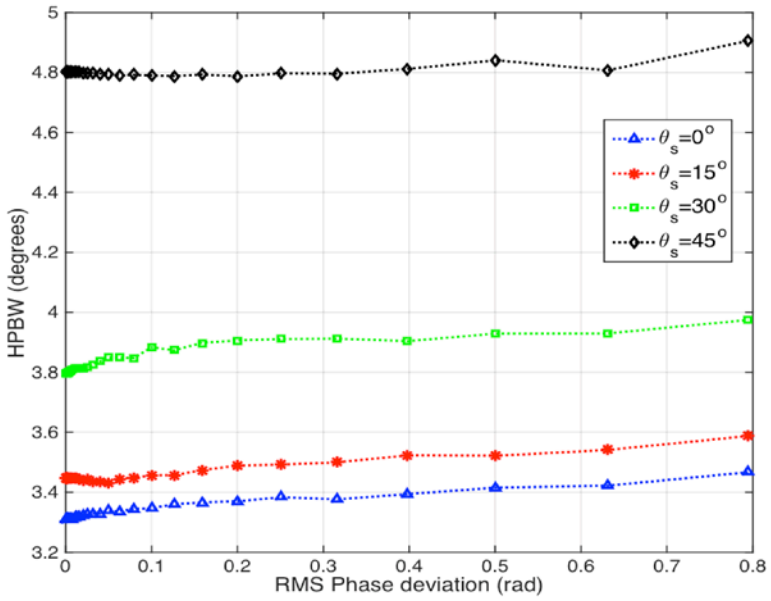

Figure 24. Half-Power Beamwidth vs. Phase Noise Deviation φ_{RMS} Plotted for Four Different Scanning Angles

3. *I* and *Q* Gain Unbalance

a. Simulation Scenario

This simulation scenario reproduces the effects of non-ideal quadrature modulators and demodulators which are used in radar and communications systems for phase control. In Figure 25 a model of the simulation scenario is illustrated. Here, each element is supposed to have a random attenuator for *I* and *Q* branches, L_I and L_Q. These attenuators represent the gain unbalance, and their values are normally distributed. This random variable probability density function (PDF) is modeled as

$$PDF = \frac{1}{\sqrt{2\pi}\sigma_L}\exp\left(-\frac{L^2}{2\sigma_L{}^2}\right) \tag{5.7}$$

where

L = random attenuator loss (either L_I and L_Q),

σ_L = random attenuator standard deviation,

= $\delta/2.575$, and

δ = nominal I and Q gain unbalance.

Using the expression above for σ_L, we expect that the random attenuation will be within the nominal gain unbalance values with 99% confidence. The modified expression for the array factor, neglecting the other phase error sources, is

$$\begin{aligned} AF(\theta,\phi) &= \sum_{n=1}^{N}\left[(1+\delta_n)e^{j\epsilon_n}A_n e^{j\psi}\right]e^{j\vec{k}\bullet\vec{r}_{on}} \\ &= \sum_{n=1}^{N}\left[W_n\right]e^{j\vec{k}\bullet\vec{r}_{on}} \\ &= \sum_{n=1}^{N}\left[I(L_I)+jQ(L_Q)\right]e^{j\vec{k}\bullet\vec{r}_{on}} \end{aligned} \tag{5.8}$$

where

$I(L_I)$ = in-phase signal distorted by random attenuation L_I, and

$Q(L_Q)$ = quadrature signal distorted by random attenuator L_Q.

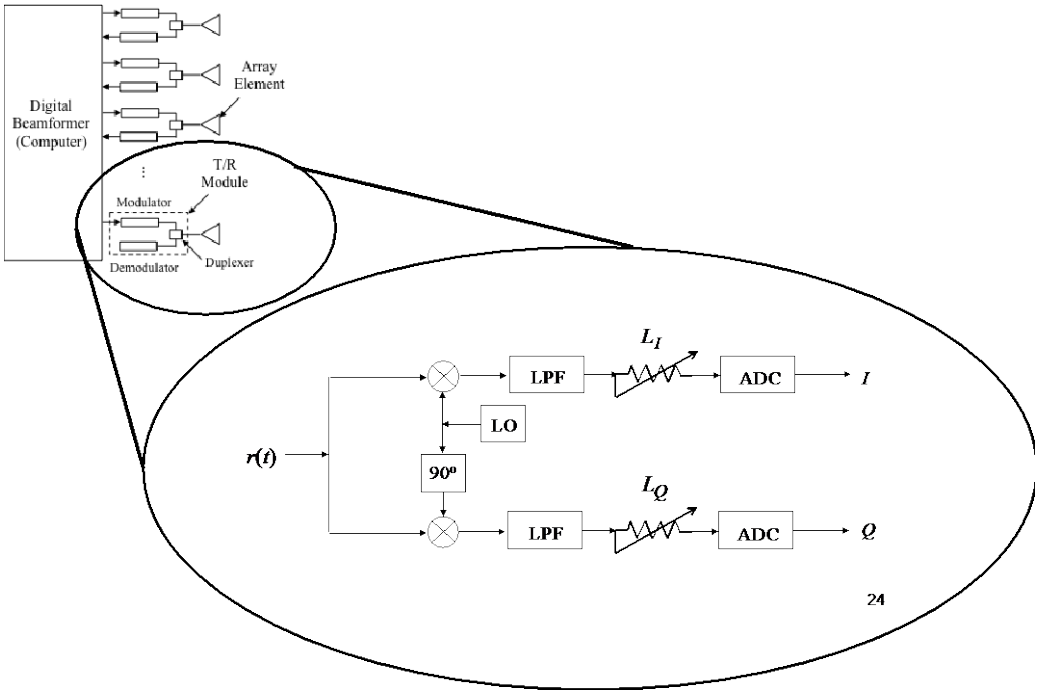

Figure 25. Receiving Simulation Scenario where L_I and L_Q are Hypothetical Random Attenuators

b. Simulation Results

Similar to previous cases, the simulation results were obtained from the average of 100 trials for four different scanning angles: 0^o, 15^o, 30^o and 45^o.

The pattern distorted by I and Q gain unbalance is shown in Figure 26. On the top pattern, the elements have random magnitude attenuation within the limit of 0.4 dB, whereas for the bottom pattern the limit was 1.0 dB. The dotted line is the pattern with no errors. In Figure 27 and Figure 28 the average sidelobe level and the peak sidelobe level, respectively, are illustrated. The impact of *I* and *Q* gain unbalance is less significant than the phase noise; however, for $L > 1$ dB this error contribution is more noticeable. A $L > 1$ dB is unlikely to happen because modulators and demodulators are designed to have a very small gain unbalance. The modulator used in the example in Section F, the ADL5375 from Analog Devices [37], specifies an *I* and *Q* gain unbalance is only 0.08 dB.

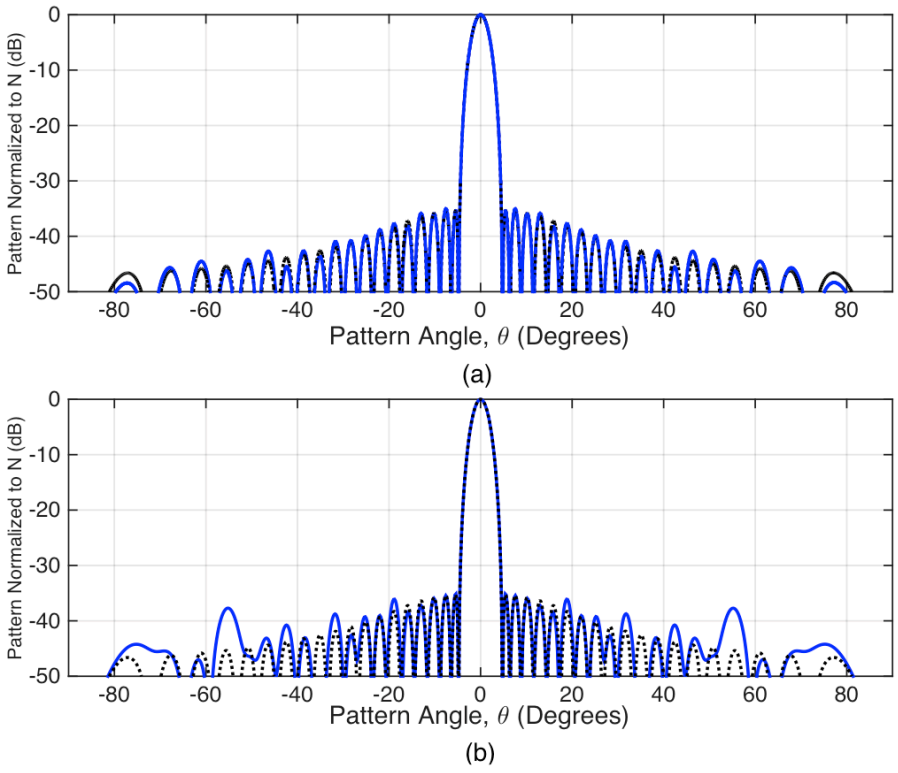

Figure 26. Linear Array Pattern Degraded by *I* and *Q* Gain Unbalance (Solid). (a) *L* = 0.4 dB and (b) *L* = 1.0 dB

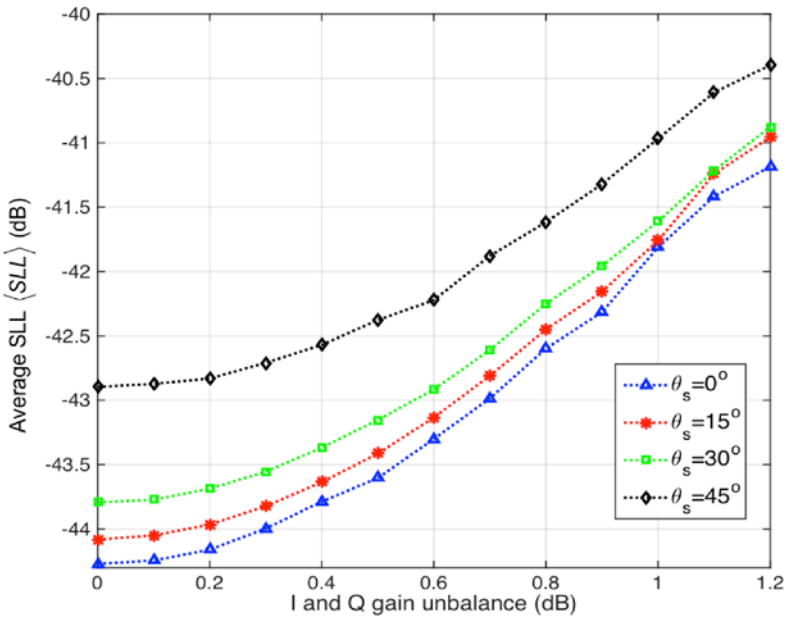

Figure 27. Relative Average Sidelobe Level $\langle SLL \rangle$ vs. *I* and *Q* Gain Unbalance *L* Plotted for Four Scanning Angles

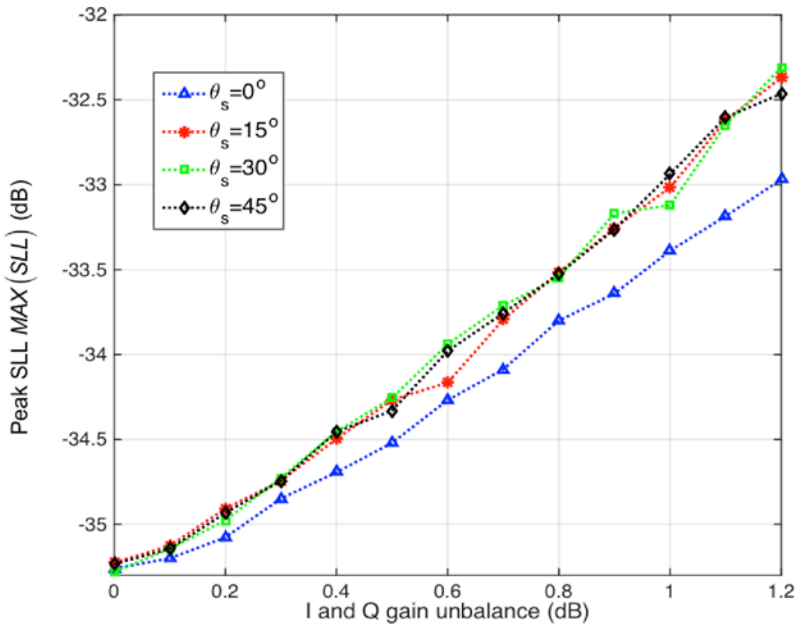

Figure 28. Relative Peak Sidelobe Level vs. *I* and *Q* Gain Unbalance *L* Plotted for Four Scanning Angles

When compared to phase noise simulations in the previous section, the loss due to *I* and *Q* gain unbalance is small. The plot in Figure 29 shows an average loss of 0.002 dB when the gain unbalance is greater than 0.5 dB.

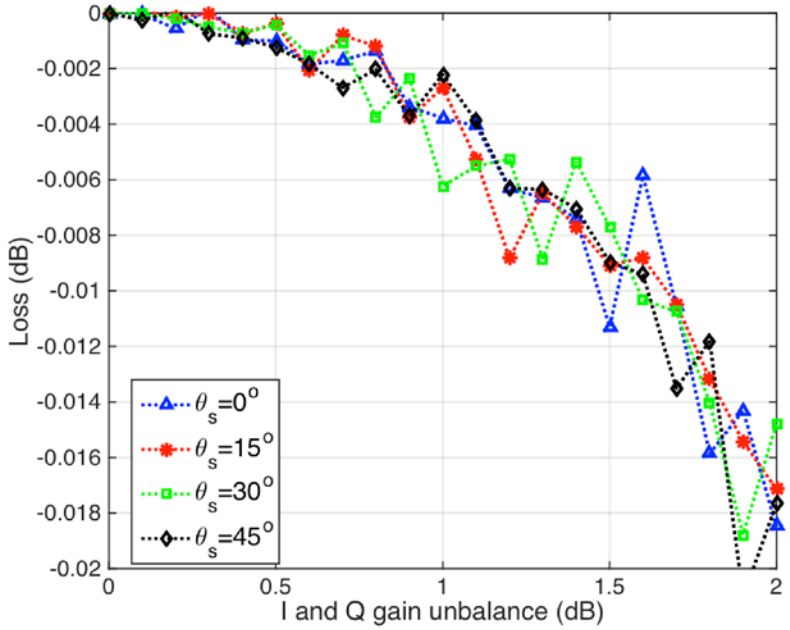

Figure 29. Array Gain Loss Due to *I* and *Q* Gain Unbalance *L* Plotted for Four Scanning Angles

Beam pointing accuracy is more affected by this type of error than the random phase deviation. The average beam pointing error is shown in Figure 30, and the beam pointing standard deviation relative to the HPBW is shown in Figure 31. From the $\langle BPE \rangle$ plot one can see that the pointing error is more significant when the gain unbalance is higher. The pointing error standard deviation reaches 12% with 0.5 dB of gain unbalance. The HPBW as a function of gain unbalance is shown in Figure 32.

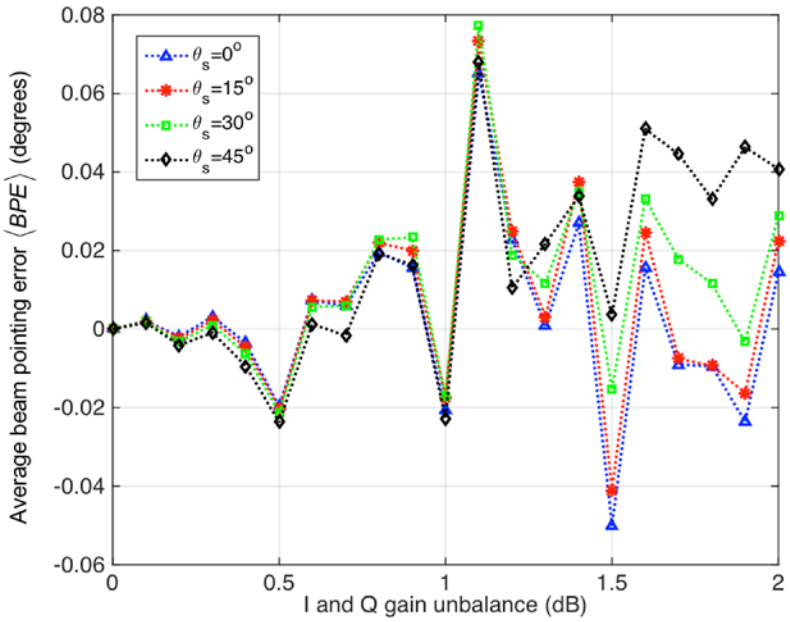

Figure 30. Relative Average Beam Pointing Error $\langle BPE \rangle$ vs. *I* and *Q* Gain Unbalance *L* Plotted for Four Scanning Angles

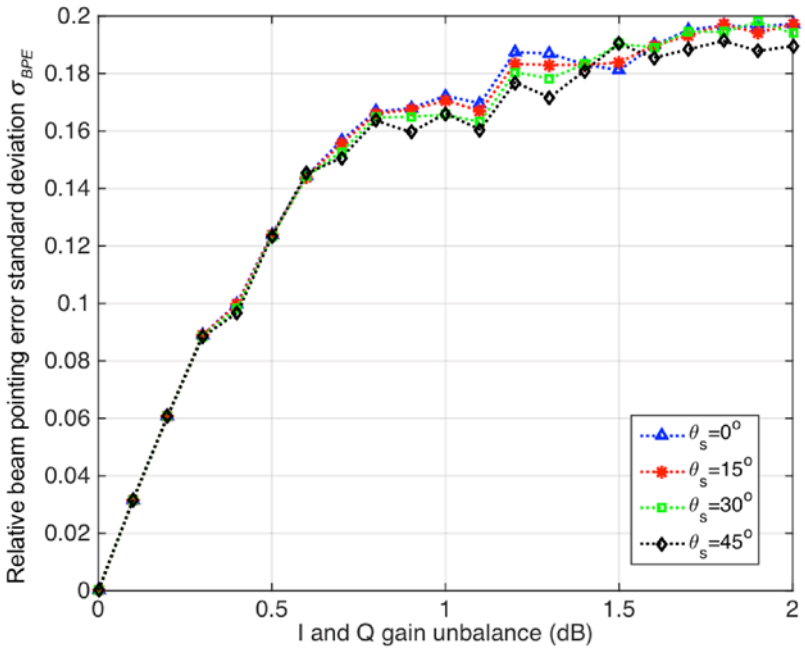

Figure 31. Relative Standard Deviation σ_{BPE} vs. *I* and *Q* Gain Unbalance *L* Plotted for Four Scanning Angles

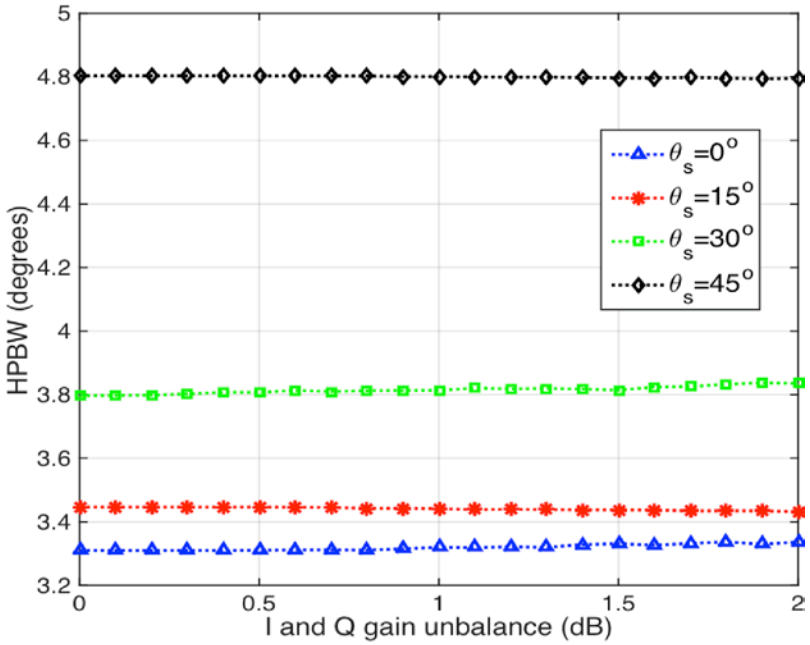

Figure 32. Half-Power Beamwidth vs. *I* and *Q* Gain Unbalance *L* Plotted for Four Scanning Angles

4. Linear Frequency Drift

a. Simulation Scenario

For linear frequency drift, it is assumed that all elements have an independent LO. If no other phase errors are considered, the instantaneous frequency (4.1) becomes

$$\begin{aligned} f(t) &= f_s + f_d(t) + f_a(t) \\ &= f_n + f_d(t) \end{aligned} \tag{5.9}$$

with $f_{offset} = 0$ and $f_a(t) = 0$.

For this simulation, the elements are assumed to have independent LOs with instantaneous frequency normally distributed in a random process, with PDF

$$PDF_{freq} = \frac{1}{\sqrt{2\pi}\sigma_d} \exp\left(-\frac{(f - f_n)^2}{2\sigma_d^2} \right) \tag{5.10}$$

where

f = instantaneous frequency $f(t)$,

f_n = nominal frequency, and

σ_d = frequency drift standard deviation

= $2\pi Dt^2/2.575$.

Recall that $f_d = 2\pi Dt^2$.

Using this definition for σ_d leads to a $f_d(t)$ contribution within the desired oscillator accuracy with 99% confidence. Furthermore, when $t = 0$, all the elements are phase synchronized to the nominal frequency $f(t) = f_n$. The expression for the array factor accounting only for frequency drift is given by

$$AF(\theta,\phi) = \sum_{n=1}^{N} W_n e^{j\vec{k}\bullet\vec{r}_{on}} \tag{5.11}$$

where

$$\begin{aligned} \vec{k}\bullet\vec{r}_{on} &= k[ux_n + vy_n + wz_n] \\ &= \left(2\pi f(t)/c\right)[ux_n + vy_n + wz_n] \\ &= \left(2\pi[f_n + f_d]/c\right)[ux_n + vy_n + wz_n]. \end{aligned}$$

Expanding the expression (5.11), we get

$$\begin{aligned} AF(\theta,\phi) &= \sum_{n=1}^{N} W_n e^{jk[ux_n+vy_n+wz_n]} \\ &= \sum_{n=1}^{N} W_n e^{j\vec{k}_n\bullet\vec{r}_{on}} \left(e^{j\left[2\pi f_d(t)/c\right][ux_n+vy_n+wz_n]} \right) \end{aligned} \tag{5.12}$$

where $k_n = 2\pi f_n/c$. For a linear array along the *x*-axis (5.12) reduces to

$$AF(\theta,\phi) = \sum_{n=1}^{N} W_n e^{j\vec{k}_n \bullet \vec{r}_{on}} \exp\left(j\frac{2\pi f_d(t) u x_n}{c} \right) \tag{5.13}$$

where the expression in parenthesis is the phase error due to frequency drift. Notice the expressions (5.12) and (5.13) are actually functions of time because the linear drift is time dependent. An important observation is that drift contribution to phase error is not a random process. In other words, independent of what type of oscillator is being used, if they are set in free-run or hold-over mode, the phase error magnitude linearly increases.

b. Simulation Results

Different from the previous scenarios, for frequency drift the pattern degradation is illustrated as a function of time. The importance of a stable local oscillator distribution system to continuously synchronize the system is respectively illustrated in this section.

In Figure 33 and Figure 34 the gain loss and average sidelobe level, respectively, as a function of time without synchronization of elements whose LO are in a free-run mode are shown. Notice the best clock, with 0.1 ppm accuracy, tolerates a longer non-synchronization interval, around 0.1 s. For example, it is necessary to employ a LO with 10^{-13} accuracy if an array requires a synchronized period of 24 hours without external reference. The cesium frequency standard Microsemi 5071A has 10^{-12} accuracy [38]; moreover, the synchronization requirement is more demanding and critical for higher frequencies.

In Figure 35 an array pattern simulation assuming an array employing local oscillators with accuracy of 0.1 ppm or better, in free-run mode, and a nominal frequency of 300 MHz is shown. An array using a LO with an accuracy of 100 ppm was simulated, and the results are illustrated in Figure 36. This scenario is more realistic because 100 ppm is approximately the accuracy of available COTS VCO's. In this case the pattern is severely degraded after 2.0 ms, meaning that the synchronization interval should not be longer than a fraction of millisecond.

The conclusion extracted from the Figure 35 and Figure 36 pattern plots is the necessity of periodic phase synchronization in order to avoid pattern degradation due to frequency drift errors.

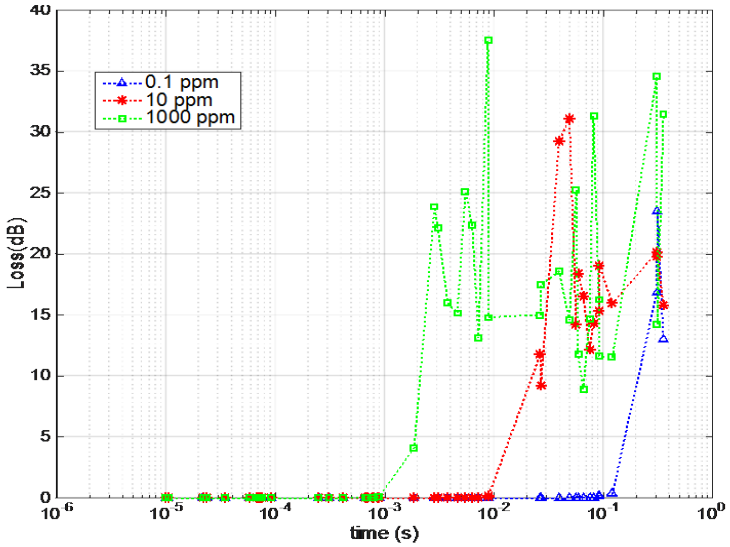

Figure 33. Gain Loss Due to LO in Free-Run as a Function of Time. Different Colors Represent Different LO Accuracies, Operating at 300 MHz.

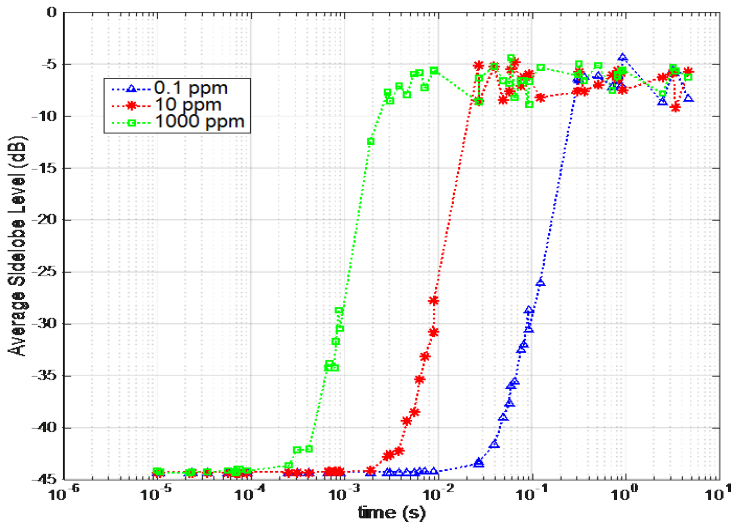

Figure 34. Average Sidelobe Level Due to LO in Free-Run as a Function of Time. Different Colors Represent Different LO Accuracies, Operating at 300 MHz.

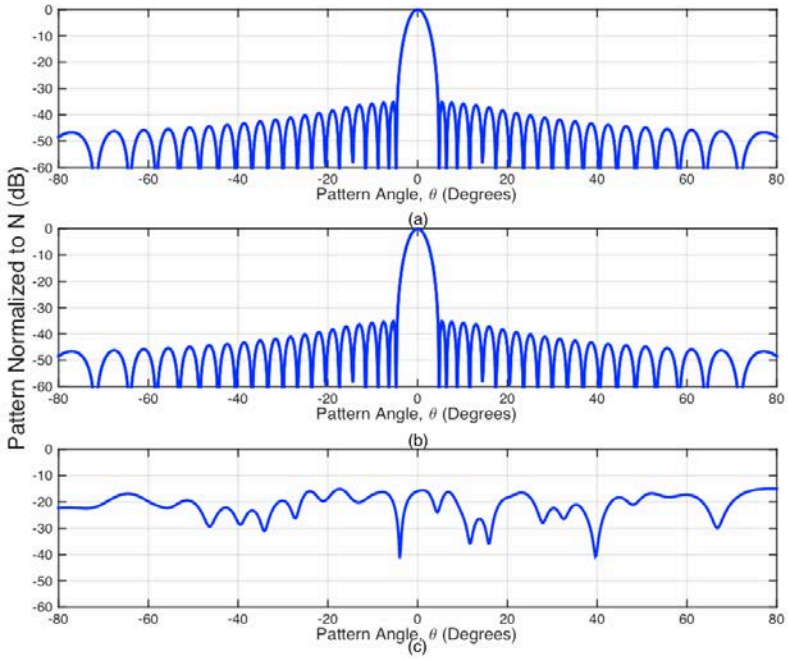

Figure 35. Pattern Degradation Due to LO in Free-Run. LO Accuracies of 0.1 ppm or Better (a) t = 1.8 μs (b) t = 1.9 ms and (c) t = 920 ms

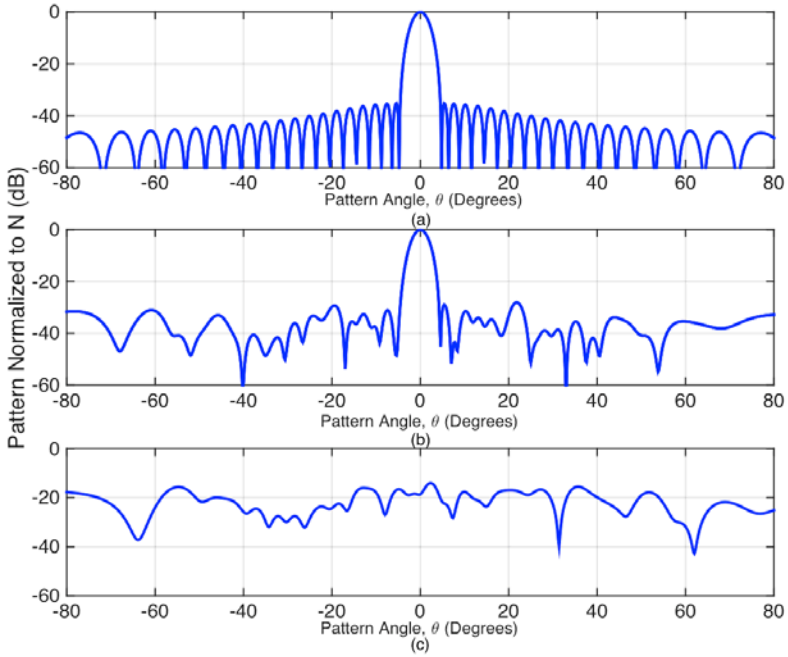

Figure 36. Pattern Degradation Due to LO in Free-Run. LO Accuracies of 100 ppm or Better (a) t = 1.8 μs (b) t = 1.9 ms and (c) t = 920 ms

5. Element Mislocation Error

a. Simulation Scenario

In Table 2, the simulation settings for a uniform linear array of 50 identical elements employed in the element dislocation error scenario, which has a different number and spacing of elements compared to previous simulations, thereby allowing a larger variation in element mislocation, is summarized.

Table 2. Array Characteristics used in MATLAB Simulations

Number of elements	50
Elements spacing	0.4 wavelength
Element factor	$\cos(\theta)$
Nominal frequency	300 MHz
Tapering	Taylor (-35 dB SLL, Nbar = 5)

In this scenario, a single LO is distributed to the array elements in a series fed manner from one edge of the array. The elements are randomly mislocated within a range so that two adjacent elements do not overlap. An example is illustrated in Figure 37. With a series feed the LO distribution errors accumulate.

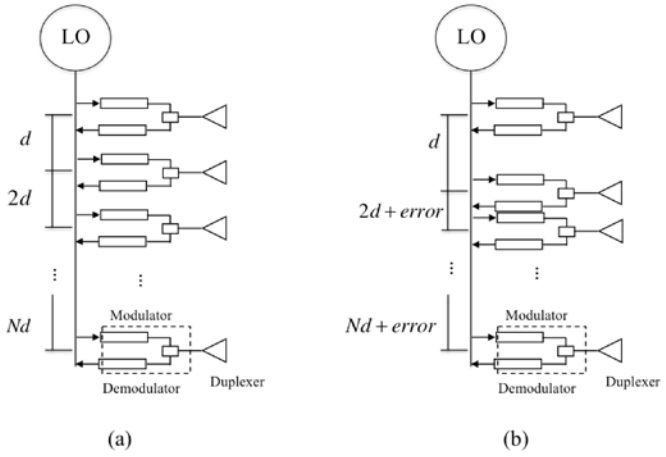

Figure 37. (a) Ideal Linear Array. (b) Linear Array with Elements non-Uniformly Distributed

In an ideal scenario, when using a common LO, the elements can compensate for the delay between element locations by applying a correction phase for the scanning direction; hence, for this scenario the complex weight is set to phase compensate based on the elements' theoretical positions. Suppose the element position is only perturbed in the *x* direction so $y_n = z_n = 0$; hence, (3.20) can be written as

$$\vec{r}_n = \vec{r}_{on} + \Delta\vec{r}_n = (x_n + \Delta x_n)\hat{x}. \tag{5.14}$$

The correction phase in the scanning direction is

$$\psi_n = \frac{2\pi x_{on}\sin(\theta_s)}{\lambda}. \tag{5.15}$$

The distance between the ideal position and the real position represents a phase error that is expressed as

$$\vec{k} \bullet \Delta\vec{r}_n = 2\pi P_\epsilon \sin(\theta) \tag{5.16}$$

where P_ϵ is the position error and is defined as $P_\epsilon = \Delta x_n / \lambda$, which is expressed in fractions of wavelengths. The variable P_ϵ is a uniform random variable with probability density function

$$PDF = \begin{cases} \dfrac{1}{MAX(P_\epsilon) - MIN(P_\epsilon)}, & MIN(P_\epsilon) < P_\epsilon < MAX(P_\epsilon) \\ 0, & \text{otherwise} \end{cases}. \tag{5.17}$$

The mislocation of elements changes the array factor, which is expressed as

$$AF(\theta,\phi) = \sum_{n=1}^{N} W_n e^{j\vec{k}\bullet\vec{r}_{on}} e^{j\vec{k}\bullet\Delta\vec{r}_n} = \sum_{n=1}^{N} \left(e^{j2\pi\sin(\theta)P_\epsilon} \right) W_n e^{j\vec{k}\bullet\vec{r}_{on}} \tag{5.18}$$

where the expression in parentheses accounts for the phase error due to element mislocation.

b. Simulation Results

In Figure 38 we see the pattern disrupted by the random mislocation of the elements and additional phase noise. On the top plot the phase noise standard deviation is 0.006 wavelengths, whereas the standard deviation for the bottom plot is 0.058 wavelengths.

From Figure 39 and Figure 40, we see there is significant increase in average and peak sidelobes. For RMS position error $P_\epsilon > 0.03\lambda$, the $\langle SLL \rangle$ is already larger than the maximum sidelobe level limited by Taylor's taper. When $P_\epsilon > 0.04\lambda$, the peak SLL is at least 10 dB higher than the no error scenario and is worse for oblique scanning angles. In Figure 41 the array gain loss due to element mislocation is shown. As expected the increase in SLL increases the gain loss; however, the array was set to make the phase correction in scanning direction, which reduces the loss effect.

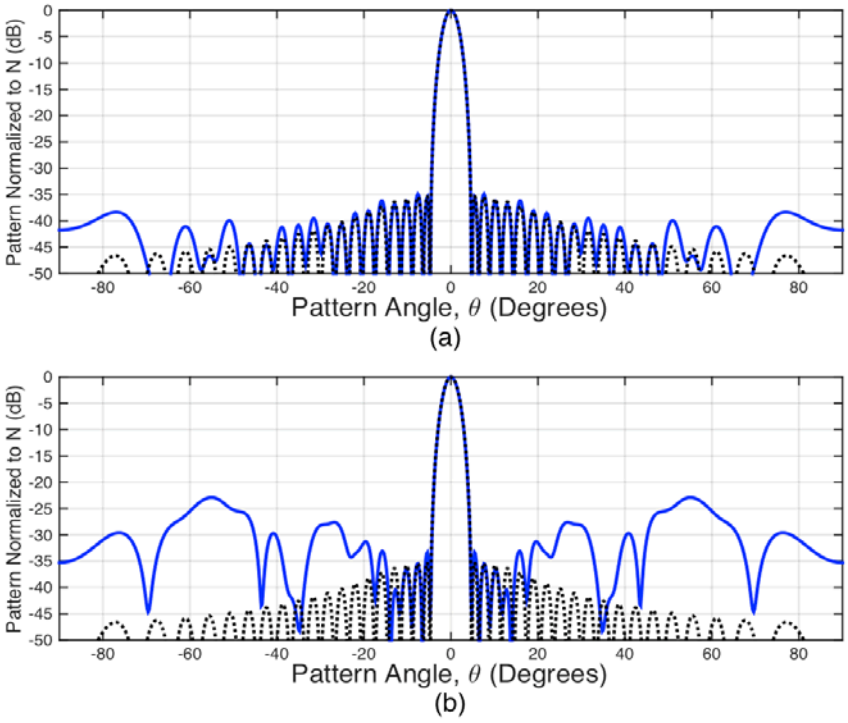

Figure 38. Linear Array Aattern Degraded by Element Mislocation (a) RMS Mislocation Error 0.006 Wavelength and (b) RMS Mislocation Error 0.058 Wavelength

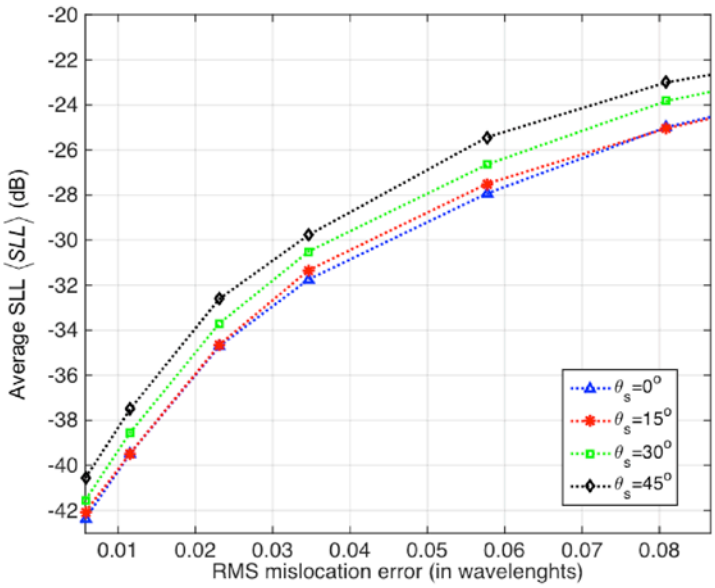

Figure 39. Relative Average Sidelobe $\langle SLL \rangle$ vs. RMS Element Mislocation (P_ϵ) Expressed in Fraction of Wavelength Plotted for Four Different Scanning Angles

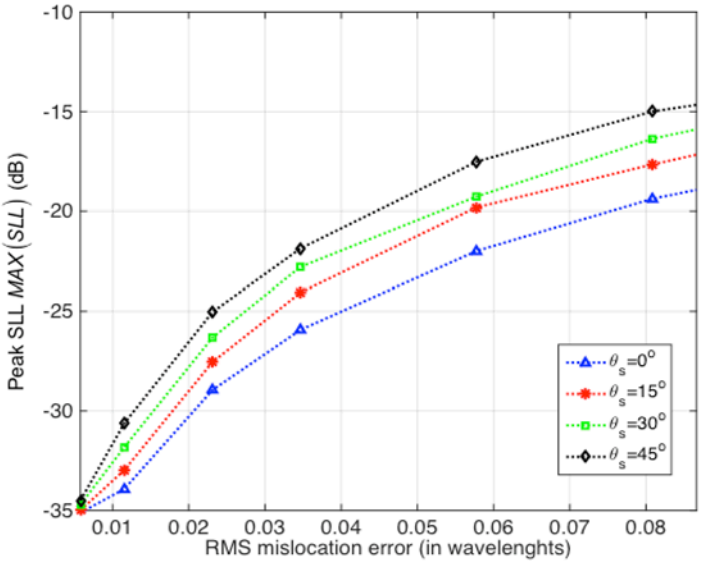

Figure 40. Relative Peak Sidelobe vs. RMS Element Mislocation (P_ϵ) Expressed in Fraction of Wavelength Plotted for Four Different Scanning Angles

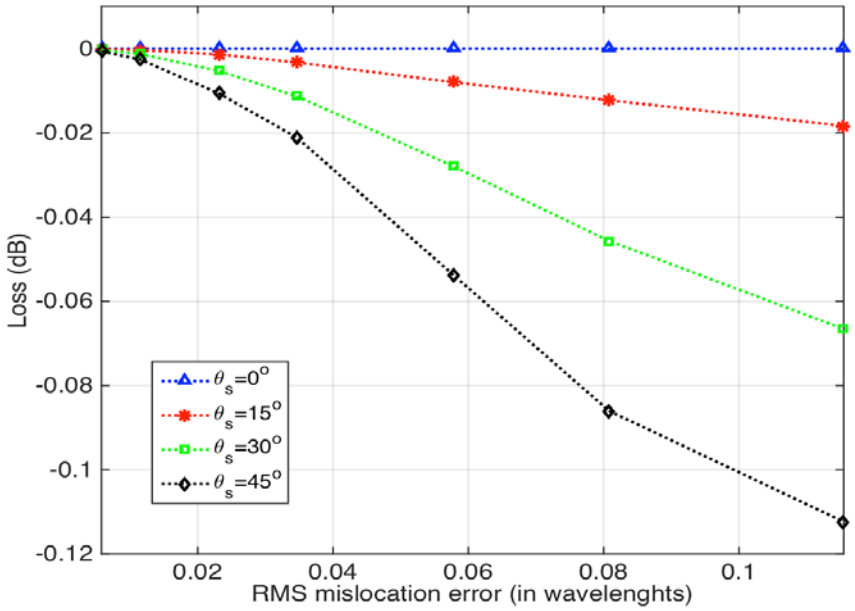

Figure 41. Array Gain Loss Due and RMS Element Mislocation (P_ϵ) Plotted for Four Scanning Angles

In Figure 42 and Figure 43 the beam pointing error average and standard deviation, respectively, are shown. The latter is relative to the half-power beamwidth. The beam pointing error in both plots increases significantly with position error. For example, the σ_{BPE} increased seven times when the P_ϵ changed from 0.1 to 0.2 λ for $\theta_s = 45^\circ$. The half-power beamwidth is shown in Figure 44 and does not show any significant change due to positioning error.

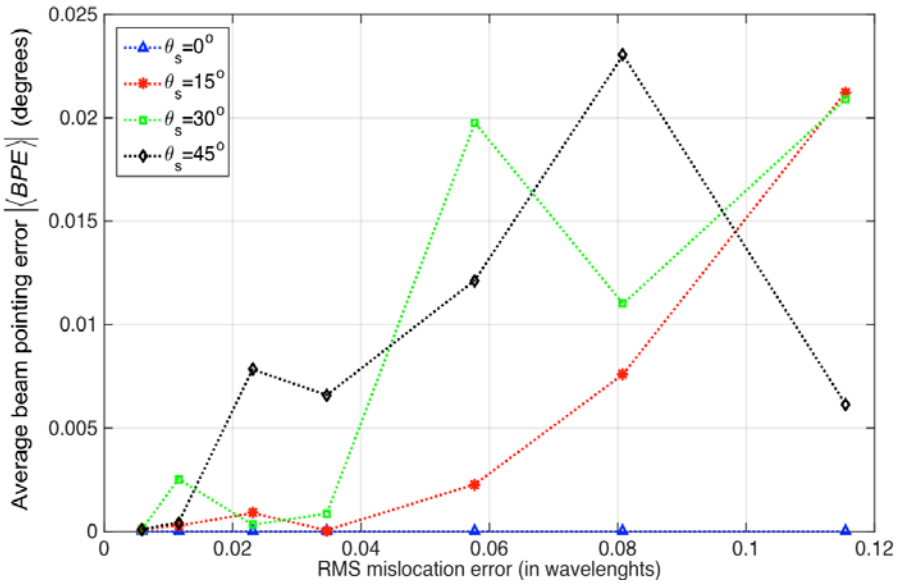

Figure 42. Magnitude of Average Beam Pointing Error $\langle BPE \rangle$ vs. RMS Element Mislocation (P_ϵ) Plotted for Four Different Scanning Angles

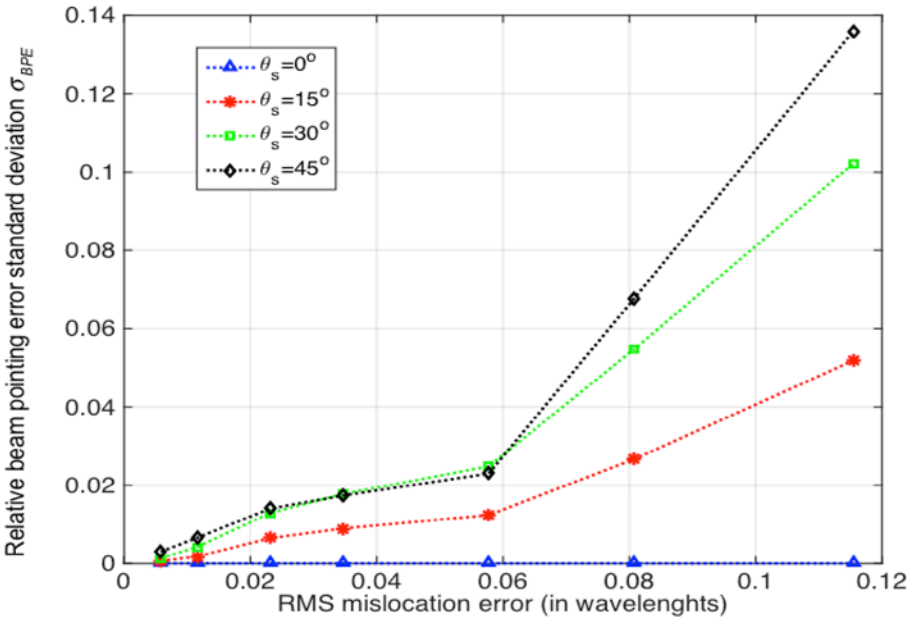

Figure 43. Relative Standard Deviation Beam Pointing Error σ_{BPE} vs. RMS Element Mislocation (P_ϵ) Plotted for Four Different Scanning Angles

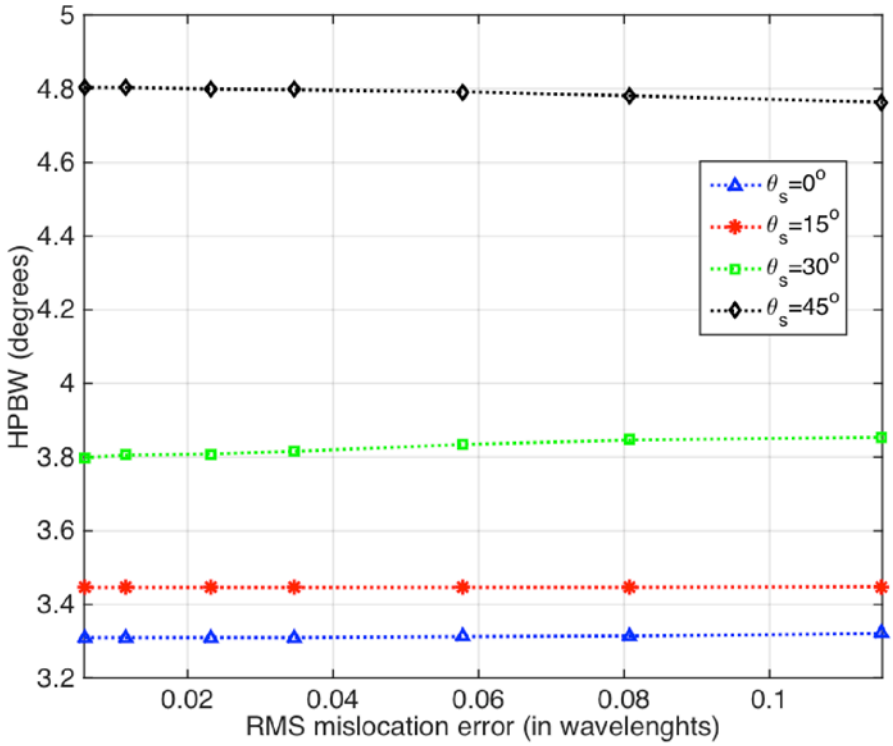

Figure 44. Half-Power Beamwidth vs. RMS Element Mislocation (P_ϵ) Plotted for Four Different Scanning Angles

E. ARRAY OF SUBARRAYS HARDWARE ERROR SIMULATIONS

1. Simulation Scenario for Phase Noise, Gain Unbalance and Frequency Drift Error

In this scenario the pattern degradation due to phase error for an array of linear subarrays with ten identical elements per subarray was simulated. The subarrays are randomly mislocated within four and five wavelengths; hence, there is no subarray overlap. In Table 3 and Table 4, the array characteristics are summarized.

Table 3. Array of Subarrays Characteristics used in MATLAB Simulations

Number of subarrays	20
Subarray spacing	4 – 5 wavelengths (uniform random distributed)
Tapering	None

Table 4. Subarray Characteristics used in MATLAB Simulations

Number of elements	10
Elements spacing	0.4 wavelength
Element factor	$\cos(\theta)$
Nominal frequency	300 MHz
Subarray tapering	Taylor (-20 dB SLL, Nbar = 2)

2. Phase Noise Simulation Results

The same simulation setting used for the linear array was repeated for an array of subarrays; i.e., each element has independent LOs which are synchronized. The subarray pattern with added phase noise deviation φ is given in (3.8), whereas the overall array pattern was computed using (3.6).

The simulation results are obtained from the average of 100 trials for four different scanning angles: 0^o, 15^o, 30^o and 45^o.

In Figure 45(a) the pattern distorted by phase noise with RMS of 0.05 rad is shown, and in the bottom plot, Figure 45(b), the phase noise RMS value is 0.5 rad. When compared to the dotted line, which is the pattern without noise errors, the plot in Figure 45(a) is almost indistinguishable, whereas for the plot in Figure 45(b), the increase in sidelobe level is noticeable. This is confirmed by the relative average and peak sidelobes plots in Figure 46 and Figure 47. Note the sidelobes for array of subarrays are usually higher than a linear array because of the grating lobes caused by the subarray spacing.

In Figure 48 the gain loss due to random phase deviation is illustrated. For phase noise with RMS of one radian (a very large value), the gain loss is approximately 3 dB. Overall, the values for gain loss are similar to those obtained in the linear array simulation.

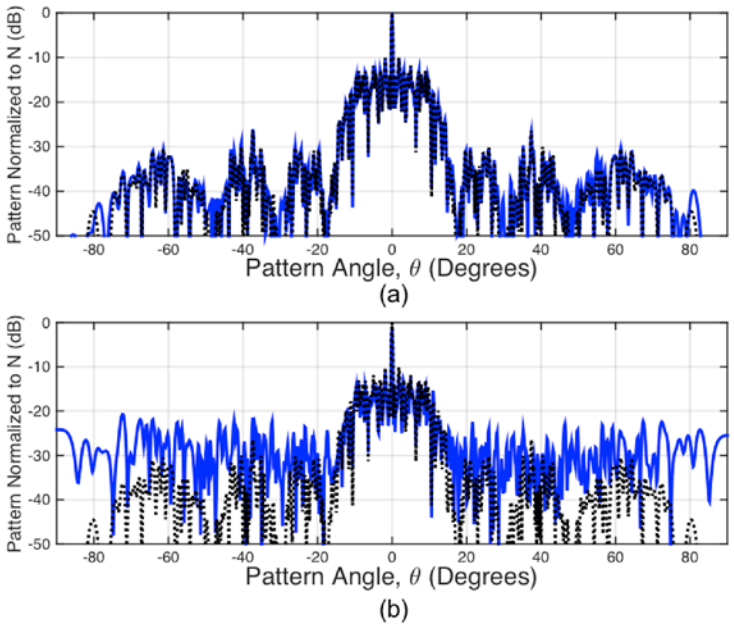

Figure 45. Linear Array of Subarrays Pattern Degraded by Phase Noise (blue), the Dotted Line is the Array Without Phase Noise Error (a) $\varphi_{RMS} = 0.05$ rad and (b) $\varphi_{RMS} = 0.5$ rad

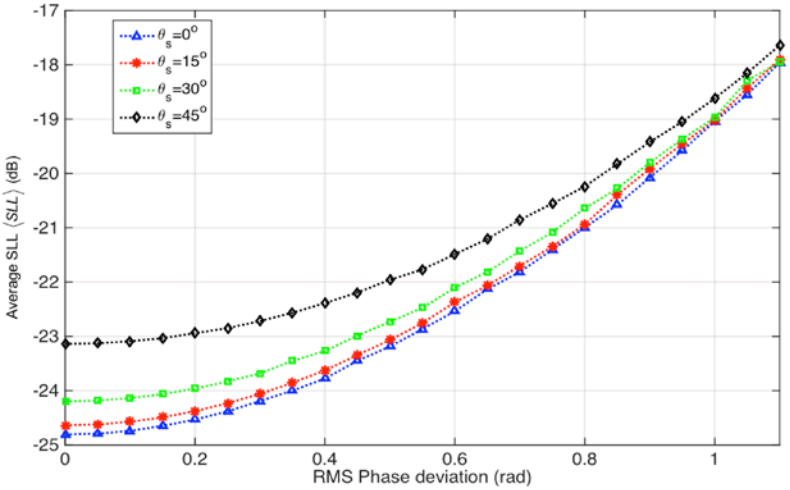

Figure 46. Relative Average Sidelobe $\langle SLL \rangle$ vs. RMS Phase Deviation φ_{RMS}

Plotted for Four Different Scanning Angles

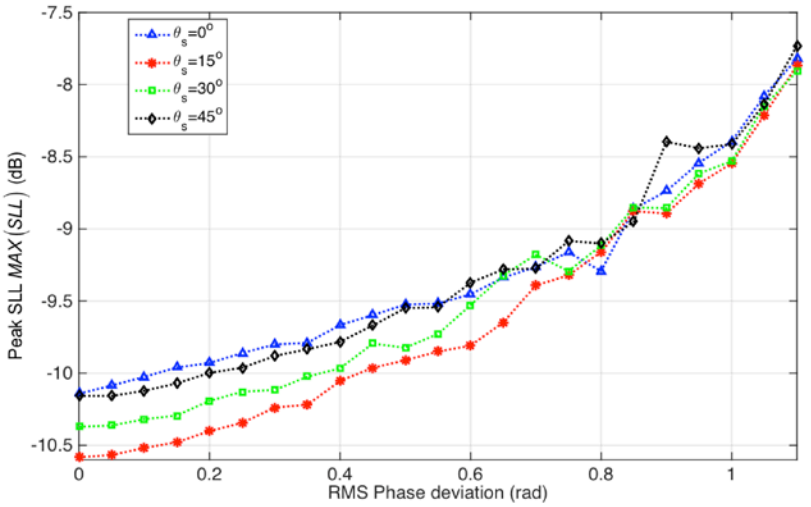

Figure 47. Relative Peak Sidelobe Level vs. RMS Phase Deviation φ_{RMS} Plotted for Four Different Scanning Angles

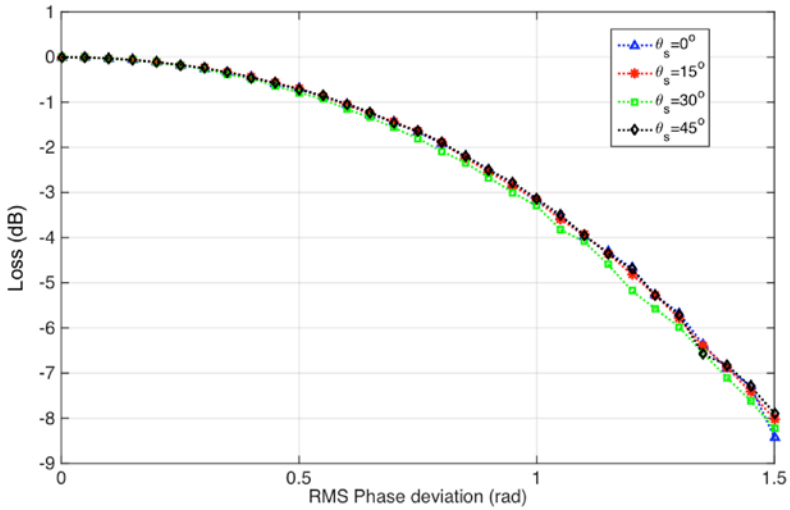

Figure 48. Array Gain vs. RMS Phase Deviation φ_{RMS} Plotted for Four Scanning Angles

In Figure 49 the average beam pointing error is illustrated and shows a small variation, on the order of couple of millidegrees, caused by phase noise. Additionally, in Figure 50 the relative beam pointing error standard deviation, which is small compared to

the result illustrated in Figure 23 for a uniform array, is shown. In the current simulation, the half-power beamwidth is smaller because the scenario used a larger array and more elements.

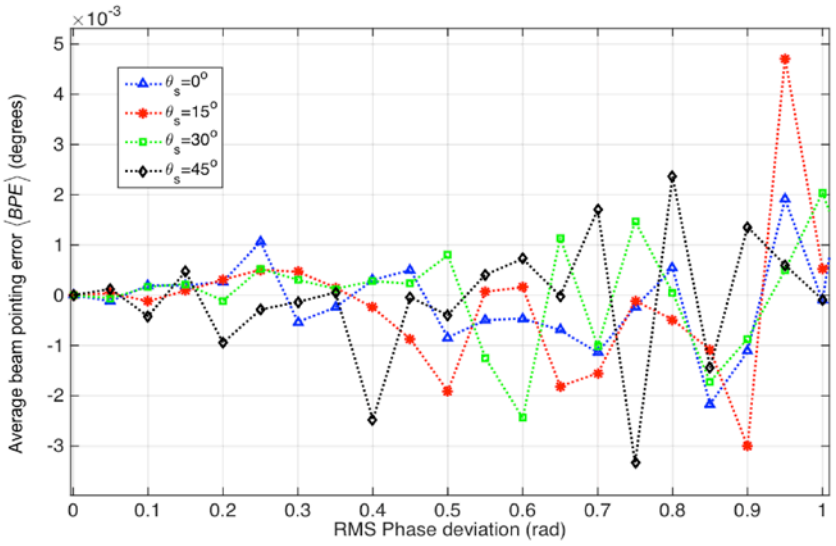

Figure 49. Average Beam Pointing Error $\langle BPE \rangle$ vs. RMS Phase Deviation φ_{RMS} Plotted for Four Different Scanning Angles

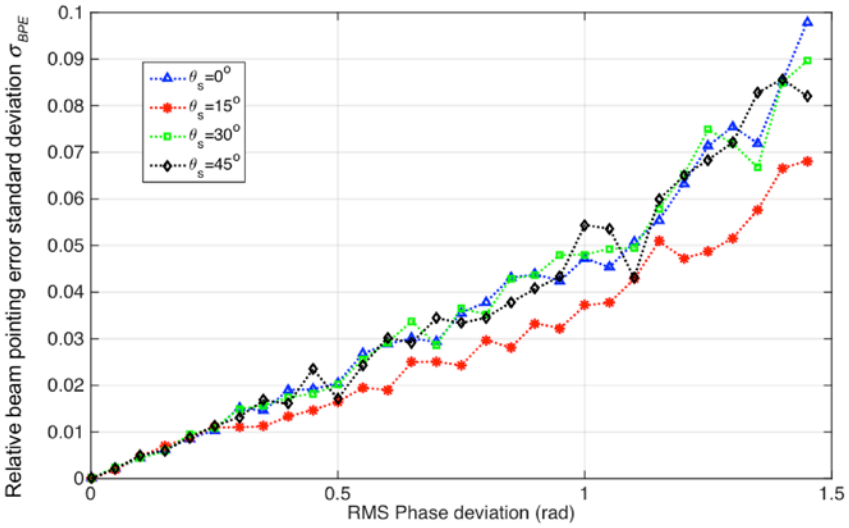

Figure 50. Relative Standard Deviation Beam Pointing Error σ_{BPE} vs. RMS Phase Deviation φ_{RMS} Plotted for Four Different Scanning Angles

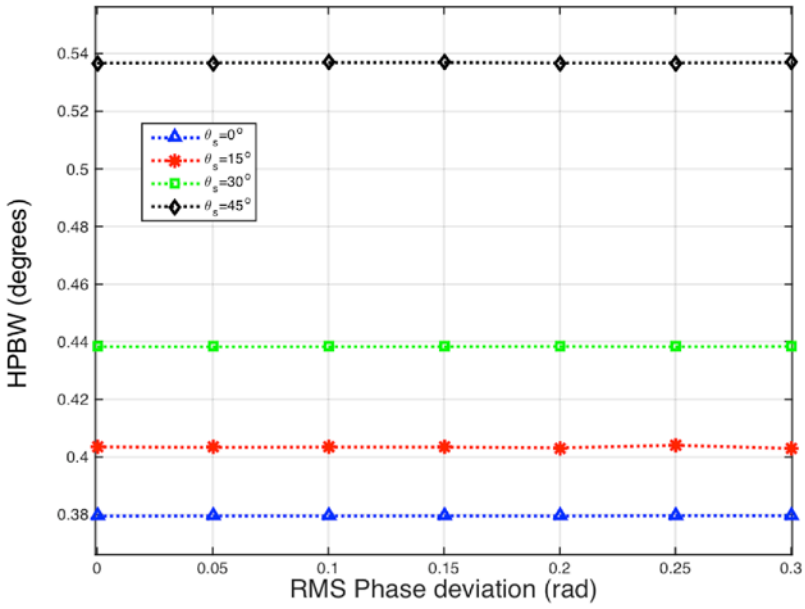

Figure 51. Half-Power Beamwidth vs. RMS Phase Deviation φ_{RMS} Plotted for Four Different Scanning Angles

3. *I* and *Q* Gain Unbalance Simulation Results

In this simulation the pattern degradation caused by *I* and *Q* gain unbalance was obtained; hence the subarray pattern accounting for these errors is given in (5.8), and the overall array pattern was computed using (3.6).

Similar to the previous case, the results in this section are the average of 100 trials for each scanning angle, i.e. 0^o, 15^o, 30^o and 45^o.

From the array patterns illustrated in Figure 52 one can conclude that this array configuration is not affected by small gain errors since Figure 52(a) shows a pattern for an array with gain errors up to 1 dB. Although the pattern shown in Figure 52(b) presents high sidelobes, to get this result the simulation considered gain unbalance up to 5 dB, which is unlikely to happen except for the major hardware failures. For instance, the specification of modulator ADL5375 from Analog Devices [37] for *I* and *Q* gain unbalance is only 0.08 dB.

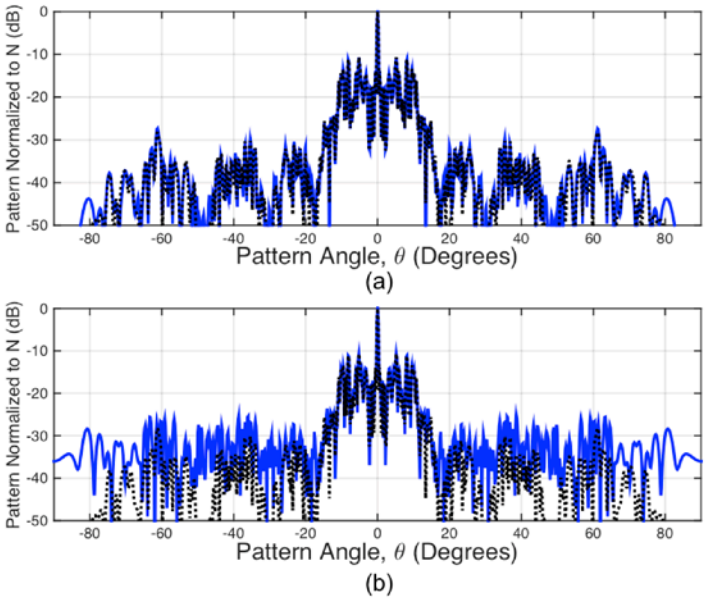

Figure 52. Linear Array of Subarrays Pattern Degraded Because of Unbalanced Gain (blue), and the Dotted Line is the Array without Errors (a) L= 1.0 dB and (b) L = 5.0 dB

In Figure 53 and Figure 54 the relative average and peak sidelobes plots, respectively, are shown. The sidelobe level increase is significant only for large gain unbalance. This confirms the previous statement that this type of error does not significantly affect the sidelobe level.

Regarding the gain loss results, when we compare the plots in Figure 29 and Figure 55, the loss for a linear array is slightly better than that for an array of subarrays. On the other hand, this simulation showed that the beam pointing performance, both average and relative standard deviation, for an array of subarrays is better than the linear array when the plots from Figure 30 and Figure 31 are compared with those in Figure 56 and Figure 57, respectively. The better beam pointing performance is a consequence of a larger array when the I and Q gain errors are normally distributed. If this assumption is true, and these errors are spatially uncorrelated, then the average approaches zero at the scanning angle. Finally, the graph in Figure 58 shows the half-power beamwidth as a function of gain unbalance, which obviously does not affect this characteristic.

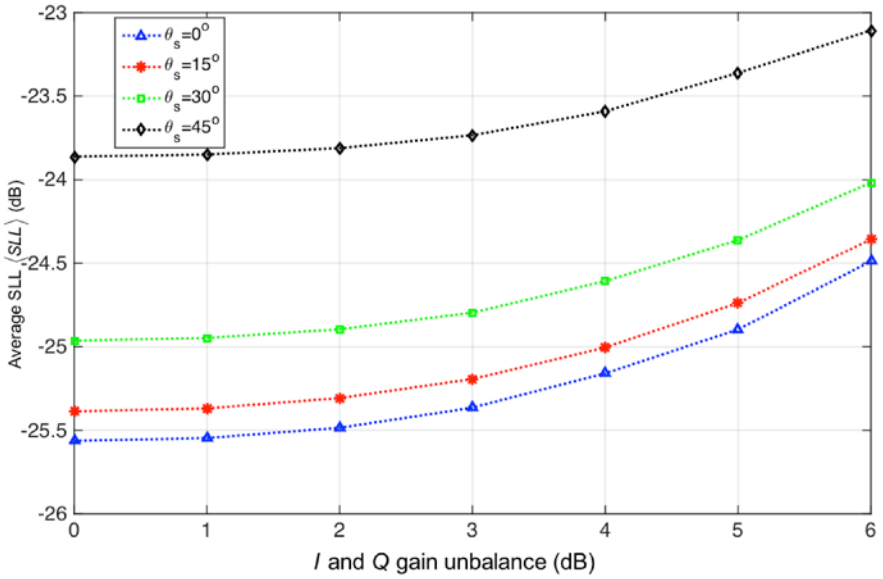

Figure 53. Relative Average Sidelobe $\langle SLL \rangle$ Increase Due to *I* and *Q* Gain Unbalance Plotted for Four Different Scanning Angles

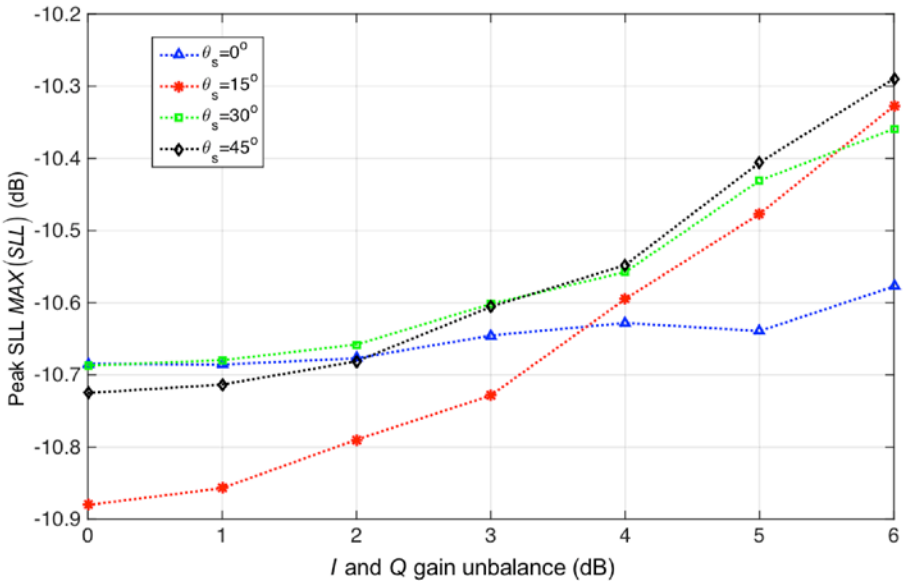

Figure 54. Relative Peak Sidelobe Level Increase Due to *I* and *Q* Gain Unbalance Plotted for Four Different Scanning Angles

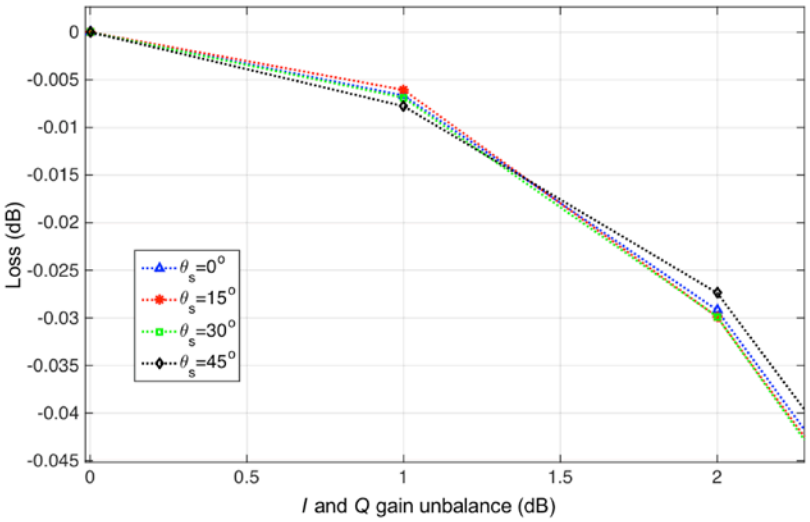

Figure 55. Array Gain Loss Due due to *I* and *Q* Gain Unbalance Plotted for Four Scanning Angles

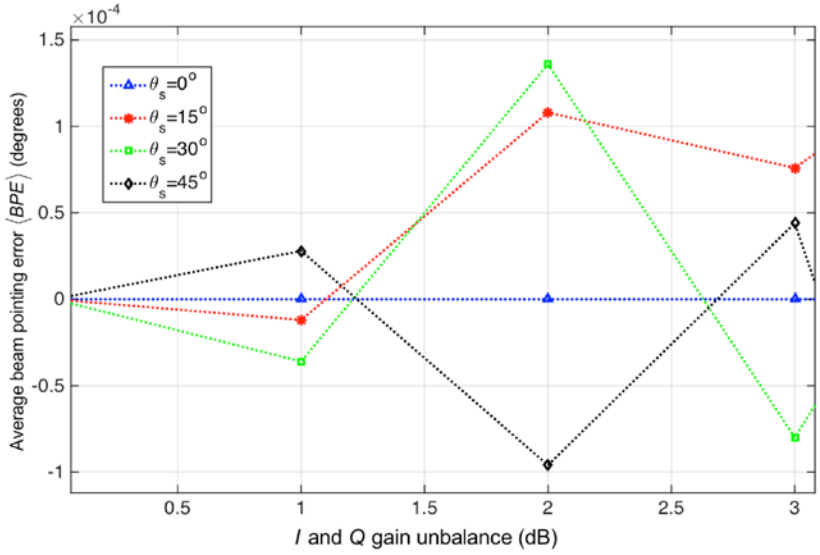

Figure 56. Average Beam Pointing Error $\langle BPE \rangle$ vs. *I* and *Q* Gain Unbalance Plotted for Four Different Scanning Angles

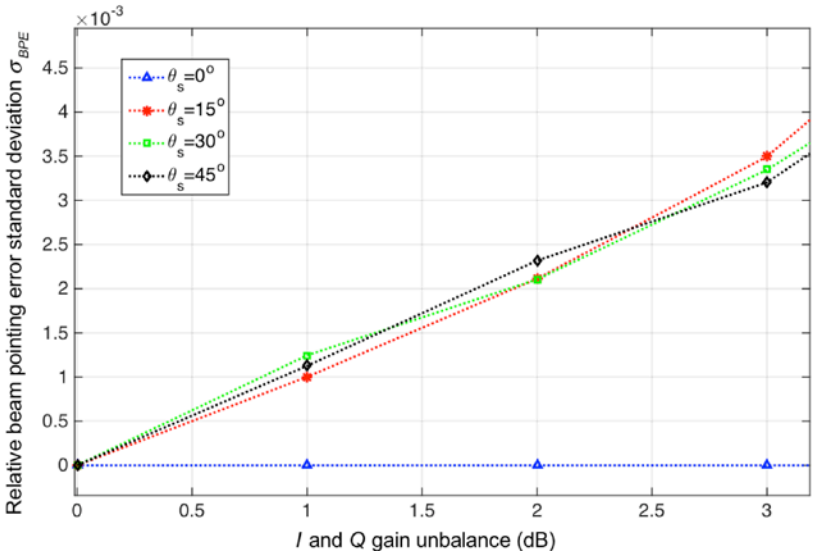

Figure 57. Relative Standard Deviation Beam Pointing Error σ_{BPE} vs. *I* and *Q* Gain Unbalance Plotted for Four Different Scanning Angles

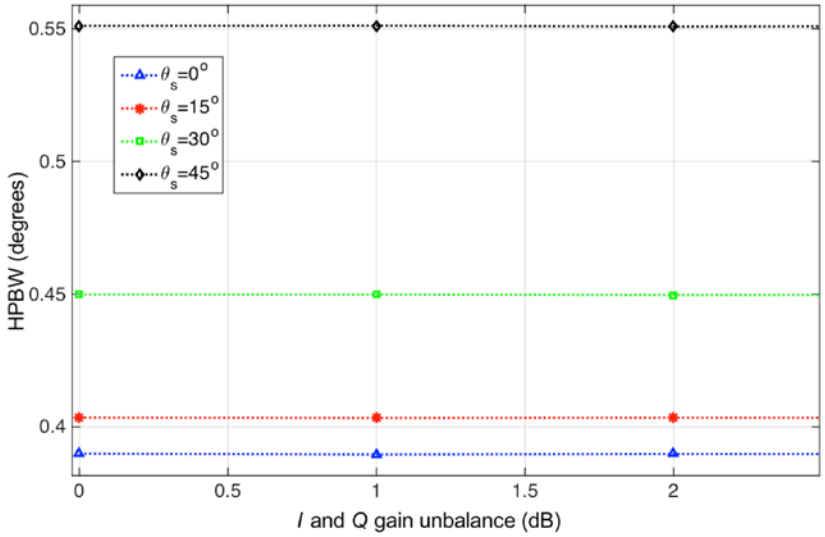

Figure 58. Half-Power Beamwidth vs. *I* And *Q* Gain Unbalance Plotted for Four Different Scanning Angles

F. TYPICAL SCENARIO

The objective of this section is to show an example of the impact of phase noise and gain unbalance on the array pattern using the information obtained from the data sheet of the COTS components.

Suppose a surface ship radar is operating at S-band, i.e., 3500 MHz, employing a uniform digital phased array design with one hundred elements, which are individually affected by phase errors. For this analysis the system bandwidth is 10 MHz. Shown in Figure 59 is a block diagram of a T/R module with non-ideal components, which are listed in Table 5.

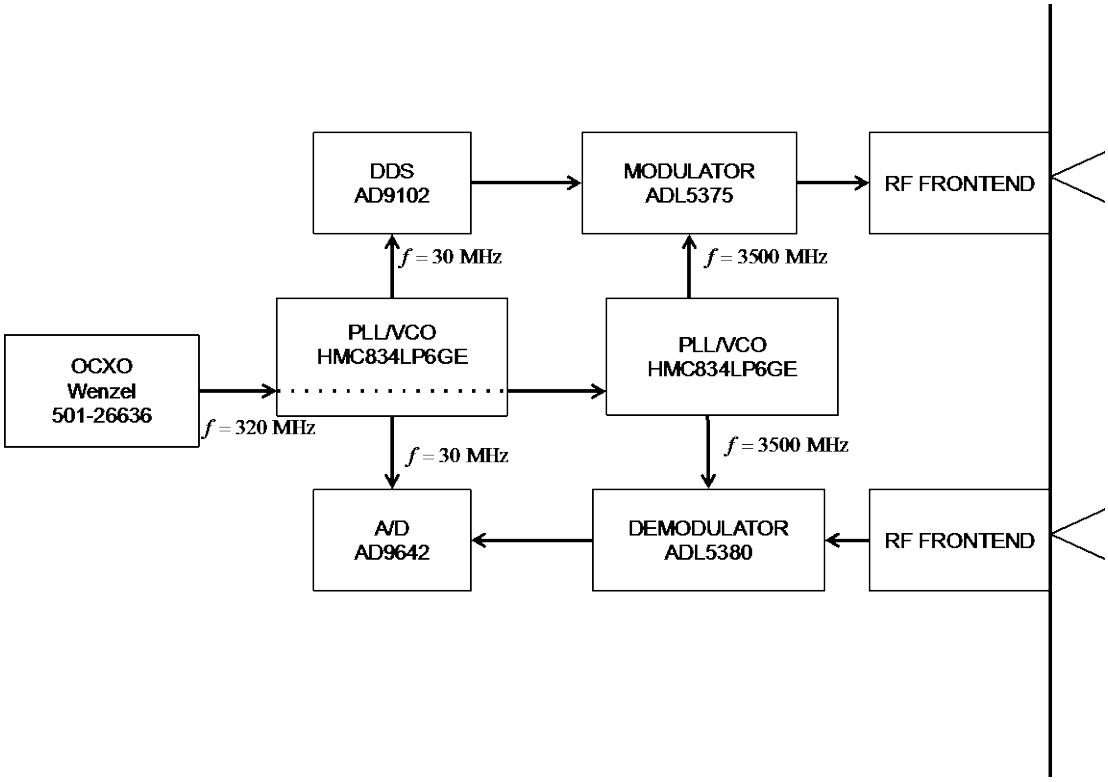

Figure 59. T/R Module Block Diagram Used as Example of Digital Phased Array with Non-Ideal Components

Table 5. Example T/R Module Components and Function

	Function	Manuf.	Model	Reference
Oven controlled crystal oscillator	Synchronization reference sent by DBF to elements	Wenzel	501-26636	[39]
Phased locked loop (VCO)	LO reference to digital components, modulator and demodulator.	Hittite	HMC834 LP6GE	[40]
Digital-to-Analog Converter and Waveform Generator	Digital waveform generator.	Analog Devices	AD9102	[41]
Analog-to-Digital Converter	Digitalization of received baseband signal.	Analog Devices	AD9642	[42]
Quadrature modulator	Modulate and upconvert the waveform using LO as carrier multiplier.	Analog Devices	ADL5375	[37]
Quadrature demodulator	Demodulate the received RF signal using LO as carrier multiplier.	Analog Devices	ADL5380	[43]

1. Calculating Phase Noise

In order to convert the phase noise specified in oscillators' datasheets to random phase φ, also defined as jitter in [44], the phase noise PSD has to be integrated over the signal bandwidth, which is equivalent to computing the area under the curve shown in Figure 60:

$$\left(\text{Phase Noise Power}\right) = \text{Area}_A + \text{Area}_B + \text{Area}_C + \text{Area}_D + \text{Area}_E. \tag{5.19}$$

The trapezoidal area marked in Figure 60 is an area on a log-log plot, which has *x* and *y* axis in logarithmic scale. The total random phase deviation is computed using the square-root sum of the individual phase noise contributors

$$\varphi_{RMS} = \sqrt{2\sum_{i=1}^{K-1}\left(\frac{10^{S_\varphi/10}}{f_i^{m_i}}\frac{1}{m_i+1}\right)\left[f_{i+1}^{m_i+1} - f_i^{m_i+1}\right]} \tag{5.20}$$

where the frequencies f_i are the corner frequencies between phase noise regions, K is the number of phase noise regions and m_i are the curve slopes defined as

$$m_i = \frac{S_\varphi(f_{i+1}) - S_\varphi(f_i)}{\log_{10}(f_{i+1}) - \log_{10}(f_i)}. \tag{5.21}$$

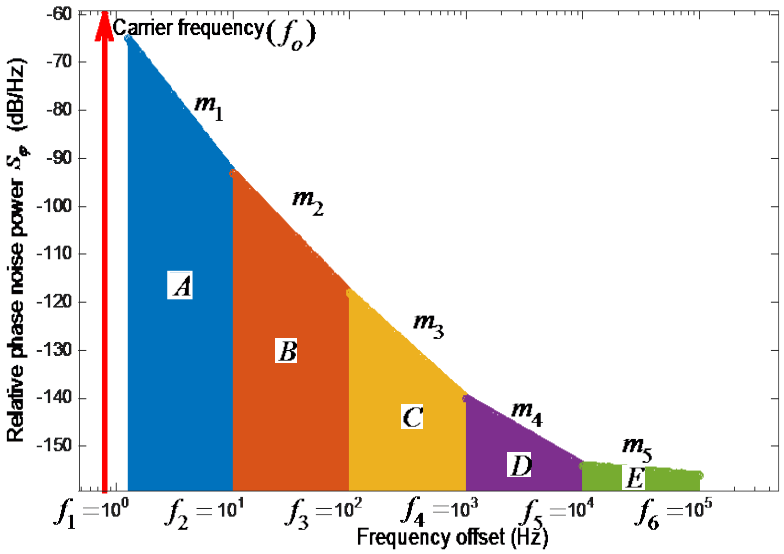

Figure 60. Phase Noise Frequency-Domain Representation of A MCXO Model Vectron MX-503. The Colored Area under the Curve Represents the Phase Noise Power

Adapted from [1]: W. Kester, (2008, Dec.). "Converting Oscillator Phase Noise to Time Jitter," 2008. [Online]. Available: http://www.analog.com/media/en/training-seminars/tutorials/MT-008.pdf.

The upper limit for integration (number of phase noise regions) is determined by signal single-sided bandwidth, whereas the lower limit is found on the LO data sheet. In practice, data sheets usually provide phase noise values from 100 Hz to 1 MHz of frequency offset, neglecting the phase noise close to the carrier, because the majority of the jitter is due to the WPM noise. Alternatively, there are online calculators and

spreadsheets that convert the phase noise to RMS φ_{RMS} in radians or jitter in seconds, like the one found in [45].

In order to calculate the cumulative effect of phase noise for two or more components, the noise power of the individual component contributions is summed

$$\varphi_{RMS} = \sqrt{2\sum_{j=1}^{N}\sum_{i=1}^{K-1}\left(\frac{10^{S_{j\varphi}/10}}{f_{ij}^{m_i}}\frac{1}{m_{ij}+1}\right)\left[f_{ij+1}^{m_{ij}+1} - f_{ij}^{m_{ij}+1}\right]} \tag{5.22}$$

where

f_{ij} = the corner frequencies between phase noise regions of the j^{th} component in the cascade,

m_{ij} = i^{th} phase noise region curve slope of the j^{th} component in the cascade, and

N = number of components in cascade.

2. Crystal Oscillator Wenzel 501-26636

In the proposed scenario the XO Wenzel 501-26636 is the reference transmitted from the DBF to the T/R modules for synchronization. From the manufacturer data sheet the XO phase noise is listed in Table 6.

Using (5.20), we get the RMS value for random phase deviation at 320 MHz:

$$\varphi_{RMS}\big|_{f=320\text{MHz}} = 1.135\times10^{-4} \text{ rad.} \tag{5.23}$$

Table 6. XO Wenzel 501-26636 Phase Noise Specification

100 Hz	-118 dBc/Hz
1 kHz	-141 dBc/Hz
10 kHz	-151 dBc/Hz
100 kHz	-152 dBc/Hz

3. Voltage Controlled Oscillator Hittite HMC834LP6GE

The reference signal from the XO Wenzel 501-26636 is used for frequency synthesis using VCO Hittite HMC834LP6GE, whose phase noise specification is shown in Table 7 and Table 8.

Table 7. VCO Hittite HMC834LP6GE Phase Noise Specification at 4 GHz

10 kHz	-78 dBc/Hz
100 kHz	-108 dBc/Hz
1 MHz	-134 dBc/Hz
10 MHz	-156 dBc/Hz
100 MHz	-171 dBc/Hz

At 4 GHz, the RMS value for random phase deviation is

$$\varphi_{RMS}\big|_{f=4\text{GHz}} = 0.0126 \text{ rad.} \tag{5.24}$$

Table 8. VCO Hittite HMC834LP6GE Phase Noise Specification at 100 MHz

10 kHz	-111 dBc/Hz
100 kHz	-141 dBc/Hz
1 MHz	-163.5 dBc/Hz
10 MHz	-170 dBc/Hz
100 MHz	-173 dBc/Hz

At 100 MHz, the RMS value for random phase deviation is

$$\varphi_{RMS}\big|_{f=100\text{MHz}} = 2.8312\times10^{-4}\ \text{rad.} \tag{5.25}$$

Adding the contribution from reference XO, we get the LOs reference signal for the modulator and demodulator with a random phase deviation of

$$\varphi_{RMS_{LO}} = \sqrt{(\varphi_{RMS}\big|_{f=320\text{MHz}})^2 + (\varphi_{RMS}\big|_{f=4\text{GHz}})^2}$$

$$= \sqrt{(1.135\times10^{-4})^2 + (0.0126)^2} \tag{5.26}$$

$$= 0.0126\ \text{rad.}$$

The clock reference signal for the DDS and A/D converter has a random phase deviation of

$$\varphi_{RMS_{clk}} = \sqrt{(\varphi_{RMS}\big|_{f=320\text{MHz}})^2 + (\varphi_{RMS}\big|_{f=100})^2}$$

$$= \sqrt{(1.135\times10^{-4})^2 + (2.8312\times10^{-4})^2} \tag{5.27}$$

$$= 3.0501\times10^{-4}\ \text{rad.}$$

Notice for low frequencies the phase noise contribution is negligible; on the other hand, for high frequencies, the phase noise increases significantly. In Table 9, the expected pattern alteration due to phase noise is summarized.

Table 9. Pattern Degradation Due to LO Phase Noise

	$\theta_s = 0^\circ$	$\theta_s = 15^\circ$	$\theta_s = 30^\circ$	$\theta_s = 45^\circ$
Average SLL increase (dB)	0.4	0.42	0.39	0.3
Peak SLL increase (dB)	0.72	0.64	0.7	0.71
Loss (dB)	0.05	0.05	0.05	0.05
Relative beam pointing error standard deviation	0.0035	0.0035	0.0039	0.0044

4. Phase Errors Due to *I* and *Q* Gain Unbalance

For the proposed scenario, the modulator ADL5375 and the demodulator ADL5380 have the *I* and *Q* gain unbalance listed in Table 10. Additionally, the DDS (AD9102) and A/D converter (AD9642) contribute with a gain error of 1% and 2%, respectively. This is equivalent to an additional gain error of 0.04 dB in transmission and 0.08 dB on reception.

Table 10. Modulator, Demodulator Gain Unbalance at 3500 MHz, and DDS and A/D Converter Gain Error

Modulator ADL5375 (dB)	0.08
Demodulator ADL5380 (dB)	0.14
DDS AD9102 (dB)	0.04
A/D converter AD9642 (dB)	0.08

In Table 11 and Table 12, the pattern degradation due to transmission and reception gain errors, respectively, are summarized.

Table 11. Pattern Degradation Due to Transmission *I* and *Q* Gain Unbalance

	$\theta_s = 0^\circ$	$\theta_s = 15^\circ$	$\theta_s = 30^\circ$	$\theta_s = 45^\circ$
Average SLL increase (dB)	0.03	0.03	0.02	0.03
Peak SLL increase (dB)	0.06	0.1	0.14	0.11
Loss (dB)	$3x10^{-5}$	$6x10^{-5}$	$3x10^{-5}$	$2x10^{-4}$
Relative beam pointing error standard deviation	0.0316	0.0316	0.0316	0.0316

Table 12. Pattern Degradation Due to Transmission *I* and *Q* Gain Unbalance

	$\theta_s = 0^\circ$	$\theta_s = 15^\circ$	$\theta_s = 30^\circ$	$\theta_s = 45^\circ$
Average SLL increase	0.11 (dB)	0.12 (dB)	0.1 (dB)	0.07 (dB)
Peak SLL increase	0.18 (dB)	0.32 (dB)	0.3 (dB)	0.3 (dB)
Loss	$5x10^{-4}$ (dB)	$1x10^{-4}$ (dB)	$2x10^{-4}$ (dB)	0 (dB)
Relative beam pointing error standard deviation	0.0608	0.0608	0.0608	0.0608

5. Overall Pattern Degradation

In Table 13, the overall pattern degradation due to phase noise and gain errors, accounting for transmission and reception, is summarized. Although the components used in this example have small errors individually, the pattern degradation due to the combined effect of phase noise and gain error is not negligible.

Table 13. Overall Pattern Degradation

	$\theta_s = 0^\circ$	$\theta_s = 15^\circ$	$\theta_s = 30^\circ$	$\theta_s = 45^\circ$
Average SLL increase (dB)	0.94	0.99	0.9	0.7
Peak SLL increase (dB)	1.68	1.7	1.84	1.83
Loss (dB)	0.1	0.1	0.1	0.1
Relative beam pointing error standard deviation	0.0687	0.0687	0.0687	0.0687

G. SUMMARY

In this chapter, the array pattern degradation was analyzed using results generated from equations programed in MATLAB to simulate and compute the pattern characteristics: average sidelobe level, peak sidelobe level, gain loss, average and relative standard deviation for beam pointing error, and HPBW.

Phase noise and *I* and *Q* gain unbalance were simulated for two different scenarios: a uniform linear array and a linear array of subarrays. In both cases, the results show a significant increase in sidelobe levels but small gain loss. For the uniform linear array scenario, the beam pointing error is larger than for a linear array of subarrays because of the difference in size between the arrays.

For phase errors caused by element mislocation, only the uniform linear array scenario was simulated. The results show that small deviations can produce significant degradation in sidelobe level and beam pointing error; moreover, the pattern characteristics are worse for oblique angles. The gain loss is not significantly affected.

In Section D.4, the relationship of the non-synchronization interval to the non-ideal oscillator accuracy was addressed. For this simulation, the oscillator was modeled to have linear frequency drift. From the simulation results, one can conclude that the pattern resilience depends on the oscillator accuracy and the system nominal frequency.

In Section F, a typical scenario analysis for a uniform linear array constituted of COTS components was presented. In the next chapter, a summary, the conclusions of this research, and suggestions for future work are presented.

VI. CONCLUSION AND FUTURE WORK

The primary objective of this research was to analyze phased array digital beamforming degradation under the influence of phase errors caused by phase noise, *I* and *Q* gain unbalance and element mislocation. Parametric simulations were programmed in MATLAB to perform Monte Carlo simulations of hardware errors using equations and models studied in the literature review. The simulation results can be used as reference to establish acceptable tolerance limits for phase errors.

In the first four chapters of this thesis the literature review of topics related to digital phased array antennas was presented. The literature review focused on the technologies and techniques that affect the coherency among the array elements, which is vital for beamforming. Appropriate error models were developed and implemented in MATLAB.

Analyzing the T/R module architecture, two main sources for phase errors were identified: phase noise and gain unbalance between *I* and *Q* branches. Every digital and analog component that requires a reference signal is affected by local oscillator phase noise. Moreover, gain unbalance between *I* and *Q* branches can be a source of phase errors in quadrature modulators and demodulators.

In order to build the simulation scenarios, modifications to the standard digital array pattern equations were proposed to account for phase noise, *I* and *Q* gain unbalance and element mislocation.

Additionally, the mathematical models for instantaneous phase and phase noise were presented and were used to model the local oscillator used in the simulations. The phase noise model was based on the *power-law* model, which is an approximation frequently used for oscillators.

A. CONCLUSION

The array pattern degradation was observed from the analysis of the sidelobe level (average and peak), gain loss and beam pointing error (average and standard deviation). Phase noise, *I* and *Q* gain unbalance, element mislocation and frequency linear drift were the phase error sources studied in these experiments.

Initially, the established simulation scenario consisted of 100 elements uniformly distributed. The element separation distance was 0.2 wavelengths. For phase noise and *I* and *Q* gain unbalance, there was a noticeable increase in sidelobe levels and beam pointing error proportional to the phase error. On the other hand, the gain loss was not significant in both cases.

Additionally, for the same scenario, the effect of linear frequency drift on the array pattern was simulated. From the simulation results, we see a relationship between pattern distortion, oscillator accuracy and system nominal frequency. If a less accurate device replaces an oscillator that has less frequency drift, the synchronization interval must decrease proportionally to maintain the pattern characteristics. In a similar fashion, higher frequency systems must be synchronized more often.

For element mislocation simulations, the scenario was slightly different (50 elements, uniformly distributed with separation distance between elements of 0.4 wavelength); however, the observed effects were the same. That is, a significant increase of sidelobe level and beam pointing error resulted. Additionally, it was observed that for more oblique scanning angles, the degradation of these pattern characteristics was more significant.

The experiments for phase noise and *I* and *Q* gain unbalance were repeated for an array of subarrays scenario, with 20 subarrays randomly spaced from one another within four and five wavelengths. Each subarray was set to have ten elements. In both cases, the simulation results showed a significant increase in sidelobe levels due to grating lobes in addition to the effects of the simulated phase errors (phase noise and gain unbalance), but in contrast a small value of array gain loss was found. Compared to the uniform linear array scenario, this experiment obtained better performance for beam pointing error

parameters, which is attributed to the size of the array and the assumption of spatially uncorrelated errors among the elements.

In addition to the error sources examined in this study, there exist other factors related to phase errors that were not considered in this research:

1. Digital components of the array introduce quantization errors
2. System thermal noise was neglected
3. Transmission and reception coupling

In Chapter V, Section F, a typical radar scenario was analyzed using information from COTS components' specifications. Among the array pattern characteristics, the sidelobe level was most affected by phase errors (average increase of 1 dB), but the significance of the degradation depends upon the system requirements. The beam pointing error was also significant in this example, but it decreases if the size of the array increases. Overall gain is not significantly affected by the phase errors considered in this research. Array designers can use a similar analysis to establish phase error limits based on the desired pattern characteristics.

B. FUTURE WORK

1. Phase Noise Analysis for EHF Systems

More recently, the demand for bandwidth pushed the research for radar systems to higher frequencies, such as EHF or millimetric waves, which requires high performance components; therefore, these systems require multiple upconversion and downconversion stages, which have an impact on phase noise.

Moreover, each of these stages require non-linear devices (mixers) to perform frequency multiplication, increasing the probability of IM products being generated. These spurious frequencies increase the correlated phase noise, which can degrade the array pattern even more.

2. LO Distribution Techniques

The transmission of the LO signal through a channel and its recovery using non-ideal devices introduce noise that is transferred to other components in form of phase noise. Moreover, the synchronization process also adds phase errors due to discrete phase shifters. It is important to model the impact of these errors on phase noise and account for them in the array pattern.

Alternatively, the array elements can be locally synchronized by a LO distribution system divided into levels. The first level elements are synchronized to a LO, which is linked to the reference of LO in level two. These second level LOs are directly connected to the DBF. Depending on the size of the array, we add more levels of LO; consequently, the random errors are also added in a chain effect.

APPENDIX. LOCAL OSCILLATORS

Some of the typical oscillator architectures and technology and examples of available COTS devices are described in this section.

a. Crystal Oscillators

In reference [46], the author describes the construction and operation of four types of crystal oscillators.

(1) Crystal Oscillators

A crystal oscillator (XO) usually has quartz as a resonance element. Quartz is a monocrystal of silicon dioxide (SiO_2), which is cut and packetized to supply a constant and stable resonance frequency. To differentiate from other XOs, they are also called packaged crystal oscillators (PXOs) [46].

The limit for resonance frequency depends on the crystal mode of oscillation. In Figure 61 (a) and (b) are illustrated the two low frequency modes, flexural and torsional, commonly found in tuning fork resonators. For medium frequencies the contour mode is usually encountered, exemplified in Figure 61 (c); to obtain higher frequencies the thickness mode is used, which is illustrated in Figure 61 (d). For the latter mode, resonance frequency is inversely proportional to the crystal thickness, so the cut of the crystal also influences in its performance [17].

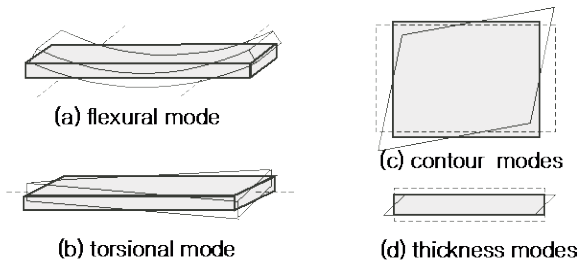

Figure 61. The Four Possible Modes of Oscillation for Quartz Crystals

Source [17]: E. Vittoz, *Low-Power Crystal and MEMS Oscillators: The Experience of Watch Developments*. Lausanne: Springer Science+Business Media B.V., 2010, p.16.

(2) Temperature Compensated Crystal Oscillators

Temperature variations might change the resonator characteristics, degrading the oscillator accuracy. Temperature compensated crystal oscillators (TCXO) use a temperature sensor signal to control a variable capacitor in the oscillator network; therefore, the reactance is adjusted despite the temperature variation [46]. According to [46] a TCXO is 20 times more stable than a XO.

(3) Oven Controlled Crystal Oscillators

Oven controlled crystal oscillators (OCXO) have an oven, which is an enclosed structure, to stabilize the sensitive elements of the oscillator, such as the crystal. The oven is adjusted to a temperature where the crystal is stable. The OCXO is 1000 times more stable than XO [46].

(4) Microcomputer Compensated Crystal Oscillators

The microcomputer compensated crystal oscillators (MCXO) use a microcomputer to measure and compensate the temperature effects over the resonator. There are two types of MCXO, one using pulse deletion and other using frequency summation. The former method has a resonator that is tuned slightly above the desired frequency; then pulses are eliminated to compensate the temperature effect. For frequency summation, the microcomputer uses a DDS to generate a frequency compensation to be added to resonator output frequency; the result is a constant frequency [46].

b. Atomic Standards and Chip Scale Atomic Clock

All atomic frequency standards available on the market take advantage of hydrogen-like atom gases, which have one “unpaired electron in a symmetric orbit” [46]. In short, the physical concept behind the atomic resonator consists of a beam radiation at the frequency that causes an electron excitation on a hydrogen-like gas, which forces the atoms to change their energy level. Based on the element characteristics, some different techniques are used to extract the energy state frequency information and are illustrated in the next sections.

(5) Cesium Beam Frequency Standard

The cesium beam frequency standard (CsFS) is illustrated in Figure 62. The CsFS has a cesium gas that is accelerated, forming an atomic beam, which is submitted to a magnetic field that selects the lower energy state atoms. These atoms form a beam that is directed to a microwave cavity. Once the correct frequency is transmitted inside the cavity, the atoms are stimulated to change energy state. A probe is used to transmit the signal in the cavity. A high-energy state cesium beam is formed, and then, it is submitted to another magnetic field. When the beam hits the detector, the system knows the frequency of 9,192,631,770 Hz is in the cavity [47].

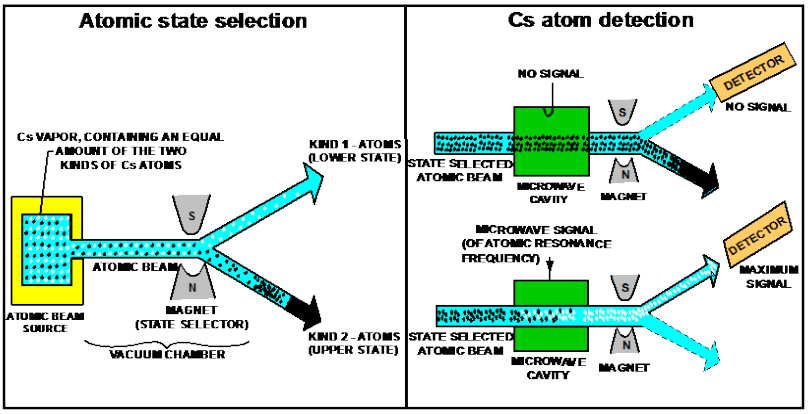

Figure 62. CsFS Operation. Left the Atomic State Selection. Right Beam Detection

Source [46]: J. R. Vig, (2015, Nov10) Quartz Crystal Resonators and Oscillators - For Frequency Control and Timing Applications—A Tutorial. [Online]. Available: http://www.ieee-uffc.org/frequency-control/learning-vig-tut.asp.

(6) Rubidium Frequency Standard

Rubidium frequency standard (RbFS) is another type of atomic standard that uses characteristics of the rubidium (Rb) atom that absorbs a specific radiation frequency to change state. In Figure 63 is illustrated a RbFS block diagram. The ^{87}Rb lamp radiates light that can be absorbed by Rb-87 buffer gas with high-energy state. When the radiation in the cavity has the exact frequency of 6.834,682,608 GHz, the ^{87}Rb changes from low

energy state to high. Consequently, the light is partially absorbed by the gas and power on the photo cell drops. A quartz VCXO is used to control the frequency in the cavity. To work properly, the light must not have the 795 nm wavelength component because it prevents the ^{87}Rb atom from changing state; for this reason a filter of ^{85}Rb is used [46].

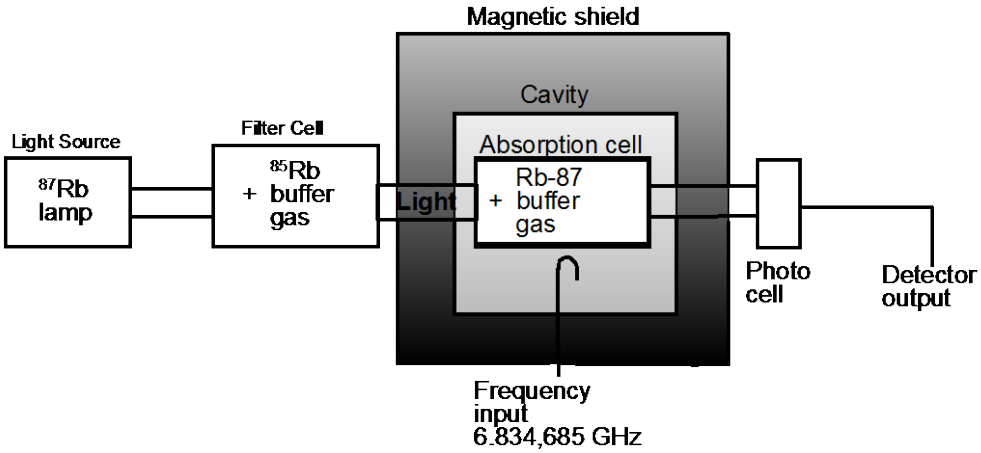

Figure 63. Rbfs Operation Block Diagram

Adapted from [46] J. R. Vig, (2015, Nov10) Quartz Crystal Resonators and Oscillators - For Frequency Control and Timing Applications - A Tutorial. [Online]. Available: http://www.ieee-uffc.org/frequency-control/learning-vig-tut.asp.

(7) Hydrogen Maser Frequency Standard

In a Hydrogen maser standard (H-maser), a beam of hydrogen atoms is formed by electrical discharge on the gas. A magnetic field is used to select the beam of atoms that has a certain energy state, and it is directed to a microwave cavity. The cavity is excited with a FM signal at 1,420,405,751.77 Hz, which induces the atoms to transition. Consequently, the cavity transmits an AM signal through a probe, and the desired frequency is extracted from the signal envelope [48].

(8) Chip Scale Atomic Clock

The great challenge for the development of a chip scale atomic clock (CSAC) is the fact that all conventional technologies use a microwave cavity, limiting the dimension

reduction. The solution to this is the coherent population trapping (CPT) technique. In Figure 64 is illustrated the block diagram of a CSAC.

The vertical-cavity surface emitting lasers (VCSELs) transmit two laser beams, whose frequencies are controlled. Then a procedure called interrogation is performed. The beams, directed to the gas, have to be collinear and circularly polarized. Two frequency values are important: the difference between the two beams frequency, and the laser center frequency. Both are selected in order to excite the atoms to an optically excited state; when "the difference frequency between the two laser fields equals the ground state hyperfine splitting, a coherence is generated in the atomic vapor" [31]. Consequently, the atoms that are coherently excited do not scatter the laser beam, and the power on the detector increases [31].

Two important technological advances were necessary to allow the CSAC construction and manufacturing. First was to confine high-pressure cesium vapor at 65^{o}C in a milimetric cell. Another necessary technological advance was the use of high bandwidth VCSELs, which are necessary to the interrogation process [31].

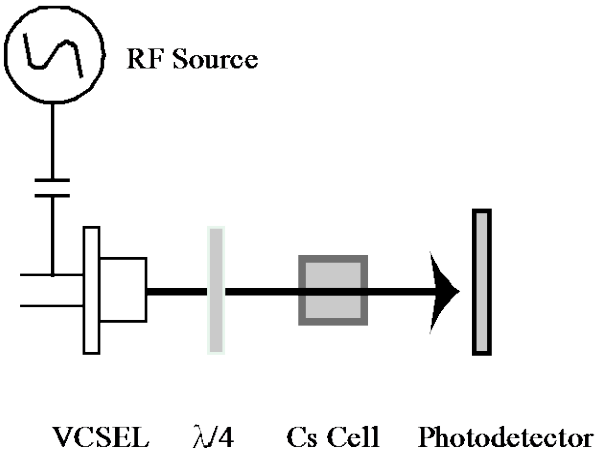

Figure 64. CSAC Using Coherent Population Trapping Technique

Source [31]: R. Lutwak, D. Emmons, W. Riley, and R. M. Garvey, "The Chip-Scale Atomic Clock – Coherent Population Trapping Conventional Interrogation," *34th Annual Precise Time and Time Interval (PTTI) Meeting*. Beverly, MA, pp. 542, 2002.

c. Voltage Controlled Oscillators

Oscillators are expected to have low phase noise, high Q-factor and small drift; crystal oscillators are used because they meet these requirements. Additionally, some applications demand also a tunable signal reference.

An oscillator that is designed to change its resonance frequency has the drawback of being more susceptible to unintentional tuning [46]. Consequently, an oscillator has stability inversely proportional to tuning range due to changes in resonance element load reactance; however, a VCO is still one of the most important devices for synchronized systems.

Frequency tuning in a VCO is performed using a variable reactance load on the resonant element, which changes its oscillation period. Usually a varactor is employed for this task. For relaxation oscillators, the variable capacitance changes the discharge time, while LC oscillators change their natural oscillation frequency; however, there are many techniques to implement a VCO for different requirements of phase noise, Q-factor and accuracy.

In Table 14, several COTS oscillators and their performance specifications are listed.

Table 14. Oscillator Performance Comparison

Type	Model	Range (MHz)	Phase noise (dBc)	Accuracy (ppm)	Reference
VCXO	Crystal CCO-083	10-200	-80 @ 10 Hz -112 @ 100 Hz -140 @ 1 kHz -150 @ 10 kHz	±25	[49]
OCXO	Crystal CO27VS05DE	10	-102 @ 10 Hz -132 @ 100 Hz -150 @ 1 kHz -152 @ 10 kHz	±0.2	[50]
TCXO	Crystal CVT32	10-30	-83 @ 10 Hz -115 @ 100 Hz -135 @ 1 kHz -140 @ 10 kHz	±2.5	[51]
MCXO	Vectron MX-503	8-26	-65 @ 1 Hz -93 @ 10 Hz -118@ 100 Hz -140 @ 1 kHz -154 @ 10 kHz -156 @ 100 kHz	±0.5	[52]
VCO	Vectron VS-705	120-1000	-30 @ 10 Hz -60 @ 100 Hz -85 @ 1 kHz -105 @ 10 kHz -130 @ 100 kHz	±100	[53]
CsFS	Microsemi 5071A	5	-106 @ 1 Hz -130 @ 10 Hz -145 @ 100 Hz -150 @ 1 kHz -154 @ 10 kHz -154 @ 100 kHz	± 0.000001	[38]
RbFS	Symmetricon 8040C	5	-72 @ 1 Hz -95 @ 10 Hz -130 @ 100 Hz -140 @ 1 kHz -148 @ 10 kHz	± 0.00005	[54]
CSAC	Microsemi Quantum SA.45s CSAC	10	-50 @ 1 Hz -70 @ 10 Hz -113 @ 100 Hz -128 @ 1 kHz -135 @ 10 kHz -140 @ 100 kHz	± 0.00005	[55]

THIS PAGE INTENTIONALLY LEFT BLANK

LIST OF REFERENCES

[1] H. T. Friis and C. B. Feldman, "A multiple unit steerable antenna for short-wave reception," *Proc. Inst. Radio Eng.*, vol. 25, no. 7, pp. 337–419, 1937.

[2] R. J. Mailloux, "A history of phased array antennas," in *History of Wireless*, Amherst, MA, John Wiley & Sons, 2006, pp. 567–603.

[3] D. Jenn, Y. Loke, T. C. H. Matthew, Y. E. Choon, O. C. Siang, and Y. S. Yam, "Distributed phased arrays and wireless beamforming networks," *Int. J. Distrib. Sens. Networks*, vol. 5, no. 4, pp. 283–302, 2009.

[4] "MWR-05XP mobile phased array weather radar." (n.d.). *Center for Interdisciplinary Remotely-Piloted Aircraft Studies*, 2014. [Online]. Available: http://www.cirpas.org/mobileRadarTruck.html. [Accessed: 07-Dec-2015].

[5] D. Ehyaie, "Novel approaches to the design of phased array antennas," Ph.D. dissertation, Horace H. Rackham School of Graduate Studies, University of Michigan, 2011.

[6] "Ballistic missile defense: The Aegis SPY-1 Radar." (2013). Mostly Missile Defense. [Online]. Available: http://mostlymissiledefense.com/2012/08/03/ ballistic-missile-defense-the-aegis-spy-1-radar-august-3-2012/. [Accessed: 23-Nov-2015].

[7] "Common starting point for phased array programs may save billions, years off development." (2013). [Online]. Available: http://www.darpa.mil/news-events/ 2013-02-26. [Accessed: 23-Nov-2015].

[8] "Phased array antenna," Hughes Aircraft Co., Culver City, CA (unpublished photo).

[9] B. Feng and D. C. Jenn, "Two-way pattern grating lobe control for distributed digital subarray antennas," *IEEE Trans. Antennas Propag.*, vol. 63, no. 10, pp. 4375–4383, 2015.

[10] L. B. Oliveira, J. R. Fernandes, I. M. Filanovsky, C. J. M. Verhoeven, and M. M. Silva, *Analysis and Design of Quadrature Oscillators*, Vol. 1. Lausanne, Switzerland: Springer Science+Business Media B.V., 2008.

[11] R. Mailloux, *Phased Array Antenna Handbook*, 2nd ed. Norwood, MA: Artech House, 2005.

[12] Y. Loke, "Sensor synchronization, geolocation and wireless communication in a shipboard opportunistic array," M.S. thesis, Department of Electrical and Computer Engineering, Naval Postgraduate School, 2006.

[13] Y.-C. Tsai, “Development of the phase synchronization circuit for wirelessly distributed digital phased array,” M.S. thesis, Department of Information Sciences, Naval Postgraduate School, 2009.

[14] P. Djerf and I. Tornazakis, “Development of a distributed digital array radar (DDAR),” M.S. thesis, Department of Information Sciences, Naval Postgraduate School, 2008.

[15] S. Bregni, *Synchronization of Digital Telecommunications Networks*, Vol. 1. Hoboken, NJ: John Wiley & Sons, 2002.

[16] Texas Instruments, “AN-1728 IEEE 1588 precision time protocol time synchronization performance,” Dallas, TX, 2007.

[17] E. Vittoz, *Low-Power Crystal and MEMS Oscillators: The Experience of Watch Developments*. Lausanne, Switzerland: Springer Science+Business Media B.V., 2010.

[18] S. A. Maas, “System considerations,” in *Microwave Mixers*. Boston: Artech House, 1993, pp. 153–185.

[19] M. Skolnik, *Radar Handbook*, 3rd ed. Baltimore, MD: The McGraw-Hill Companies, 2008.

[20] S. J. Roome, “Analysis of quadrature detectors using complex envelope notation,” *Radar Signal Process. IEE Proc.*, vol. 136, no. 2, p. 95, 1989.

[21] M. A. Lombardi, “Fundamentals of time and frequency,” in *The Mechatronics Handbook*. Boca Raton, FL: CRC press, 2001, pp. 17.1–17.18.

[22] “Precision clock synchronization protocol for networked measurement and control systems.” IEEE 1588 standard, 2004.

[23] B. Razavi, “A study of injection locking and pulling in oscillators,” *IEEE J. Solid-State Circuits*, vol. 39, no. 9, pp. 1415–1424, 2004.

[24] K. Kundert. (2015, Oct.23). “Predicting the phase noise and jitter of PLL-based frequency synthesizers, version 4i.” [Online]. Available: http://www.designers-guide.org/analysis/PLLnoise+jitter.pdf.

[25] V. F. Krou, “Noise in resonators and oscillators,” in *Frequency Stability*, IEEE Press, 2012, pp. 37–63.

[26] “Voltage Controlled Oscillator ROS-2600-1119+.” (n.d.). [Online]. Available: http://www.minicircuits.com/pdfs/ROS-2600-1119+.pdf. [Accessed: 10-Nov-2015].

[27] D. B. Leeson, “A simple model of feedback oscillator noise spectrum,” *Proc. IEEE*, vol. 54, no. 2, pp. 329–330, 1966.

[28] R. W. Rhea, “Noise,” in *Discrete Oscillator Design: Linear, Nonlinear, Transient, and Noise Domains*. Norwood, MA, Artech House, 2010, pp. 173–216.

[29] D. Scherer, “Generation of low phase noise microwave signal,” in *RF & Microwave Measurement Symposium and Exhibition*, 1981, pp. 1–31.

[30] B. P. Lathi, *Modern Digital and Analog Communication Systems*, 2nd ed. Sacramento, CA: The Dryden Press, 1989.

[31] R. Lutwak, D. Emmons, W. Riley, and R. M. Garvey, “The chip-scale atomic clock – Coherent population trapping conventional interrogation,” *34th Annual Precise Time and Time Interval (PTTI) Meeting*. Beverly, MA, pp. 539–550, 2002.

[32] M. I. Skolnik, “Nonuniform arrays,” in *Antenna Theory Part 1*, New York: McGraw-Hill, 1969, pp. 207–234.

[33] “Taylorwin” (n.d.). Mathworks. [Online]. Available: http://www.mathworks.com/help/signal/ref/taylorwin.html?searchHighlight=taylorwin. [Accessed: 21-Nov-2015].

[34] “sigwin.taylorwin class.” (n.d.) Mathworks. [Online]. Available: http://www.mathworks.com/help/signal/ref/sigwin.taylorwin-class.html. [Accessed: 21-Nov-2015].

[35] E. W. Weisstein, “Gaussian quadrature.” (n.d.). [Online]. Available: http://mathworld.wolfram.com/GaussianQuadrature.html. [Accessed: 21-Nov-2015].

[36] M. Abramowitz, I. Stegun, and D. Miller, *Handbook of Mathematical Functions with Formulas, Graphs and Mathematical Tables (National Bureau of Standards Applied Mathematics Series No. 55)*, Vol. 32, No. 1, 1965.

[37] “Data sheet: 400 MHz to 6 GHz Broadband Quadrature Modulator.” (n.d.) *Analog Devices*, 2007. [Online]. Available: http://www.analog.com/media/en/technical-documentation/evaluation-documentation/ADL5375.pdf. [Accessed: 16-Dec-2015].

[38] “Data sheet: 5071A primary frequency standard.” (2014). *Microsemi Corporation*. [Online]. Available: http://www.microsemi.com/document-portal/doc_view/133269-5071a. [Accessed: 23-Nov-2015].

[39] “Data Sheet: Oven Controlled Crystal Oscillator 501-26636.” (n.d.). Wenzel Associates, Austin, TX.

[40] “Data sheet: Fractional-N PLL with Integrated VCO HMC834LP6GE.” (n.d.). *Hittite Microwave Corporation*. [Online]. Available: http://www.analog.com/media/en/technical-documentation/data-sheets/hmc834.pdf. [Accessed: 16-Dec-2015].

[41] “Data sheet: Digital-to-Analog Converter and Waveform Generator AD9102.” (n.d.), *Analog Devices*, 2013. [Online]. Available: http://www.analog.com/media/en/technical-documentation/data-sheets/AD9102.pdf. [Accessed: 16-Dec-2015].

[42] “Data sheet: Analog-to-Digital Converter AD9102.” (n.d.). *Analog Devices*, 2011. [Online]. Available: http://www.analog.com/media/en/technical-documentation/data-sheets/AD9642.pdf. [Accessed: 16-Dec-2015].

[43] “Data sheet: 400 MHz to 6 GHz Quadrature Demodulator.” (2009). Analog Devices. [Online]. Available: http://www.analog.com/media/en/technical-documentation/data-sheets/ADL5380.pdf. [Accessed: 16-Dec-2015].

[44] W. Kester. (2008, Dec.). “Converting oscillator phase noise to time jitter,” 2008. [Online]. Available: http://www.analog.com/media/en/training-seminars/tutorials/MT-008.pdf.

[45] “Convert SSB phase noise to jitter.” (n.d.). Raltron Electronics Corporation. [Online]. Available: http://www.raltron.com/cust/tools/osc.asp. [Accessed: 16-Dec-2015].

[46] J. R. Vig. (2014, Aug.). “Quartz crystal resonators and oscillators – For frequency control and timing applications – A tutorial.” Rev. 8.5.6.2. [Online]. Available: http://www.ieee-uffc.org/frequency-control/learning-vig-tut.asp.

[47] “Why are Cesium atomic clocks used?” (n.d.). [Online]. Available: http://www.nist.gov/pml/div688/timekeeping.cfm#Cs. [Accessed: 10-Nov-2015].

[48] F. L. Walls and D. A. Hove, “A passive hydrogen maser frequency standard,” in *Proceedings 1978 Frequency and Control Symposium*, 1978, pp. 492–498.

[49] “Data sheet: CCO-083/085.” (n.d.). Crystek Crystals. [Online]. Available: http://www.crystek.com/crystal/spec-sheets/clock/CCO-083_085.pdf. [Accessed: 11-Oct-2015].

[50] “Data Sheet: CO27VS05DE-02-10.000.” (n.d.). Crystek Crystals. [Online]. Available: http://www.crystek.com/crystal/spec-sheets/ocxo/CO27VS05DE-02-10_000.pdf. [Accessed: 11-Oct-2015].

[51] “Data sheet: CVT32 model.” (n.d.). Crystek Crystals. [Online]. Available: http://www.crystek.com/crystal/spec-sheets/tcxo/CVT32.pdf. [Accessed: 10-Nov-2015].

[52] M. Controlled, C. Oscillator, H. Precision, and P. Specifications, “Data sheet: MX-503,” Vectron International. [Online]. Available: http://www.vectron.com/products/ocxo/MX-503.pdf. [Accessed: 23-Nov-2015].

[53] “Data sheet: VS-705.” (n.d.). Vectron International. [Online]. Available: http://www.vectron.com/products/vcso/vs705.pdf. [Accessed: 23-Nov-2015].

[54] “Data Sheet: 8040C Rubidium Frequency Standard.” (n.d.). Symmetricon, Inc. [Online]. Available: http://www.microsemi.com/document-portal/doc_view/133415-8040c. [Accessed: 23-Nov-2015].

[55] “Data Sheet: Quantum SA.45s CSAC.” (2015). Microsemi Corporation. [Online]. Available: http://www.microsemi.com/document-portal/doc_view/133305-quantum-sa-45s-csac. [Accessed: 23-Nov-2015].

THIS PAGE INTENTIONALLY LEFT BLANK

INITIAL DISTRIBUTION LIST

1. Defense Technical Information Center
   Ft. Belvoir, Virginia

2. Dudley Knox Library
   Naval Postgraduate School
   Monterey, California